X-RAY PHOTOELECTRON SPECTROSCOPY FOR CHEMICAL AND ELECTRICAL CHARACTERIZATION OF DEVICES EXTENDED TO LIQUID/SOLID INTERFACES

A DISSERTATION SUBMITED TO
THE GRADUATE SCHOOL OF ENGINEERING AND SCIENCE
OF BILKENT UNIVERSITY
IN PARTIAL FULFILLMENT OF THE REQUIREMENTS FOR
THE DEGREE OF
DOCTOR OF PHILOSOPHY
IN
CHEMISTRY

By
Pınar Aydoğan Göktürk

December 2018

X-RAY PHOTOELECTRON SPECTROSCOPY FOR CHEMICAL AND ELECTRICAL CHARACTERIZATION OF DEVICES EXTENDED TO LIQUID/SOLID INTERFACES

By Pınar Aydoğan Göktürk

December, 2018

We certify that we have read this dissertation and that in our opinion it is fully adequate, in scope and in quality, as a dissertation for the degree of Doctor of Philosophy.

_____

Şefik Süzer (Advisor)

_____

Coşkun Kocabaş

_____

Burak Ülgüt

_____

Ahmet Oral

_____

Mehmet Fatih Danışman

Approved for the Graduate School of Engineering and Science:

_____

Ezhan Karasan

Director of the Graduate School

ABSTRACT

X-RAY PHOTOELECTRON SPECTROSCOPY FOR CHEMICAL AND ELECTRICAL CHARACTERIZATION OF DEVICES EXTENDED TO LIQUID/SOLID INTERFACES

Pınar Aydoğan Göktürk

Ph.D. in Chemistry

Advisor: Şefik Süzer

December 2018

Understanding of electrical and electrochemical devices in operating conditions is vital for development of new technologies. Many important characteristics that determine the performance of such devices lie on their surfaces and interfaces which significantly deviate from the bulk properties. However, particularly for the liquid based devices, carrying out surface analysis is challenging and requires highly sophisticated instrumentation. In this PhD. thesis, we aim to unravel the potential development on liquids, dielectrics as well as the liquid/solid interfaces during AC and DC excitation in a chemically resolved fashion using the UHV compatible non-aqueous liquids in a basic electrowetting on dielectrics configuration within X-Ray Photoelectron Spectroscopy (XPS) chamber. Low molecular weight Polyethylene glycol (PEG) and a particular ionic liquid Diethylmethyl(2-methoxyethyl)ammonium bis(trifluoromethylsulfonyl)imide [DEME][TFSI] are used to represent two extreme cases as being non-ionic and fully-ionic liquids. Application of external electrical bias to these devices either from the

top or the bottom electrode during data acquisition enabled us to investigate the electrowetting phenomenon, in a chemically addressed fashion

In the first part of the thesis, geometrical changes that the drop undergoes during electrowetting have been monitored both by steady state areal maps and by dynamic XPS point analysis where the potential was altered periodically.

In the second part, we have focused only on the DC electrowetting of liquids. We probed the potential developments in the dielectric layer and on the liquid by monitoring the changes in the binding energy of the representative XPS peaks with respect to the applied potential. We showed that the conductivity of the liquid has no influence on the potential and the entire potential drop occurs at the liquid/dielectric interface. Dielectric breakdown and its effect on the potential developments were also investigated in this part.

In the third part, we have tried to understand the frequency dependent potential developments of the ionic liquid and the polyethylene glycol based EWOD devices by AC electrowetting. Our time dependent XPS measurements under AC excitation with sweeping frequency have demonstrated that EWOD devices exhibit two different behaviors separated by a critical frequency, which is dependent on the AC resistance (impedance) or ionic content of the liquid and also the electrical characteristics of the dielectric layer. Below the critical frequency, XPS spectra are mainly affected by the capacitive component of the dielectric, hence the liquid completely screens the applied electrical field. However, for frequencies above the critical, the resistive component of the liquid dominates and the drop behaves like a

resistive strip, resulting in the formation of equipotential surface contours which are shown experimentally for the first time in this study.

In the last part of the thesis, an equivalent circuit model was developed to electrically describe the electrowetting behavior of PEG on dielectric and also to generate a solid-state mimicking device to produce the same XPS spectral observations.

Keywords: X-ray Photoelectron Spectroscopy, ionic liquids, polyethylene-glycol, electrowetting on dielectrics, electrochemical device, in-situ, in-vacuo, operando

ÖZET

AYGITLARIN ELEKTRİKSEL VE KİMYASAL ANALİZLERİ

İÇİN X-IŞINI FOTOELEKTRON SPEKTROSKOPİSİNİN

SIVI/KATI ARAYÜZEYLERİNİ DE KAPSAYACAK ŞEKİLDE GENİŞLETİLMESİ

Pınar Aydoğan Göktürk

Kimya, Doktora Tezi

Danışman: Şefik Süzer

Aralık 2018

Elektriksel ve elektrokimyasal aygıtları çalışma koşullarında incelemek, yeni teknolojilerin geliştirilmesi için hayati önem taşımaktadır. Bu tür aygıtların performansını belirleyen birçok önemli özellikleri, geri kalan kütle ile önemli ölçüde farklılıklar göstermekte olan yüzey ve ara yüzleri tarafından kontrol edilmektedir. Ancak, özellikle sıvı bazlı aygıtlar için, yüzey analizi yapmak zordur ve oldukça gelişmiş enstrümantasyon gerektirmektedir. Bu doktora tez çalışmasında, X-ışını fotoelektron cihazı içinde, geleneksel dielektrik malzemeler üzerindeki elektro-ıslanma konfigürasyonunda çok yüksek vakum uyumlu ve sulu olmayan sıvılar kullanılarak, alternatif ve doğru akım altında sıvı, dielektrik ve sıvı/katı arayüzler üzerindeki potansiyel oluşumların kimyasal çözünürlükle incelenmesi amaçlanmıştır. Düşük moleküler ağırlıktaki polietilen-glikol (PEG) ve özel bir iyonik sıvı (DEME-TFSI) kullanılarak iyonik olmayan ve tamamen iyonik olan sıvılar olmak üzere iki uç noktayı temsil eden sıvılar incelenmiştir. Veri toplanması sırasında üst ya da alt

elektrottan aygıtlara harici bir elektriksel potansiyel uygulanarak, bu potansiyelin kimyasal olarak adreslenmiş bir şekilde ölçülebilmesi, elektro-ıslanma olayını hem kimyasal hem de elektriksel boyutlardan incelenebilmesini sağlamıştır.

Tezin ilk bölümünde, elektro ıslanma sırasında damlacıkta meydana gelen geometrik değişiklikler, hem durağan alansal taramalar, hem de potansiyelin periyodik olarak değiştirildiği dinamik XPS nokta analizleri ile izlenmiştir.

İkinci bölümde, sıvıların sadece DC altındaki elektro-ıslanmalarına odaklanılmıştır. Hem sıvıyı hem de dielektrik alt taşını temsil eden XPS tepelerinin bağlanma enerjisindeki değişimler, dışarıdan uygulanan elektriksel potansiyele göre izlenerek, hem dielektrik tabakadaki, hem de sıvının değişik bölgelerindeki potansiyel gelişmeleri tespit edilmiştir. Sıvının iletkenliğinin, sıvı/dielektrik ara yüzeyinde meydana gelen potansiyel dağılımı üzerinde hiçbir etkisinin olmadığı gösterilmiştir. Ayrıca, dielektrik bozulma ve bunun sıvı üzerindeki potansiyel gelişimi üzerine etkisi de bu bölümde incelenmiştir.

Üçüncü bölümde, iyonik sıvı ve polietilen glikol bazlı aygıtların frekansa bağlı AC elektro-ıslanma sırasındaki potansiyel gelişmeleri incelenmiştir. AC uyarımı altında frekans taraması ile yapılan zamana bağlı XPS ölçümleri; aygıtların, sıvının direncine veya iyonik içeriğine ve ayrıca dielektrik tabakanın elektriksel özelliklerine bağlı olan kritik bir frekansla ayrılan, iki farklı davranış sergilediğini göstermiştir. Kritik frekanstan düşük değerlerde, XPS spektrumları esas olarak dielektriğin kapasitif bileşeni tarafından belirlenmekte olup, dolayısıyla sıvı uygulanan elektrik alanını tamamen bloke etmektedir. Bununla birlikte, kritiğin üzerindeki frekanslar

için, sıvının direnci baskındır ve damla, bir direnç şeridi gibi davranmaktadır. Bu davranışın sonucunda oluşan eş potansiyel yüzey konturları da ilk kez deneysel olarak bu çalışmada gösterilmiştir.

Tezin son bölümünde, araştırılan sistemi elektriksel olarak tanımlamak ve aynı XPS spektral gözlemini tekrarlayabilmek için kullanılacak olan ve katı hal direnç ve kapasitörlerden oluşan bir taklit cihaz üretmek için eşdeğer bir devre modeli geliştirilmiştir.

Anahtar Kelimeler: X-ışını Fotoelektron Spektroskopisi, iyonik sıvılar, polietilen glikol, dielektrik üzerinde elektro-ıslanma, elektrokimyasal cihaz, gerçek zamanlı, çalışma durumunda

Acknowledgements

At the official end of my education life, I feel that it is only the beginning for my scientific adventure. This thesis and many of other achievements would not be possible without the guidance of my advisor, Prof. Şefik Süzer. He helped me to shape the figure of scientist in my head. I want to express my sincere gratitude to him for being an excellent mentor. He always encouraged me to achieve more. I learnt a lot from him. During my years in his research group, everybody asked me the reason why I chosen him in the first place, now I believe from where I stand, I am the answer for those questions.

Additionally, I would like to thank to Dr. Coskun Kocabas and Dr. Burak Ülgüt for their valuable discussions and contributions to my research. I also want to thank to the first person, Dr. Gülay Ertaş, who gave me opportunity to begin doing research in my sophomore years.

Our former group members Merve Camcı and Ahmet Uçar were always on my side and always encouraged me even if they were thousand miles away. Besides being lab-mates, they are more than friends to me. Special thanks to my friend Seylan Ayan from the chemistry department for motivating me during our studies and qualifying exam. I also want to thank Ceren Çamur for being my best friend from the day we met in the first year of our university. I want to thank her for the sleepless nights we were studying together. On the other hand, I appreciate our department secretary Emine Yiğit for her support, patience and assistance. These people made Bilkent a second home for me.

I would like to acknowledge the Scientific and Technological Research Council of Turkey (TUBITAK) for the financial support through Project Numbers 212M051 and 215Z53.

I must express my profound gratitude to my parents and to my sister for providing me a continuous support and encouragement throughout my years of study. I am proud to be their daughter.

Last but not the least, I am so lucky to have such a loving husband who always believes in me. He makes everything possible to simplify my life. I would not have gone this far without him.

To my husband Ekin

Contents

Chapter 1

1. Introduction 1

1.1. X-ray Photoelectron Spectroscopy 1

1.1.1. Basic Principles of X-ray Photoelectron Spectroscopy 1

1.1.2. Common usage of XPS 5

1.1.3. Application of Electrical Bias 8

1.1.3.1. *Operando* XPS 12

1.1.4. Analyzing Liquid Surfaces with Photoelectron Spectroscopy 14

1.1.4.1. Ionic Liquids 16

1.1.4.1.1. General Properties and Applications of Ionic Liquids 16

1.1.4.1.2. Ionic Liquids and XPS 18

1.1.4.1.3. *In-situ* reaction Monitoring of Ionic Liquids 20

1.1.4.2. Low Volatility Organic Solvents 22

1.2. Electrowetting **24**

1.2.1. Fundamentals of Electrowetting 24

1.2.1.1. Challenges in EWOD 27

1.2.1.2. D.C. Electrowetting 30

1.2.1.3. A C. Electrowetting 30

1.2.2. Applications of Electrowetting Phenomenon 33

1.2.3. Electrowetting of Nonaqueous Liquids 35

1.2.4. Dynamics of Electrowetting 36

1.3. Aim of the Study **37**

Chapter 2

2. Experimental **39**

2.1. Materials **39**

2.2. EWOD Device Preparation **40**

2.3. Instrumentation **41**

2.3.1. Characterization Techniques 41

2.3.1.1. X-Ray Photoelectron Spectroscopy 41

2.3.1.2. Contact Angle Meter 42

2.3.1.3. Electrical Impedance Spectroscopy and Modeling 43

2.4. XPS Analysis of Electrical Circuit Mimicking EWOD Devices **44**

Chapter 3

3. Results and Discussions 45

3.1. Characterization of the Hydrophobic Layer 45

3.2. Conventional XPS Analysis on EWOD Devices 47

3.3. Electrowetting of PEG 51

3.3.1. Geometrical Changes in air ambient 51

3.3.2. Geometrical Changes in vacuo 53

3.4. Potential Developments Under DC Excitation 58

3.4.1. Dielectric Breakdown 65

3.5. Potential Developments Under AC Excitation 71

3.6. **Model Electrical Circuits Mimicking The EWOD Devices** 86

Chapter 4

4. Conclusions 95

Bibliography 98

List of Figures

Figure 1 Simple schematic representation of X-Ray Photoelectron Spectroscopy 3

Figure 2 Energy level diagram of an unbiased conductive sample and spectrometer system. 4

Figure 3 XP survey of graphene on silicon wafer representing the photoelectron peaks from core level and Auger peaks together with high resolution Si2p, O1s and C1s regions. 6

Figure 4 Energy level diagram of biased and unbiased conductive sample with spectrometer system. 9

Figure 5 XP spectra of a conducting gold metal when sample is grounded, subjected to +4V and -4V D.C. voltage bias and SQW excitation of 4V amplitude with 1 kHz frequency 10

Figure 6 XP spectra of PEG when the wire electrode is grounded, subjected to squarewave and sine wave excitation of 6V amplitude with 50 Hz frequency. 11

Figure 7 Voltage-Contrast XPS Areal maps for the measured binding energies of C1s peak (a) as the device is under the external bias before (b) same device after the mild plasma oxidation and (c) after creating of a line defect with Ar^+ ion beam. Reprinted with permission from Aydogan, P., Polat, E. O., Kocabas, C. & Suzer, S. X-Ray Photoelectron Spectroscopy for Identification of Morphological Defects and Disorders in Graphene Devices. 34, 041516, (2016). Copyright 2018, American Vacuum Society 13

Figure 8 XP N1s spectra of [BMIM][PF_6] during the electrochemical process. The spectra are recorded in the line scan mode, at different time intervals and across the two gold electrodes. Adopted from Ref [82] with permission from the Centre National de la Recherche Scientifique (CNRS) and The Royal Society of Chemistry. 22

Figure 9 Schematic representation of an electrowetting on dielectric device with a hydrophobic layer between the dielectric and the liquid 26

Figure 10 Picture of the contact line instability of polyethylene glycol drop under high voltages representing the mother and satellite droplets 29

Figure 11 Schematic representation of the equivalent circuit diagram for a droplet on a dielectric-covered electrode. 31

Figure 12 Schematic representation for a droplet on hydrophobized dielectric-covered electrode. (Adapted with permission from Aydogan Gokturk, P., Ulgut, B. and Suzer, S. “DC Electrowetting of Nonaqueous Liquid Revisited by XPS”. Langmuir 2018, 34, 7301-7308. Copyright 2018, American Chemical Society.)..... 40

Figure 13 Schematic representation of the equivalent circuit diagram for a droplet on a dielectric-covered electrode (Adapted with permission from Aydogan Gokturk, P., Ulgut, B. and Suzer, S. “DC Electrowetting of Nonaqueous Liquid Revisited by

XPS". Langmuir 2018, 34, 7301-7308. Copyright 2018, American Chemical Society.) 42

Figure 14 Schematic representation of the contact angle measurements of EWOD devices during the external electrical stimuli 43

Figure 15 Thickness profile of the CYTOP layer. (Reprinted with permission from Aydogan Gokturk, P., Ulgut, B. and Suzer, S. "DC Electrowetting of Nonaqueous Liquid Revisited by XPS". Langmuir 2018, 34, 7301-7308. Copyright 2018, American Chemical Society.) 46

Figure 16 Side-view images of water droplet before and after the CYTOP coating.. 46

Figure 17 XP survey spectrum coming from the PEG surface with elemental regions in the high-resolution scanning mode. 47

Figure 18 XP survey spectrum coming from the IL surface. The insets show various elemental regions in the high-resolution scanning mode 49

Figure 19 XP survey spectrum coming from the CYTOP surface. The insets show various elemental regions in the high-resolution scanning mode. (Adapted with permission from Aydogan Gokturk, P., Ulgut, B. and Suzer, S. "DC Electrowetting of Nonaqueous Liquid Revisited by XPS". Langmuir 2018, 34, 7301-7308. Copyright 2018, American Chemical Society.)..... 50

Figure 20 DC Voltage dependence of contact angle. The voltage was increased from 0 to 50 V, and then brought back to 0 V and decreased from 0 to -50V gradually... 52

Figure 21 DC Voltage dependence of contact angle and shape of PEG droplet. The voltage increased from 0 to 50 V, and then back to 0 V and decreased from 0 to -

50V gradually. (Reprinted with permission from Aydogan Gokturk, P., Ulgut, B. and Suzer, S. “DC Electrowetting of Nonaqueous Liquid Revisited by XPS”. Langmuir 2018, 34, 7301-7308. Copyright 2018, American Chemical Society.)..... 53

Figure 22 DC Voltage dependence of contact angle and shape of PEG droplet. The voltage increased from 0 to 50 V, and then back to 0 V and decreased from 0 to -50V gradually. (Reprinted with permission from Aydogan Gokturk, P., Ulgut, B. and Suzer, S. “DC Electrowetting of Nonaqueous Liquid Revisited by XPS”. Langmuir 2018, 34, 7301-7308. Copyright 2018, American Chemical Society.)..... 56

Figure 23 DC Voltage dependence of contact angle and shape of PEG droplet. The voltage increased from 0 to 50 V, and then back to 0 V and decreased from 0 to -50V gradually. (Reprinted with permission from Aydogan Gokturk, P., Ulgut, B. and Suzer, S. “DC Electrowetting of Nonaqueous Liquid Revisited by XPS”. Langmuir 2018, 34, 7301-7308. Copyright 2018, American Chemical Society.)..... 57

Figure 24 C1s spectra recorded at different applied bias, along the line shown in the inset. The lateral position of the liquid/substrate interface, determined by the region where both C1s features overlap, also moves with the bias. (Reprinted with permission from Aydogan Gokturk, P., Ulgut, B. and Suzer, S. “DC Electrowetting of Nonaqueous Liquid Revisited by XPS”. Langmuir 2018, 34, 7301-7308. Copyright 2018, American Chemical Society.)..... 59

Figure 25 F1s spectra recorded at ground and +40V applied bias, along the line beginning from the substrate towards to the middle of the drop. 61

Figure 26 O1s and F1s spectra recorded at different applied bias, along the line beginning from the substrate towards to the middle of the drop. 62

Figure 27 Line-scan spectra of; **(a)** F1s and **(b)** C1s regions, recorded under +100 V bias and with 30 μm spot and 20 μm step sizes, along a line into the drop. **(c)** Variations in the width of the C1s peak. **(d)** Atomic percentages computed. Representative spectra at the designated point; **(e) C1s** and **(d)** F1s. **(**Reprinted with permission from Aydogan Gokturk, P., Ulgut, B. and Suzer, S. "DC Electrowetting of Nonaqueous Liquid Revisited by XPS". Langmuir 2018, 34, 7301-7308. Copyright 2018, American Chemical Society.)..... 63

Figure 28 Time-resolved C1s spectra in a fast snap-shot mode (> 12 spectra/s) recorded under 10 SQW excitation 65

Figure 29 C1s region on the drop, recorded at different bias applied to the liquid until potential where the dielectric breakdown occurs. **(**Reprinted with permission from Aydogan Gokturk, P., Ulgut, B. and Suzer, S. "DC Electrowetting of Nonaqueous Liquid Revisited by XPS". Langmuir 2018, 34, 7301-7308. Copyright 2018, American Chemical Society.)..... 66

Figure 30 C1s spectra recorded at +20V increments until the onset of the breakdown at +120V, and afterwards at ∼1 minute intervals, but still under +120V. Note that the drop recovers and returns to the full applied bias within minutes. (Reprinted with permission from Aydogan Gokturk, P., Ulgut, B. and Suzer, S. "DC Electrowetting of Nonaqueous Liquid Revisited by XPS". Langmuir 2018, 34, 7301-7308. Copyright 2018, American Chemical Society.)..... 67

Figure 31 Current measurements through a liquid (PEG) drop during an XPS investigation, under various biases approaching the breakdown and beyond. (Reprinted with permission from Aydogan Gokturk, P., Ulgut, B. and Suzer, S. "DC Electrowetting of Nonaqueous Liquid Revisited by XPS". Langmuir 2018, 34, 7301-7308. Copyright 2018, American Chemical Society.)..... 68

Figure 32 Snapshot images from the video recording of top-gated PEG EWOD device in air ambient with the application of different amplitude of potentials before and after the dielectric breakdown. (Reprinted with permission from Aydogan Gokturk, P., Ulgut, B. and Suzer, S. "DC Electrowetting of Nonaqueous Liquid Revisited by XPS". Langmuir 2018, 34, 7301-7308. Copyright 2018, American Chemical Society.) 70

Figure 33 F1s spectra recorded at different AC SQW frequencies, along the line beginning from the substrate towards to the middle of the drop. 73

Figure 34 O1s spectra recorded at different AC SQW frequencies, along the line beginning from the substrate towards to the middle of the drop 74

Figure 35 Schematic representation of the AC actuation by imposing the bias from; (a)(c) the bottom or (b)(d) the top electrodes, together with the recorded O1s and F1s spectra for PEG and IL devices respectively while sweeping the frequency**.**..... 76

Figure 36 Time dependent iterative spectra of O1s region as a 2D intensity and frequency plot with respect to the iteration number. 77

Figure 37 Time dependent iterative spectra of O1s region as a 2D intensity and frequency plot with respect to the iteration number. 78

Figure 38 O1s spectra recorded under continuous AC actuation at three different positions on the drop, while imposing the bias from; (a) the top or (b) the bottom electrodes..... 80

Figure 39 Areal maps of the binding energy difference of positive and negative components of O1s under the applied 6V square wave bias from the bottom

electrode with; (a) 50 Hz, and; (b) 1 kHz frequencies together with their schematic representations. 82

Figure 40 Areal maps of the binding energy difference of positive and negative components of O1s under the applied 6V square wave bias from the bottom electrode with 1 kHz frequencies together with illustrative O1s spectra coming from two different positions. 83

Figure 41 O1s spectra recorded under continuous AC actuation (10^{-1} to 10^{4} Hz) for three different liquid drops. 85

Figure 42 Impedance modulus versus frequency for the PEG electrowetting at 0.5 V AC voltage 89

Figure 43 Output waveforms generated from the b position on the proposed circuit at three different frequencies and corresponding simulated O1s spectra from each of them 90

Figure 44 (a) and (b). Simulated O1s spectra at two different positions on the equivalent circuit used, while (c) and (d) are the recorded ones, on the liquid surface at two different points. 91

Figure 45 Sn3d spectra recorded at four different positions on the mimicking device. Top row correspond to actuation from the wire electrode, while bottom row from the planar Si electrode. 93

List of Schemes

Scheme 1 a) Equivalent circuit model for the EWOD system under investigation and b) Simplified equivalent circuit model 87

Scheme 2 Schematic representation of solid-state mimicking device developed from the EIS and computational resuls 89

List of Abbreviations

AC: Alternating Current

APXPS: Ambient Pressure X-Ray Photoelectron Spectroscopy

ARXPS: Angle Resolved X-Ray Photoelectron Spectroscopy

CA: Contact Angle

DC: Direct Cureent

DEME-TFSI: Diethylmethyl(2-methoxyethyl)ammonium

bis(trifluoromethanesulfonyl) imide

EDL: Electrical Double Layer

ESCA: Electron Spectroscopy for Chemical Analysis

EW: Electrowetting

EWOD: Electrowetting on Dielectrics

IL: Ionic Liquid

IMFP: Inelastic mean free path

NP: Nanoparticle

PEG: Polyethylene glycol

PEO: Polyethylene Oxide

RTIL: Room Temperature Ionic Liquid

SQW: Square Wave

UHV: Ultra High Vacuum

XPS: X-Ray Photoelectron Spectroscopy

XP: X-Ray Photoelectron

Chapter 1

1. Introduction

1.1. X-Ray Photoelectron Spectroscopy

1.1.1. Basic Principles of X-Ray Photoelectron Spectroscopy

The origin of X-ray Photoelectron Spectroscopy (XPS) reaches back to the well-known photoelectric effect. First XPS also known as ESCA (electron spectroscopy for chemical analysis) was developed by Kai Siegbahn during the 1950s at the University of Uppsala, Sweden.[1,2] Siegbahn was later awarded the Nobel Prize in Physics for his preliminary works on the development of ESCA.[3] In XPS, X-rays with known energies (usually Al-Kα or Mg-Kα with photon energy 1486.6 and 1253.6 eV respectively) are used as an exciting photon source, which interact with the specimen and lead to the excitation and emission of photoelectrons.[4] In

order for these emitted electrons to travel from sample towards the analyzer of the spectrometer, amount of gas molecules exist in the chamber should be minimized. Otherwise, they will be scattered and lost due to several unavoidable collisions. That is why, XPS requires ultra-high vacuum (UHV) conditions, which decreases the density of gas molecules and lengthens the mean free path of electrons.[5]

For determining the kinetic energy of the ejected photoelectrons, hemispherical analyzer is used. The analyzing system consists of an electrostatic input lens, a hemispherical deflector with entrance and exit slits to the analyzer and the electron detector, respectively. When photoelectrons reach the spectrometer's analyzer, they are dispersed according to their kinetic energies. As a final step, the electrons hit the electron detector, which is either channeltron or a multi-channel detector at which their energy and the number density for each particular energy are measured. Then, photoemission intensity versus the photoelectron kinetic or binding energy are displayed.[6] Figure 1 shows the simple schematic representation of X-Ray Photoelectron Spectroscopy with primary components as the radiation source, sample, electron energy analyzer and the electron detector.

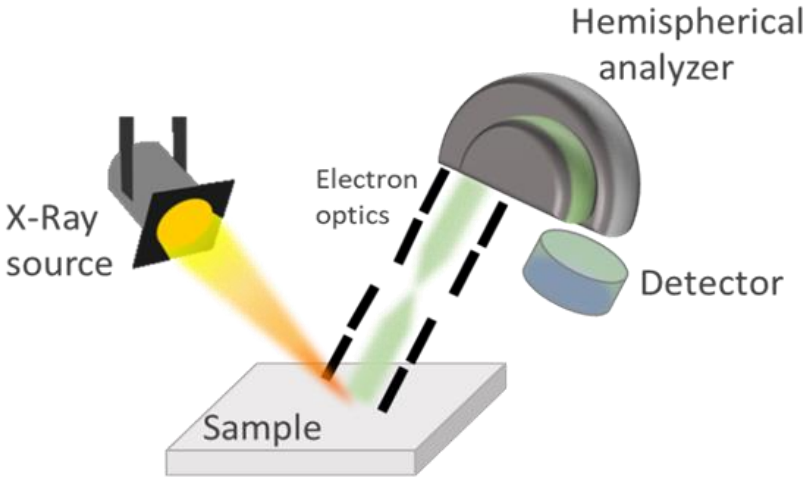

Figure 1 Simple schematic representation of X-Ray Photoelectron Spectroscopy set-up

Kinetic energy of emitted photoelectrons follows the basic equation; [7]

$$\mathrm{E_{kin}} = h\vartheta - \mathrm{E_{binding}} - \Phi_{sample}$$

where $\mathrm{E_{kin}}$ is the kinetic energy and $\mathrm{E_{binding}}$ the binding energy of the emitted electron, $h\vartheta$ is the energy of X-rays coming from the source and Φ is the work function of analyzed sample. For a conductive solid sample, Fermi levels of the sample and the spectrometer are aligned. Hence, knowledge of only the spectrometer's work function is enough to compute the binding energy of the core level electrons. Therefore, for solid samples binding energy is conventionally measured with respect to the Fermi level. A related energy level diagram for conductive samples is illustrated in Figure 2.

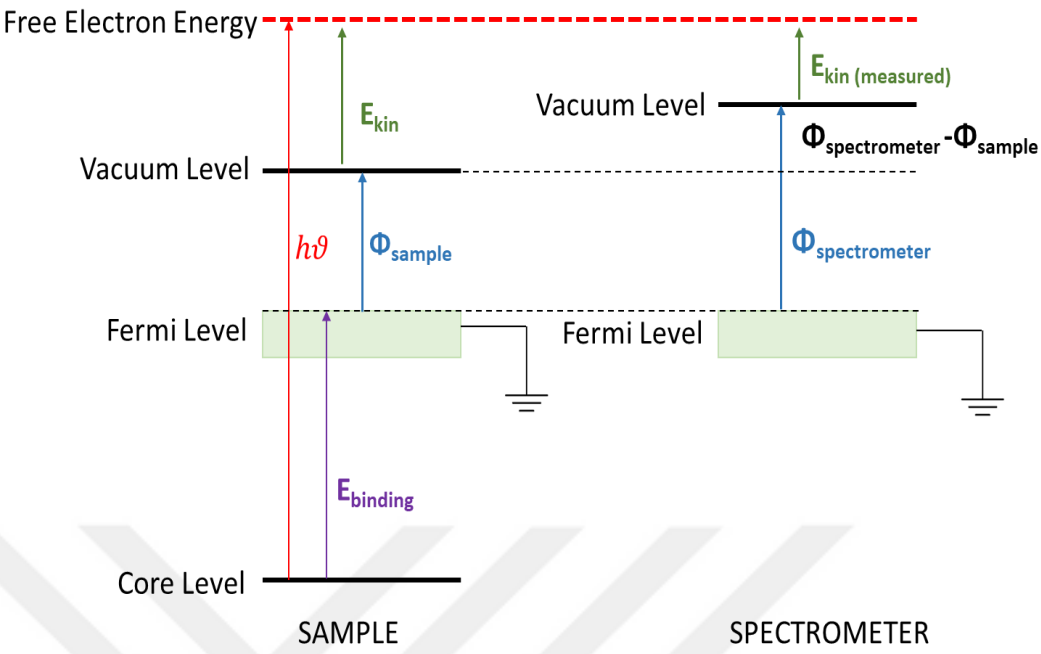

$$E_{binding} = h\vartheta - E_{kin} - \Phi_{sample}$$
$$= h\vartheta - E_{kin}(measured) - \Phi_{spectrometer}$$

Figure 2 Energy level diagram of an unbiased conductive sample and spectrometer system.

However, for an insulating sample, build-up of positive charge due to ejected electrons decreases all energy levels of the sample relative to the spectrometer's. Thus, this additional potential developed from charging results in an increase in the apparent binding energies. This unwanted surface charging can be minimized by using low energy electron flood gun during data acquisition or can be corrected by calibrating the energy scale through shifting the whole spectrum to set a specific peak to its known binding energy value, such as C1s to 285.0 eV.

As mentioned previously, electrons undergo collisions within the solid even before they escape the surface. Inelastic mean free path (IMFP) (λ_i) of the emitted

photoelectrons is defined as the length from which 36.79% of all photoelectrons are scattered through collision by the time they reach the surface. Therefore, the sampling depth in XPS is generally accepted to be equal to the $\sim 3\lambda_i$.[8] Accordingly, the probing depth of XPS is around 1-10 nm, which makes XPS a surface sensitive technique. Since the probing depth is strongly related with the kinetic energy, tunable X-ray sources enable to control the surface sensitivity, as in the case for synchrotron based analyses.[9]

1.1.2. Common usage of XPS

Binding energies of emitted photoelectrons are specific to each element and to their chemical environments. While the main photoelectron peaks arise from the electrons emitted without any energy loss, other electrons from deeper below the surface, which undergo scattering and loose energy, reaches the analyzer with decreased kinetic energy and contribute to the background of the spectrum. That is why, XPS spectra show characteristic increase in the background towards higher binding energy side of each peak.[10] Conventionally, two kinds of spectra, survey and high resolution regions are recorded. The survey spectrum with lower energy resolution covers a wide scale of binding energies, typically between 1-1400 eV and shows characteristic peaks for each element found on the surface of the sample under investigation. Figure 3 shows the survey spectrum of a graphene layer on a silicon substrate using 200 eV pass energy together with the high resolution regions acquired with 50 eV pass energy. In the survey spectrum, there are two main

regions consisting of peaks coming: i) from emission from core levels and (ii) from X-ray excited Auger emission in higher binding energies (beyond 1100 eV). Auger emission occurs when one electron from higher energy level falls down to core level hole, which is created by the emission of the photoelectron and excess energy of this process simultaneously, results in emitting the second (Auger) electron. Unlike the XPS lines, kinetic energy of Auger peaks does not change with the X-ray source. However, Auger peak positions in binding energy scale depend on the energy of exciting X-Ray source.

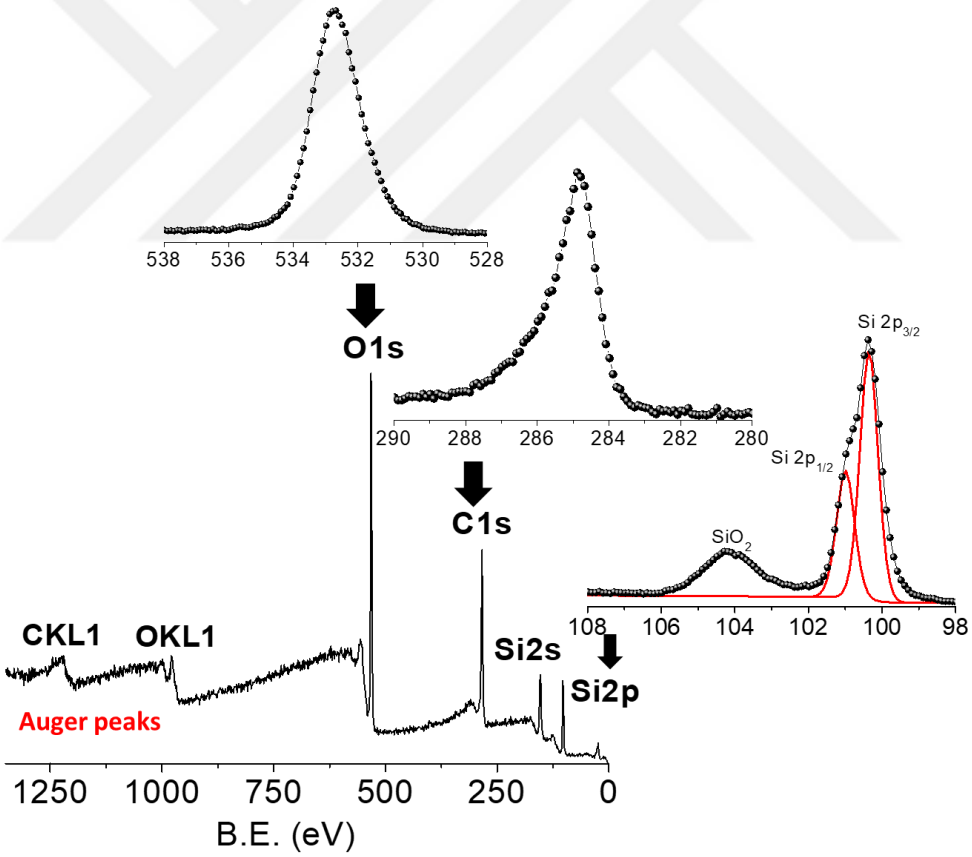

Figure 3 XP survey of graphene on silicon wafer representing the photoelectron peaks from core level and Auger peaks together with high resolution Si2p, O1s and C1s regions.

Many elements have multiple photoelectron lines corresponding to the discrete electron orbitals from which the photoelectrons are emitted. For example for silicon sample peaks both the Si 2p and Si 2s core levels are seen in the survey spectrum at the same time[9], as illustrated in Figure 4. Note that, S1s level has a binding energy of 1839, which is beyond the reach of AlKα X-Rays of 1486.6 eV. Additionally, all photoelectron peaks, except those from s orbitals, appear as spin-orbit doublets[11], see Figure 3.

Types of bonding (covalent or ionic) in compounds may also cause additional shifts in the binding energy positions, which are called chemical shifts.[12] Generally, withdrawal of valance electrons cause increase, while the addition of electrons cause decrease in the binding energy. This ability to identify the oxidation states and chemical environments of elements is one of the strong sides of this XPS technique.

In addition to the elemental identification and deducing bonding properties, XPS can also be used for quantification purposes. As in many spectroscopic techniques, the area under the XPS peak is directly related to the atomic concentration on the surface. If one considers the transmission function of the analyzer, the sensitivity factors for elements and the emission angle, the chemical stoichiometry can be found with a high accuracy. (in $\sim$1% at.)

Other common areas that XPS is used involves; i) depth profiling as either destructively by using the ion gun etching or non-destructively by changing the emission angle to change the surface sensitivity [13] and ii) chemical imaging by

mapping the surface. XPS elemental and chemical state imaging is generally performed by a rastering method where X-ray beam is scanned across the sample. This process provides pixel by pixel information and reveals a 2D image. It is also useful for analyzing the lateral variations in the surface chemical structure but the lateral resolution in XPS is generally at the tens of microns scale. This method is slow that is why generally a selected small binding energy range for a specific element and fast acquisition mode (snapshot mode) is used for this type of measurements. Accordingly, either the binding energy positions or the peak intensity variations for a specific peak can be analyzed from a selected area.[14,15]

Time-resolved X-ray photoelectron spectroscopy, on the other hand, is a powerful tool to observe the real time changes on the surface of the sample under investigation. For time resolved XPS, spectra are recorded continuously as a function of time while exposing the surface to some kind of external stimuli such as; temperature change, electrical and/or optical pulses etc.

1.1.3. Application of External Bias

The binding energy of the photoelectrons can also be varied intentionally by applying an external bias that effectively shifts all energy levels up or down depending on the sign of the potential applied, with respect to those of the grounded spectrometer and creates a surface potential. The result is that, under the positive excitation, apparent binding energy shifts to the higher values and vice

versa.[16] Figure 4 shows the energy level diagram of a positive-biased, unbiased conductive sample and the spectrometer for comparison.

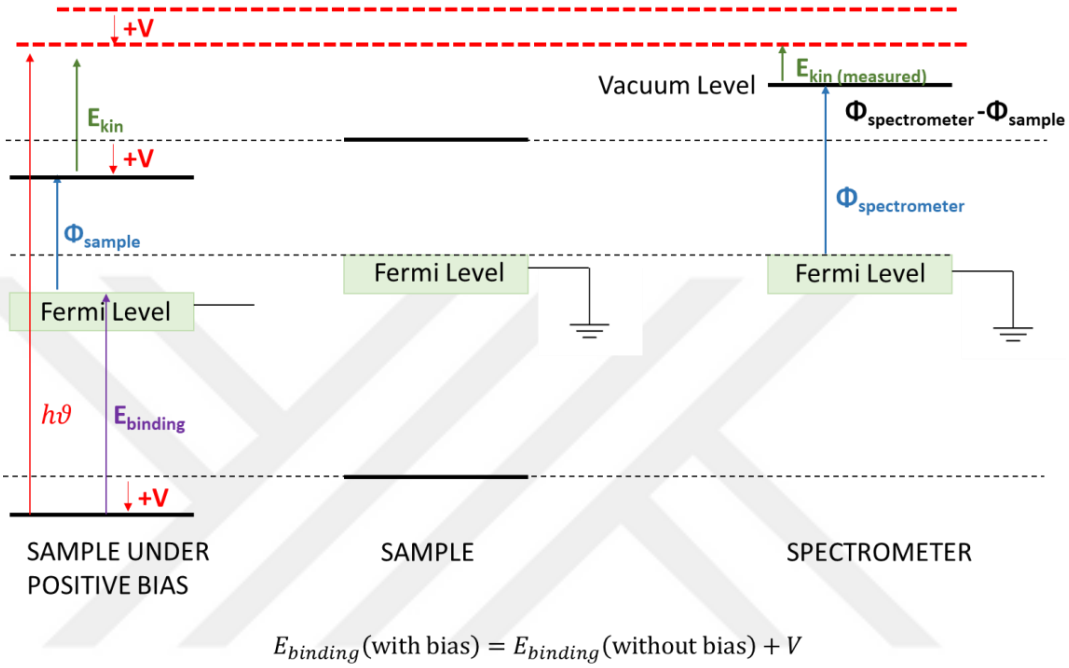

Figure 4 Energy level diagram of biased and unbiased conductive sample with spectrometer system.

This shift in binding energy is directly related to the magnitude of surface potential.[17] For example, when an external bias is applied to a conducting sample such as gold, see in Figure 5, the measured binding energy of photoelectron peaks shift in eV with the same amplitude of the applied bias (i.e. 4V causes 4.0 eV shift).[18] However, shifts with smaller amplitude than the applied bias are usually observed for poorly-conductive or non-conductive surfaces, due to additional charging caused by the emitting photoelectrons.[19,20] Like the DC excitation, AC excitation is also possible during XP data acquisition[21]. Under a dynamic

excitation, alternating between positive and negative bias with a given frequency is given to the sample.[18,22] [23] Depending on the time scale of a single scan, the XP line shape may or may not be changed. For example, for a conducting sample with low frequency AC measurements (in mHz range) a collection of time-resolved XP spectra gives the waveform of excitation. However, under the AC excitation with a frequency higher than the time scale of a single scan, both the minimum and the maximum of the applied voltages are reflected as the voltage response at the same time. For square wave (SQW) application this is directly seen as two twinned peaks, see Figure 5.

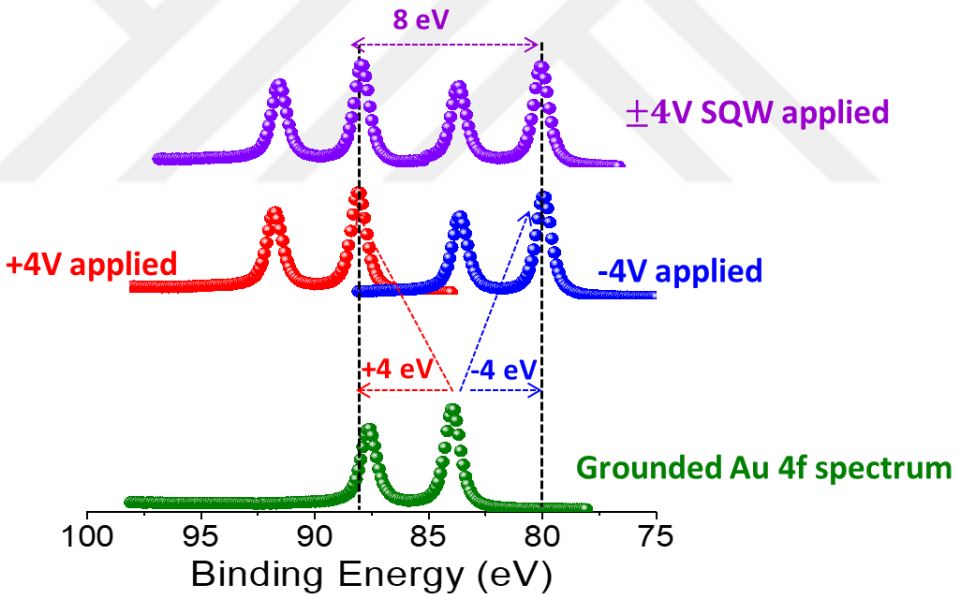

Figure 5 XP spectra of a conducting gold metal when sample is grounded, subjected to +4V and -4V D.C. voltage bias and SQW excitation of 4V amplitude with 1 kHz frequency

We note that for many electrical and electrochemical characterizations, sinusoidal waveform is used, because its use is convenient and well-established.

However, sine wave excitation to the XPS sample during data acquisition is difficult to handle since it introduces severe distortion to the line shape of the XPS peaks. Typical XPS spectra of C1s coming from a PEG drop under the 50 Hz sine and square wave excitations are shown in Figure 6 together with its grounded form. Although application of square wave causes only a twin peak at the minimum and the maximum of the applied voltages, sine wave application introduces two fairly intense peaks near the minimum and maximum of the applied voltages as well as several in between. It also causes large amount of decrease in intensity. Triangular wave excitation is also similar with the sine wave that is why, we are mainly using the SQW excitation for AC analysis.

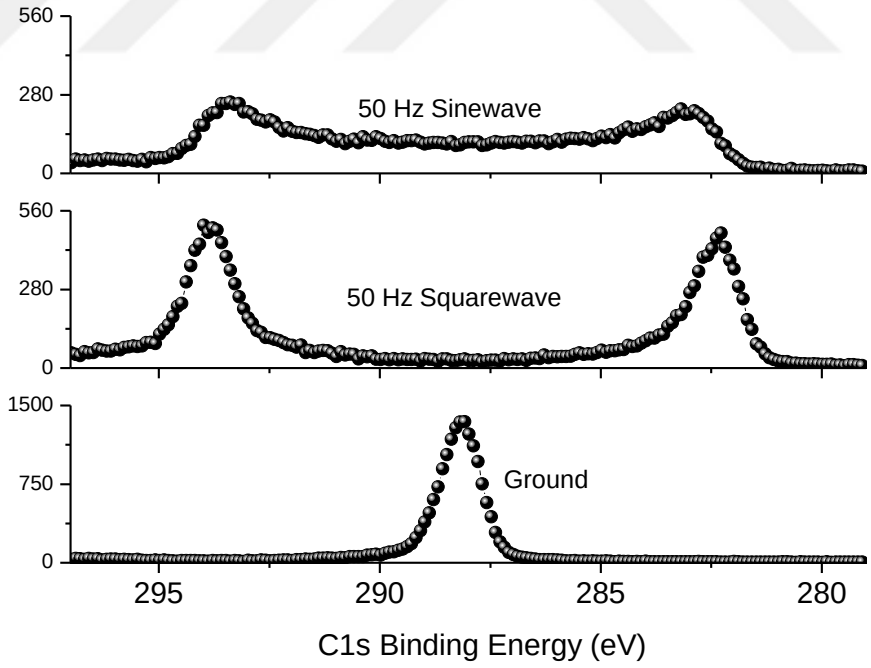

Figure 6 XP spectra of PEG when the wire electrode is grounded, subjected to squarewave and sine wave excitation of 6V amplitude with 50 Hz frequency.

1.1.3.1. *Operando* XPS

Traditionally, surface science investigations have been performed in two ways, either as an ex situ one by comparing the surface characteristics before and after a specific process aimed to investigate or as in operando by interrogating the surface of the sample during the process. *Operando* XPS can be useful for many applications especially in investigation of electrical and electrochemical devices. For instance, in one of our previous papers, we reported a Voltage-Contrast XPS study of a solid-state device, where a graphene layer was fabricated between two gold electrodes in a coplanar geometry, in order to quantify the macroscopic defects on the graphene layer. It is known that the structural defects in graphene affect the local electronic and mechanical properties. For this reason, an external +6V bias was applied between the two electrodes and areal mapping of elements were performed for the measurements. By tracing the changes in the binding energy, we extracted the voltage variations in the graphene layer which reveal information about the structural defects, cracks, impurities, and oxidation levels in graphene layer.[24] We also showed that with the increase in the quantity of defects, the sheet resistance and the deviations of binding energy values from the linear shape of potential drop increases, see Figure 7.

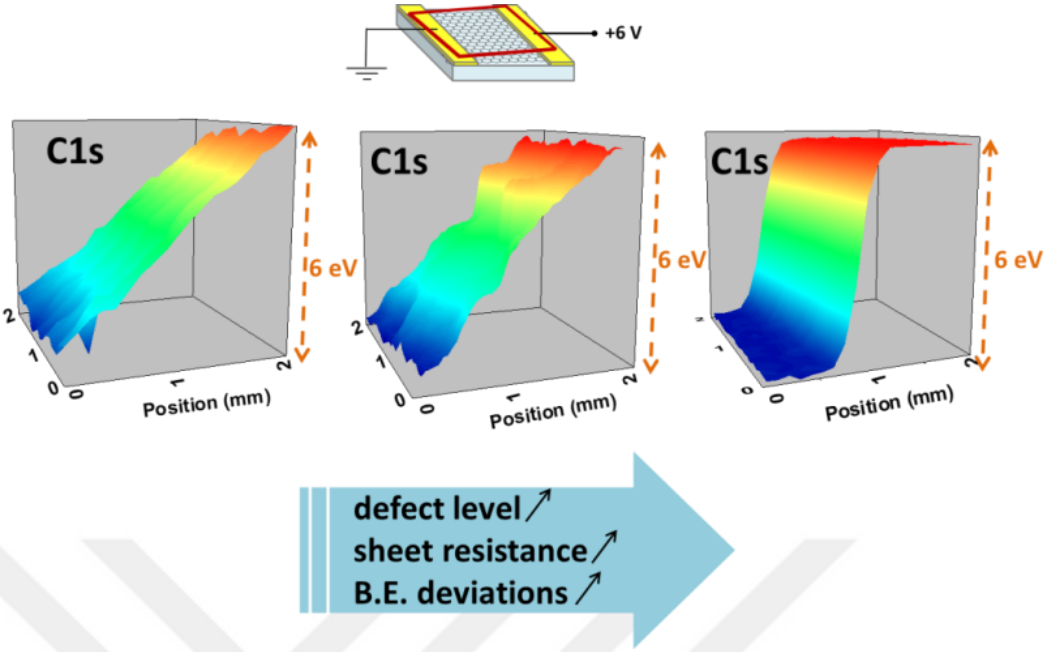

Figure 7 Voltage-Contrast XPS Areal maps for the measured binding energies of C1s peak (a) as the device is under the external bias before (b) same device after the mild plasma oxidation and (c) after creating of a line defect with Ar^+ ion beam. *Reprinted with permission from Aydogan, P., Polat, E. O., Kocabas, C. & Suzer, S. X-Ray Photoelectron Spectroscopy for Identification of Morphological Defects and Disorders in Graphene Devices. 34, 041516, (2016). Copyright 2018, American Vacuum Society*

We also reported on the X-Ray photoemission from the graphene and dielectric layer on back-gated transistor geometry under operating conditions where we applied different amplitudes of external potentials from the gate while we grounded the both source and the drain electrodes. We observed that application of gate voltages dopes the graphene and changes its Fermi level that can be followed through the change of measured C1s binding energy.[25]

After that, we went one step further and investigated the electrical behavior of a single graphene transistor in a 64-element integrated circuit by applying a

constant voltage bias of +3V DC to the source electrode and a variable voltage bias to the gate electrode, while grounding the drain electrode. By tracing the shifts in the binding energy of C1s, electrical potential variations were shown, and sheet resistance of the graphene layer, as well as the contact resistances between the metal electrodes were computed.[26]

In another study, we investigated the double layer capacitor made of an ionic liquid electrolyte filled between two gold electrodes and probed the potential development on the surface of ionic liquid during charging process.[27] Additionally, application of squarewave potentials with varying frequency enabled us the real time observation of fast processes (like charge screening due to ion rearrangements) occurring in a time scale of milliseconds to a few minutes by XPS studies under laboratory conditions.

1.1.4. Analyzing Liquid Surfaces with Photoelectron Spectroscopy

Implementation of UHV analytical techniques to the liquids has been a dream for many surface scientists starting by Kai Siegbahn himself and more importantly by his son Hans Siegbahn because many aqueous or organic liquids are not compatible with these tools due to their high vapor pressure. However, understanding liquids and especially the liquid/solid or liquid/vapor interfaces are crucial for several scientific fields including electrochemistry, corrosion, heterogeneous catalysis and environmental chemistry since they play an important role in many natural processes too.[16,28-31]

Kai and Hans Siegbahn laid the foundations for applying ESCA to liquids. In 1973, they presented the first spectrum of a liquid, which is the formamide, in their paper 'ESCA applied to liquids'. In the same study, they also showed the ways to separate the signals of the liquid from the vapor.[32] With the improvement of the technique, in 1985 Hans Siegbahn has able to report the photoelectron spectra of various glycol salt solutions as well as pure liquids.[33] He also provided important future prospects and potential applications for liquids ESCA, which gave inspiration to the next generation of researchers.

With the ambient pressure X-ray Photoelectron Spectroscopy (APXPS), which allows measurement in the Torr range, analysis of aqueous solutions in equilibrium with their vapor under ambient gas pressures has become a well-known routine. However, it still requires sophisticated and complex instrumentation like vacuum liquid microjet [34-37], since electrons emitted from these highly volatile liquids undergo multiple collisions with both the vapor and liquid molecules until reaching the electron detector and results in significant decrease of signal to noise ratio.

On the other hand, liquids with the low vapor pressures such as ionic liquids (ILs) and some of low molecular weight polymeric compounds, which do not evaporate even under the UHV conditions, can be used in UHV XPS in order for better understanding of many processes involving liquids. [38-40]

1.1.4.1. Ionic Liquids

1.1.4.1.1. General Properties and applications of ionic liquids

Ionic liquids (ILs) are molten salts with melting temperatures lower than 100^{o}C.[42] They are composed entirely of anions and cations, exhibit unique properties like nonvolatility, high thermal stability, ionic conductivity as well as air and water stability. The wide diversity in IL structure, by changing either the cationic or the anionic components for a specific task, plays a major role in earning the name of “designer solvents”.[41] Hence, the appropriate selection of anionic and cationic components allows fine tuning of the ILs’ properties for particular purposes. It was shown in previous studies that there are more than 10^6 possible ILs arrangements. The most common cation moieties include the imidazolium, pyrrolidinium, pyridinium and ammonium based structures with varying alkyl groups. In addition, the most common anions used in literature are hexafluorophosphate, tetrafluoroborate, trifluoromethylsulfonate, bis(trifluoromethylsulfonyl)imide and trifluoromethylacetate. Contrary to the conventional salts, in ionic liquids cationic parts have larger size organic structures while the anions are relatively small and more flexible. Due to this large size characteristic, low mobility of ions within the ILs’ medium is expected. Because of these unique properties, ILs have many applications including energy storage and conversion, extraction and separation processes.[42,43]

The first and most abundant usage of ionic liquids in the field of energy materials is being an electrolyte solution. Conventional aqueous salt solutions, as

electrolytes in any electrochemical system, suffer from the volatility and safety problems in high operating temperatures and voltages. However, ionic liquid electrolytes are safe and green alternatives for conventional solutions.[44] Another important characteristic of ionic liquids for application in electrochemical devices is being resistant to any possible electrochemical redox reactions, since the electrochemical windows of ionic liquids are reported to be in a wide window generally larger than 4 V.[45-47] In previous studies, imidazolium-based ionic liquids were used to form ionic liquid electrolytes for rechargeable aluminum batteries.[48,49] For example, in 2015 Meng-Chang Lin et al. reported on a rechargeable aluminum battery that uses aluminum metal as the anode and graphite as the cathode with an ionic liquid electrolyte made of the mixture of aluminum chloride salt and ethylmethylimidazolium chloride [EMIM][Cl].[50] Variety of ionic liquids, especially those with quaternary ammonium cations are also used in lithium ion batteries by dissolving a lithium salt resulting in the formation of a new ionic liquid consisting of two cations.[51,52] Similar to the batteries, ionic liquid electrolytes are intensively used in electrochemical double layer capacitors.[53,54] In addition of using ionic liquids as electrolytes, they are also used as carbon precursors for carbonization of N-doped carbon materials, which display unique features such as high surface area, high chemical stability, and low cost, for many applications such as lithium ion battery, capacitor electrodes and electrocatalyst.[55-57]

Apart from the energy applications, ILs are used to form various stable metal nanoparticles with a number of different synthetic methods such as the chemical or

photochemical reduction from a metal precursors or electrodeposition.[58-63] Besides being a medium for nanoparticle synthesis, it was shown by many studies that ILs also help to stabilize nanoparticles by attaching them and forming a protective layer.[64]

1.1.4.1.2. Ionic Liquids and XPS

As was mentioned in early sections, implementation of lab-based X-Ray Photoelectron Spectroscopy to analysis of traditional liquids is not possible mainly because of their high vapor pressures. However, unique properties, that ionic liquids exhibit, make them compatible for XPS analysis. First of all, they nearly have no vapor pressures and do not evaporate even under the UHV chamber of the XPS.[65] Secondly, since they are composed only of ions, they have high conductivity; hence charging is not an issue for ionic liquids during data acquisition. Finally, they are also stable to X-Ray exposure. As has been reported in many studies, there is no observation on the beam damage of the sample, unlike many other organic based ones.

In the years 2005 and 2006, two different groups published the first reports on the study of imidazolium based ionic liquids by using X-ray photoelectron spectroscopy.[38,66,67] After that investigation of IL and IL-based samples with XPS had gained much more focus with the recognition of several other applications of ILs. Over the past decade, investigation of ionic liquids by XPS has been expanded to many other types of cations than the imidazolium such as pyrrolidinium[68,69],

pyridinium[70] and ammonium[71]. A well-defined fitting and charge correction through the referencing of alkyl carbon model was also established for IL-based XPS peaks[72] and used to understand the impurities and electronic effects (like anion-cation interaction[68], the anion basicity and cation acidity) by interpretation of the binding energy shift in the ionic liquids which are then extended to binary[73] and ternary[74] mixtures of ionic liquids.

In addition, molecular level investigations such as preferential orientation of ionic moieties were carried out by the technique of changing the emission angle, hence the surface sensitivity of the instrument (so-called Angle Resolved XPS (ARXPS)). [75-78] It is established that with increasing the grazing angle, the probing depth of XPS decreases and instrument becomes more surface sensitive. Thus, if the core level intensity increases relatively with the increasing grazing angle, it indicates the presence of the element in first layers of the surface. Using ARXPS, H. Peter Steinrück and co-workers showed that when Pt salt was dissolved in the imidazolium-based IL, Pt complex ions were concentrated on the top layer of the IL surface.[77] Similarly, ARXPS results with different alkyl chain sized imidazolium based ionic liquids suggested that alkyl chain of these ILs were oriented away from the liquid.[76]

With the recognition of ionic liquids as new generation electrolytes for many electrochemical processes, understanding of ionic liquid/electrode interface in operating conditions become a necessity.[78] For that reason, many efforts have been made to investigate the electrochemical double layers and other

characteristics of the interfaces (solid/liquid and liquid/vacuum). In one of the first studies, a drop of ionic liquid was placed on an angled electrode, which allowed the formation of a film thin enough to probe the IL/electrode interface.[79] The authors applied an external potential to the electrode and probed the electrochemical processes by tracing the shifts in binding energies. In our recent paper, we also reported on the effect of electrical double layer (EDL) and screening of ionic liquids used as an electrolyte for a simple coplanar electrical double layer capacitor device, using two gold electrodes.[27] We showed that when we applied a potential to the source electrode while we were grounding the drain, only half of the imposed potential prevailed on the IL surface all throughout the capacitor due to the formation of two similar but oppositely polarized EDLs at both electrodes.

1.1.4.1.3. *In-situ* Reaction Monitoring of Ionic Liquids

Monitoring of a particular chemical process of IL systems during the process carried out inside the analytical UHV chamber (which is called as *in situ* XPS) is more preferable than the steady state analysis because it also gives the time-resolved information about the process including intermediate states. Although this kind of analysis can be vital for understanding of many organic and electrochemical reactions, such studies are still limited due to the unfamiliarity of such experiments. Lovelock et al. showed adsorption and temperature-programmed desorption of water on ionic liquids by tracing the intensity of O1s peak before and after the D_2O dosing. [80] Rubidium electrodeposition has also been followed by in situ XPS by

monitoring of the deposition progress as well as the decomposition of the ionic liquid during the process due to the high current passage. [81] With the so-called UHV spectroelectrochemistry, which allows monitoring the electrochemical reactions of ILs in situ at UHV, License and coworkers reported on the electrochemical reduction of Fe(III) to Fe(II) in an ionic liquid mixture.[40] In situ electrochemical XPS has also been used to identify the electrochemical generation of Cu species and monitor their surface diffusion with a continuous collection of data as a function of time.[39]

In our research group, in situ preparation of gold nanoparticles (NPs) in UHV chamber was demonstrated using a simple electrochemical device configuration where an ionic liquid, which served both as reaction and as stabilizing medium for the nanoparticles, was placed between two electrodes. It was also shown that gold NPs were created from the gold electrode using an anodically triggered route.[62]

In a more recent study, we showed an in situ electrochemical reduction of imidazolium based ionic liquids to N-heterocyclic carbenes within the XPS chamber, [82,83] by using a simple electrochemical device. In that study, we have placed a drop of ionic liquid as the electrolyte and also the electro-active medium between two gold wire electrodes. We collected snapshot spectra of N1s region on the selected line from the source towards to the drain electrode in different reaction times. We demonstrated the generation of the carbene intermediate inside the XPS analysis chamber by electrochemical reduction of two different imidazolium based ILs with different anionic parts through the application of a 3V DC bias from the

source electrode. We showed the direct spectroscopic evidence as the appearance of a new neutral N1s peak representing the carbene in a lower binding energy on the negatively polarized end of the electrochemical device after 2-3 hours, as depicted in Figure 8.

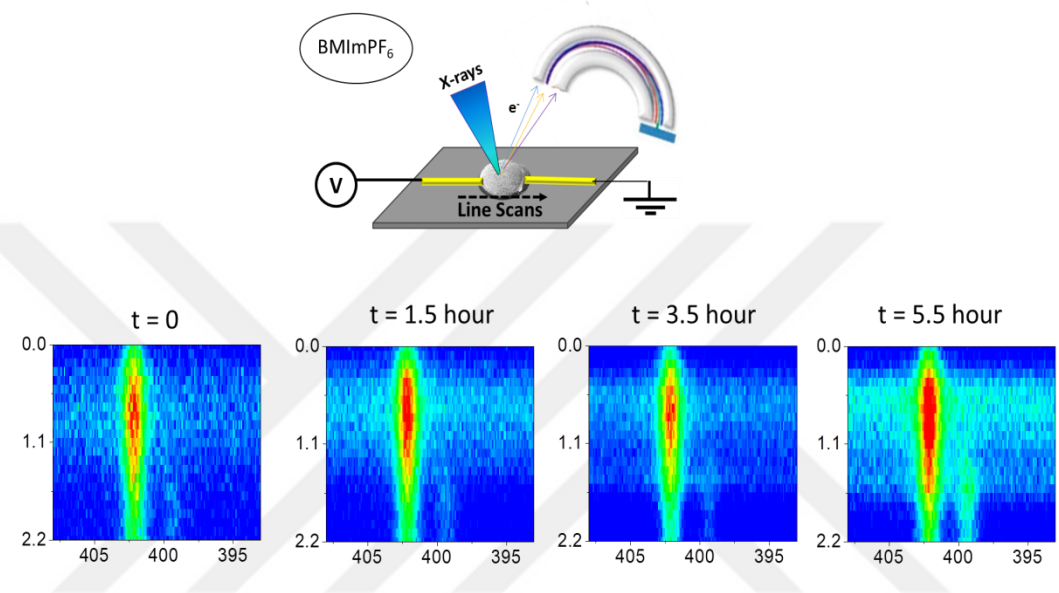

Figure 8 XP N1s spectra of [BMIM][PF_6] during the electrochemical process. The spectra are recorded in the line scan mode, at different time intervals and across the two gold electrodes. *Adopted from Ref [82] with permission from the Centre National de la Recherche Scientifique (CNRS) and The Royal Society of Chemistry.*

1.1.4.2. Low Volatile Organic Solvents

Apart from the usage of ionic liquids *in vacuo,* there are also some other organic liquids which have vapor pressures compatible with UHV experiments. Especially some of glycols, fatty alcohols and esters such as isopropyl palmitate, polyethylene glycol, searyl alcohol have low vapor pressures ranging from 10^{-5}-10^{-7} mm Hg at 20 °C.[84] These organic compounds have intensively been used in

personal care products as an emollient, emulsifier, moisturizer and thickening agent. [85,86] They are also non-toxic, biodegradable and have considerable potential in the usage of droplet-based microfluidics for biological applications.

In this thesis, we particularly have focused on the liquid polyethylene glycol (PEG). PEG is well-studied and commonly used in various applications for reasons including: (i) physical properties of PEG, (ii) coordination of PEG solutions which is also known as PEGylation, (iii) applications of low molecular weight liquid PEG as a green solvent in chemical reactions.[85] Polyethylene glycol is available in different molecular weights. PEG with molecular weight lower than 600 Da, is a colorless viscous liquid which is water soluble and hygroscopic. However, for molecular weights larger than 800 Da, PEG appears as a waxy, white solid. Liquid PEG is miscible with water and unlike any other organic solvents, PEG and water forms a monophasic solution. PEG is also known as polyethylene oxide (PEO) depending on its molecular weight. PEO is generally used for the solid form compounds with molecular weights larger than 800 Da.

1.2. Electrowetting

(This part is partially described in Aydogan Gokturk, P., Ulgut, B. & Suzer, S. "DC Electrowetting of Nonaqueous Liquid Revisited by XPS". Langmuir 2018, 34, 7301-7308. https://pubs.acs.org/doi/10.1021/acs.langmuir.8b01314
Reprinted with permission from Ref 54 Copyright 2018, American Chemical Society.)

1.2.1. Fundamentals of Electrowetting

Wettability is one of the most important features to describe the characteristic of surfaces and the contact angle (CA) measurement is the most common methodology to study wettability of surfaces.[86] CAs less than 90^{o} correspond to high wettability, while CAs larger than 90^{o} correspond to low wettability.[87] Ideally, surface tension of the liquid determines the shape hence the contact angle of a liquid droplet sitting on the surface. For a pure liquid, each molecule in the bulk experiences equivalent forces from every direction by neighboring molecules. In such case, the net force become equal to zero.[87] However, the molecules that are exposed to the surface, do not have neighboring molecules, which results in nonzero net force and creates a surface tension. As a result, in order to minimize the surface free energy, the liquid contracts and retains the minimum surface area. For many decades, numerous experimental methods have been developed to control the wettability of surfaces since in many applications, active control of the wettability is very crucial. Coatings of surfaces with polymers that are known to be hydrophobic character such as Teflon or other

fluoropolymers [88], introducing surface roughness by addition of grooves [89] or even nano-sized features [90] (which shows to enhance the wettability) are some examples of these methods. Electrowetting (EW) is another method to achieve the control of wettability. EW is a process of changing the contact angle and wetting of a surface with an application of external electric field.[91,92] In the conventional electrowetting set-up, a sessile drop sits on a planar electrode while a thin wire of counter electrode is inserted into the drop from the top. This classical set-up allows the passage of current and electron transfer which limits the contact angle change because of the possible electrochemical reactions and also the electrolysis of the liquid. In order to overcome this problem, the device geometry is further improved by an insertion of a thin dielectric film between the droplet and the planar electrode in order to achieve the larger amplitudes of contact angle change by preventing the faradaic current hence the possible side reactions[93-95]. This latter process is called electrowetting on dielectric (EWOD). EWOD process follows the Young-Lipmann's equation given below:

$$\cos\theta = \cos\theta_0 + \frac{1}{\gamma_{LG}}\frac{1}{2}cV^2 = \cos\theta + \frac{\epsilon\epsilon_0}{2\gamma_{LG}t} \qquad \text{(Equation 1)}$$

where θ is the final contact angle due to the applied potential, θ_0 is the initial contact angle at zero voltage, c is the capacitance of the dielectric, γ is the surface tension of the liquid, V is the magnitude of the applied voltage, t is the thickness of the dielectric layer, ϵ and $\epsilon_0$are the relative permittivity of dielectric and vacuum, respectively.

According to the Young-Lippmann equation, increase in the magnitude of voltage in EWOD geometry can produce quite changes in contact angle. However, application of high voltages is not feasible for many applications. That is why, achieving low voltage electrowetting, which is generally defined as the contact angle change with an applied voltage lower than 20V, is crucial.[93] Based on the same equation, three parameters can be manipulated to minimize the applied potential for desired contact angle change. The first method is to increase the relative permittivity of the dielectric layers. The second approach is to decrease the thickness of the dielectric layer which is challenging since it may cause undesirable dielectric breakdown. The final technique is to enhance the initial contact angle under zero voltage. This can be done by further coating the dielectric layer with another thin hydrophobic (i.e., Teflon or other fluoropolymers) layer which also provides better visualization of contact angle changes,[96] see Figure 9.

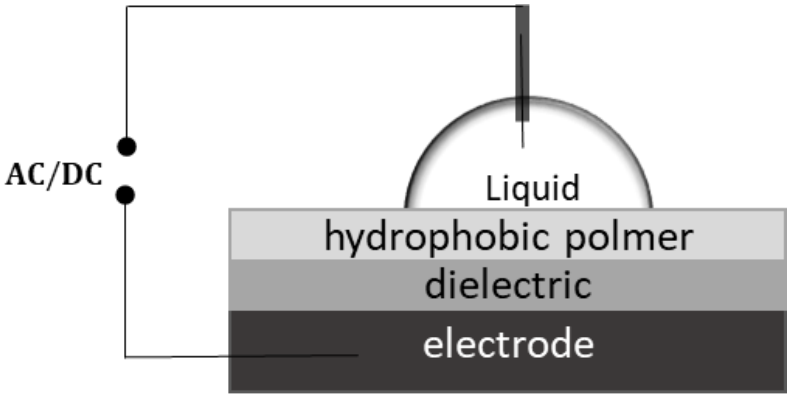

Figure 9 Schematic representation of an electrowetting on dielectric device with a hydrophobic layer between the dielectric and the liquid

Contact angle can be tuned both under the DC and AC excitation. One of these two methods can be preferable depending on the application due to their own characteristic pros and cons.

1.2.1.1. Challenges in EWOD

One of the major obstacles in electrowetting is related with saturation of the contact angle at high voltages, and numerous techniques have been developed to prevent or minimize this effect.[97-99] According to Young-Lipmann's equation, the contact angle continuously decreases with increasing voltage and eventually drops to zero. However, in practice, it is not the case. Many reports have shown that with high voltages, contact angle reaches to the saturation, which limits further contact angle modulation. The physical origin for saturation of contact angle is still not clear and has been studied intensively over the years. One of the mechanisms that was proposed for this phenomenon is the so-called charge trapping model. According to this model, above a certain voltage value, charge is injected from liquids to the solid. This injection of charge diminishes the charge on the liquid created by the external source and results in less efficient electrowetting. [100] Permanent trapping of charge carriers were shown to occur at the fluoropolymer surface and increased with aging of substrates in water as well as in various non-aqueous polar liquids.[101] Dab Klarman et al., proposed a different approach based on the free energy of capillary and electric contributions to explain the contact angle saturation and numerically determine the saturation angle.[99] Other explanations for contact

angle saturation involves ionization of air ambient[102] and diminishing the surface energy between the solid and liquid interface to zero[97].

Additionally, dielectric breakdown is another process, which is also an obstacle for many EWOD applications, which also contributes to the contact angle saturation. Dielectric breakdown can be minimized through improving the dielectric strength and chemical inertness of the insulating layers. In order to achieve good quality dielectric layers, many polymers, inorganic and even ferroelectric insulator materials have been used in previous studies such as PVDF-HFP[103], silicon nitride[104], parlylene-N and parlylene-C[105], Teflon films[101], polystyrene[106] and barium strontium titanate[107]. It was previously shown that an addition of thin hydrophobic layer provides a good electrowetting behavior. Ying-Jia Li and Brian P. Cahill used a multilayer dielectric stack instead of a single layer to increase the performance of EWOD device at low voltages.[108] In 2017, Shirinkami et al., showed the enhancement in the performance of EWOD devices through delay in dielectric breakdown by chemical mechanical surface polishing.[109] In their article, Vinayak Narasimhan and Sung-Yong Park demonstrated that an ion gel material, which consist of a copolymer poly(vinylidene fluoride-*co*-hexafluoropropylene) and an ionic liquid, ethylmethylimidazolium bis(trifluoromethylsulfonyl) imide ([EMIM][TFSI]), can be used as a high-capacitance dielectric for low-cost EWOD applications.[95] Lately, instead of a solid dielectric layer between the liquid droplet and underlying electrode, a new approach is introduced which uses liquid-infused films as the dielectric layer, where complete electrowetting and reproducible reversibility are achieved.[110]

However, once a certain voltage threshold is exceeded, the insulator, the liquid or even the ambient is likely to fail. Young-Lipmann's equation assumes that the liquid is perfectly conductive and dielectric is perfectly insulator. Violation of these assumptions in real life experiments introduces some challenges. Another limiting phenomenon, which has also been reported for the low conductivity liquids, is the contact line instability. It was previously shown by the Mugele and his co-workers that with high voltages, contact line of water-glycol mixture become unstable and emits small volume satellite droplets from the edge of the mother droplet [111], see Figure 10.

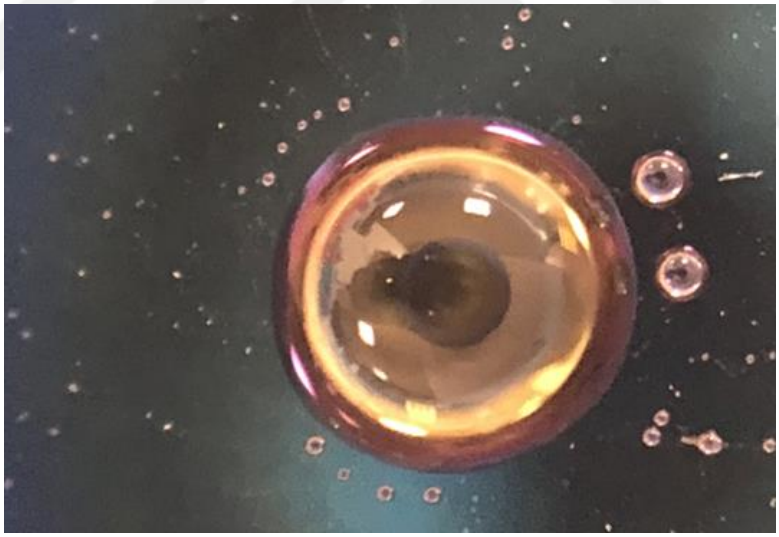

Figure 10 Picture of the contact line instability of polyethylene glycol drop under high voltages representing the mother and satellite droplets

1.2.1.2. DC Electrowetting

DC Electrowetting on Dielectrics is a simple yet an effective way to change the wetting properties of a substrate. That is why many efforts have been devoted to deeper understanding of the wetting mechanism. In the DC electrowetting, regardless of the sign of the applied DC potential, when the amplitude of potential increases the droplet electrowets the surface and decreases its contact angle[91], which is also modeled with Young-Lipmann's equation given above. However, contact angle values for negative and positive bias may slightly differ from each other. This asymmetry in electrowetting response has been shown to be related (when fluoropolymers are used as a dielectric for aqueous solutions) to the permanent trapping of charge carriers at the fluoropolymer surface, which increases with aging of substrates in water as well as in various non-aqueous polar liquids.[101]

1.2.1.3. AC Electrowetting

This part is "reproduced with permission from Langmuir submitted for publication. Unpublished work copyright 2018 American Chemical Society."

AC excitation is also preferred in many electrowetting applications because of a couple of advantages. First of all, it has been reported that the contact-angle hysteresis is smaller in AC than DC electrowetting. [106] Additionally, the contact angle saturation occurs at higher voltages and at smaller contact angles when

compared to the DC electrowetting.[98] It also was shown to reduce the ion adsorption at the liquid/dielectric interface.[112]

However, there are also additional phenomena which limit the applicability of AC electrowetting. The most important one is the frequency dependence change in the conductivity of the liquid and in the electrowetting behavior. In order to understand the frequency dependence of EWOD phenomenon under AC excitation, devices are conventionally modeled by an analogous equivalent electric circuit, which is depicted in Figure 11.[91,108,113,114] In this model, the liquid drop is represented by a parallel resistor and a capacitor, while the dielectric layer by another capacitor. This model is also supported by numerous electrical impedance spectroscopic data.[115]

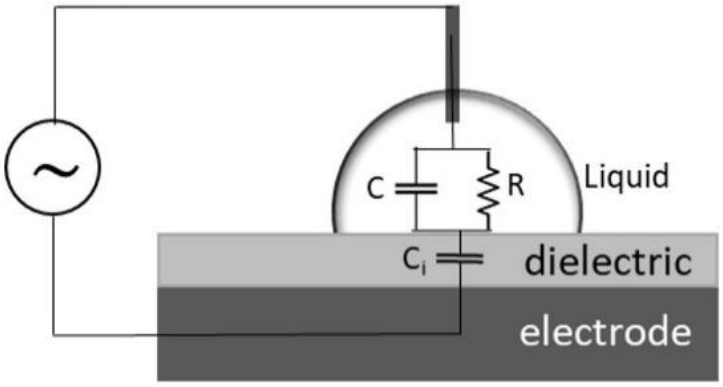

Figure 11 Schematic representation of the equivalent circuit diagram for a droplet on a dielectric-covered electrode.

Using this model for aqueous liquids, researchers have tried to understand the frequency dependent electrical behavior of EWOD phenomenon. According to the model and impedance studies, up to a certain frequency (in the low frequency

regime), capacitive component of the EWOD device determines the electrical behavior of the device, hence no voltage drop occurs in the liquid droplet but the entire voltage drops on the dielectric layer. At very high frequencies above the critical one, behavior is dominated by the resistive element of the device which is the droplet resistance, since studies shows decrease in the impedance modulus increasing the ionic concentration in the liquid droplet.[108] This behavior is attributed to the presence of the dissolved ions in the liquid, which can follow up the applied bias and screen the electrical field from the interior of the liquid up to a certain frequency, above which the voltage increase triggers formation of potential distribution within the droplet.[112]

The critical frequency between these two behaviors is determined by the following equation:

$$f_c = \frac{\sigma_l}{2\pi\left(\varepsilon_l + \varepsilon_d {}^{R}/_{d}\right)} \qquad \text{(Equation 2)}$$

where ε_l and ε_d are the electrical permittivity for the droplet liquid and the dielectric layer, respectively; σ_l is the conductivity of the liquid; R is the size of the droplet; and d is the thickness of the dielectric layer.[112] Beyond the critical frequency, a fraction of the potential that is applied to the wire drops within the droplet and results in the decrease of the effective contact angle change. [116]

In the classical electrowetting theory, the liquid is assumed to be a perfect conductor. This property can be achieved with the high ionic concentration. It was previously shown that even the deionized water can undergo electrowetting at low frequencies, but the critical frequency was reported to be smaller compared to the

aqueous ionic solutions.[114] The electric fields created within different type of liquids were calculated by T. B. Jones and K.-L. Wang[114] from elementary electrostatics. Using the Maxwell stress tensor they determined the height of rise of the liquid to model the CA change with varying frequencies.

Studies of Kwan Hyoung Kang group have shown formation of hydrodynamic flows within the droplet exposed to AC electrowetting and they have proposed some mechanisms for the origin of this flow. They analyzed the flow patterns in both the low frequency and high frequency regions, which appeared to be different from each other, for various horizontal displacement of the top electrode and correlated the numerically computed electric field inside the droplet with observed flows.[117,118] Such flows in electrowetting can be very useful for many microfluidic applications to enhance mixing of fluids.

1.2.2. Applications of Electrowetting Phenomenon

Electrowetting enables to manipulate the movement of small amount of liquids. Hence, this technology opens up new opportunities for various applications. One of these applications that use the idea of electrowetting is the display technology.[119-122] The term of “Electrowetting Display” was first presented by G. Ben, and S. Hackwood in 1981.[123] The concept is simple yet very efficient because it requires low potentials, has high reflectivity and high brightness.

The standard structure of an“ electrowetting display” device proposed first by Robert A. Hayes and B. J. Feenstra consists of the bottom electrode coated with an insulator and a hydrophobic layer, colored immiscible oil, water and top

electrode. In the absence of any potential, colored oil stays between the water and the hydrophobic coated electrode. However, when a potential applied, water moves to be in touch with the insulator, thereby displace the oil. Color switching of the electrowetting display is achieved through the visualization of interchanging between the colored oil film and the underneath electrode.[124]

Another application area is the lab on chip systems.[91] However, conventional electrowetting geometry with sessile drop configuration does not work for lab on chip applications. That is why, a thin electrode layer which is coated with hydrophobic polymer is used on the top instead of a wire counter electrode. The liquid is confined in between the two parallel substrates. The bottom substrate consists of series of individual electrodes to move the liquid in a designed pathway. Lab on chip systems can be used for moving, merging, mixing, and splitting of droplets.[125,126]

Electrowetting phenomenon was also used for development of liquid lenses. In the classical geometry, sessile droplet has a spherical shape in the liquid–vapor interface. Light passing thorough this interface is refracted based on the refractive index. Using electrowetting, this shape can be tuned.[91] In 2000, B. Bergea and J. Peseux [127] have reported on a first prototype configuration for liquid lenses which uses two immiscible transparent liquids one of which is a non-conducting liquid while the other is water. Insulating drop is in the drop shape and sits on a surface of the hydrophobized transparent window. When the potential is applied between the window and the water, the contact angle of the drop changes and

device works like a magnifying glass. The subject was recently reviewed by C-P Chiu et al. [128]

1.2.3. Electrowetting of Nonaqueous Liquids

In the literature, electrowetting is generally used to manipulate aqueous salt solutions. Few recent studies focus on the electrowetting of room temperature ionic liquids (RTILs). In 2006, John Ralston and his co-workers reported the first observations about DC electrowetting of several imidazolium and pyrrolidnium based ionic liquids on Teflon AF surfaces.[129] They also showed that electrowetting in ILs are less efficient, but changing cation structure leads to significant changes in the electrowetting behavior and the asymmetry between negative and positive voltages is amplified in ionic liquids compared to aqueous solutions.[130] In another study, researchers analyzed several ionic liquids which are having either the common anion or cation and observed the efficient contact angle decrease up to 48^{o} for [OMIM][BF_4].[131] Later on, again the research group of John Ralston published another work where they focused on a particular ionic liquid [BMIM][BF_4] and observed electrowetting on Teflon AF surfaces in an immiscible liquid ambient.[132] They studied both DC and AC actuation with electrowetting dynamics and observed significant contact angle drop over 100^{o}. In the same year, another study demonstrating a better electrowetting performance of ILs under AC than the DC voltages was published.[133] Beside from the ionic liquids, low conductivity glycerol droplet was used by Mugele et al. in the typical

EWOD geometry to study the electric field and morphological changes on droplet.[111]

1.2.4. Dynamics of Electrowetting

Electrowetting and dewetting dynamics as well as actuation and flow dynamics are also other important features for many particular applications such as merging, mixing, and splitting of droplets. In literature, many experimental set-ups have been utilized to study this type of dynamics in electrowetting such as spreading sessile drop, Wilhelmy plate method and capillary rise experiments.[129,134-136] Effects of liquid properties and droplet size, and also the amplitude of applied voltage on the actuation time are studied intensively.[135] John Ralston and his coworkers studied the dynamic electrowetting of an ionic liquid in a solid ,liquid and another immiscible liquid system and showed that the characteristic time is 20 milliseconds for spreading and 35 milliseconds for retraction process. They described the dynamics by the hydrodynamic model for small contact angles and by the molecular-kinetic model for large contact angles.[132] Same group also studied the dynamics of electrowetting and de-wetting of five different imidazolium based ILs in a solid, liquid and air systems.[129]

1.3. Aim of the Study

As we stressed earlier, extending the old techniques on solid-state material investigation by X-Ray Photoelectron Spectroscopy to the nonaqueous and non-volatile liquids opens up new perspective for better understanding of the various concepts in electrical and electrochemical processes. Previously, we studied on an ionic liquid based device in simple electrochemical setup with coplanar geometry to understand the fundamentals of electrode/IL interface and to monitor some of important in situ reactions. However, there are still plenty of gaps to fill toward better understanding of other geometries. This doctoral thesis focuses only one particular application which is the electrowetting. Contact angle tunability with the potential is crucial and electrowetting offers an excellent option for manipulating small amounts of liquids. Studies about electrowetting generally focus on the water or aqueous salt solutions. Only few of them show the ability of ILs or other low volatile liquids to electrowet. Secondly, their ambient is air or another immiscible liquid like oil. Finally, there are only the computational studies or formulations to predict the DC and/or the frequency dependent potential developments and electrical fields on or around the sessile droplet. The main motivation of this thesis is to use static (DC) and dynamic (AC) XPS as a complimentary way for investigation of nonaqueous ionic liquid and polyethylene glycol based electrowetting devices under operating conditions. In order to that, basic electrowetting device configuration with a sessile drop geometry that can be analyzed in ultra-high vacuum chamber is prepared and transferred to the chamber first to carry out some conventional measurements. The first part of the present work focuses on the DC

electrowetting. Thus, the geometrical changes droplet undergoes due to the application of potential has been studied. However, the most important focus of this part is about tracing the electrical potential developments on and around the droplet, using the shifts in the binding energy positions of the core-levels representative of the liquid and/or the substrate in chemically specific fashion. This part also studies the dielectric breakdown and potential and geometrical changes associated with it. In the second part, potential responses of different type of liquids with different ionic contents under AC electrowetting have been investigated as well as the frequency dependence of this behavior. Last but not least, our experimental findings have been also supported by an equivalent circuit model to electrically describe the system under investigation, which is further used to generate simulated XPS spectral data to be compared with both computationally and experimentally using a mimicking device.

Chapter 2

2. Experimental

2.1. Materials

Poly(ethylene glycol) (PEG) with an average molecular weight of 600 Da, which is in its liquid form and has negligible volatility, was purchased from Merck and used as received. Electrochemistry grade ionic liquid Diethylmethyl(2-methoxyethyl)ammonium bis(trifluoromethanesulfonyl) imide (DEME-TFSI) was purchased from Sigma-Aldrich and was also used without further purification. Commercial amorphous fluoropolymer called CYTOP in Type M grade and perfluorinated CYTOP solvent were obtained from Bellex International Corporation. Si wafers with a nominal 300 nm oxide layer is used as the substrate for all devices. The water used in all experiments is Millipore deionized water with resistivity of 18 MΩ cm. Ethanol Absolute (>99.9%) from Merck used to clean the substrates.

2.2 EWOD Device Preparation

The Si substrate with a nominal 300 nm oxide layer is cleaned with ethanol and deionized water then dried under Nitrogen gas flow. A CYTOP layer of about 50 nm thickness was dip-coated on the silicon substrate from a solution having a 1:3 Cytop to solvent ratio for 15 minutes to make the surface hydrophobic and dried with Nitrogen gas. This hydrophobic surface now acts as the substrate on the planar dielectric coated electrode. 3 µL of PEG or IL drop was placed on top of this fluoropolymer using a micropipette just before the insertion of sample to the entry chamber of the XPS spectrometer in order to minimize the possible water adsorption of the PEG and IL droplets. Figure 12 shows the schematic representation of EWOD.

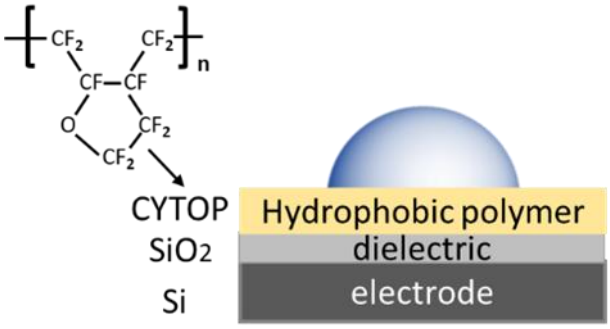

Figure 12 Schematic representation for a droplet on hydrophobized dielectric-covered electrode. (Adapted *with permission from Aydogan Gokturk, P., Ulgut, B. and Suzer, S. "DC Electrowetting of Nonaqueous Liquid Revisited by XPS". Langmuir 2018, 34, 7301-7308. Copyright 2018, American Chemical Society.)*

Finally, a thin copper wire was inserted into the droplet as the counter electrode to apply either the DC or AC potential.

2.3 Instrumentation

2.3.1 Characterization Techniques

2.3.1.1 X-Ray Photoelectron Spectroscopy

A Thermo Fisher K-Alpha X-ray Photoelectron Spectrometer with monochromatized X-rays of 1486.6 eV is used to collect all data for the XPS measurements. Spectrometer pass energies of 200 eV for the survey spectra and 50 eV for high-resolution spectra of all elemental spectral regions were used. X-Ray Spot size for areal and line scan measurements were set as 50 µm while for single point measurements as 100 µm. For the time-resolved XPS, fast data gathering mode snapshot was used instead of the scanning mode. The pressure in the analyzing chamber was always kept under 10^{-8} mbar. An external DC bias was applied using a Keithley 2400 Source Meter to the droplet or the Si substrate, see Figure 13. For pulsed as well as the frequency dependent AC measurements, a Stanford Research System Model DS340 Function Generator was employed and controlled with a LabView program developed in house, which also allows recording the current pass through the device. All data fittings were carried out by the Avantage software equipped with the instrument using 30% Gaussian and 70% Lorentzian product functions. Peak areas were calculated after Shirley background subtraction.

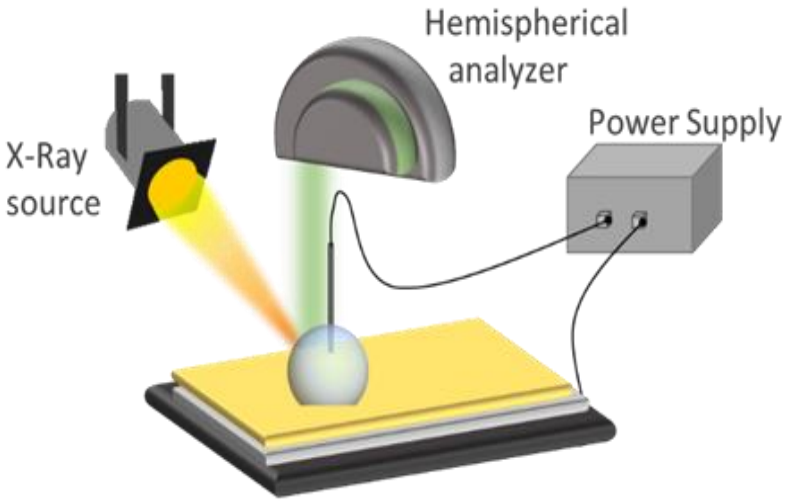

Figure 13 Schematic representation of the equivalent circuit diagram for a droplet on a dielectric-covered electrode *(Adapted with permission from Aydogan Gokturk, P., Ulgut, B. and Suzer, S. "DC Electrowetting of Nonaqueous Liquid Revisited by XPS". Langmuir 2018, 34, 7301-7308. Copyright 2018, American Chemical Society.)*

2.3.1.2 Contact Angle Meter

A DataPhysics OCA is used for contact angle measurements and drop shape analysis. Side-view images of the drops were obtained using a digital camera with zoom lens equipped with the instrument. The needle of the syringe was kept apart from the droplet and copper wire from the same EWOD device used for XPS analysis were used as a counter electrode. Figure 14 shows the schematic representation of EWOD device set-up in contact angle measurements.

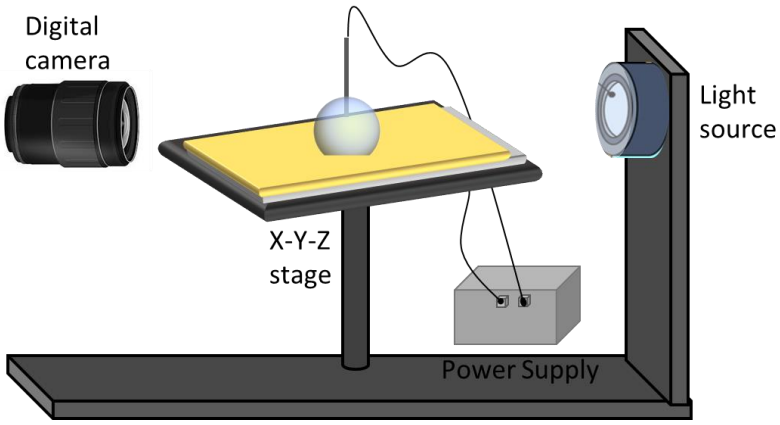

Figure 14 Schematic representation of the contact angle measurements of EWOD devices during the external electrical stimuli

2.3.1.3 Electrical Impedance Spectroscopy and Modeling

The same EWOD device that we described in the previous section is used to perform the Electrical Impedance Spectroscopy. Impedance data were measured using Gamry Interface 1000 with a zero DC bias voltage and a small AC (500 mV) perturbation. The frequency range was selected from 50 mHz to 100 kHz in order to overlap with the frequency used in XPS measurements. Measurements were done inside the Faraday's cage in order to increase the signal to noise ratio of data. Gamry Echem Analyst software was used to fit the impedance data to the equivalent electrical circuit. We, then generate the output voltage waveforms from the equivalent circuit with the simulation software, LT-Spice. Finally, these output waveforms are used to generate the XPS data from the ground state spectrum of respective element by using handwritten Phyton program.

2.4 XPS Analysis of Electrical Circuit Mimicking EWOD Devices

After the electrical measurements on the EWOD devices, a proposed equivalent electrical curcuit model is prepared for the XPS analysis. A mimicking device is fabricated through soldering of the commercial solid-state ceramic capacitors and resistors. Similar XP spectra with the EWOD device are recorded by using the Sn3d doublet peaks of the solder joints at different points on the circuit with same acquisition and frequency parameters to confirm and validate the reliability of the measured and simulated AC behaviors of the liquid.

Chapter 3

3. Results and Discussion

3.1. Characterization of the hydrophobic layer

A stylus profilometer is used to estimate the thickness of the CYTOP layer. For this type of thickness measurement, we prepared a hydrophobic CYTOP layer by dip coating the half of the sample in order to reach the uncoated parts too. Then, the stylus, which is in contact with the sample, was moved laterally across the sample for a specified distance beginning from the SiO_2 toward to the CYTOP layer. A profilometer measured the thickness of CYTOP as a function of position as in between 30-50 nm, see Figure 15.

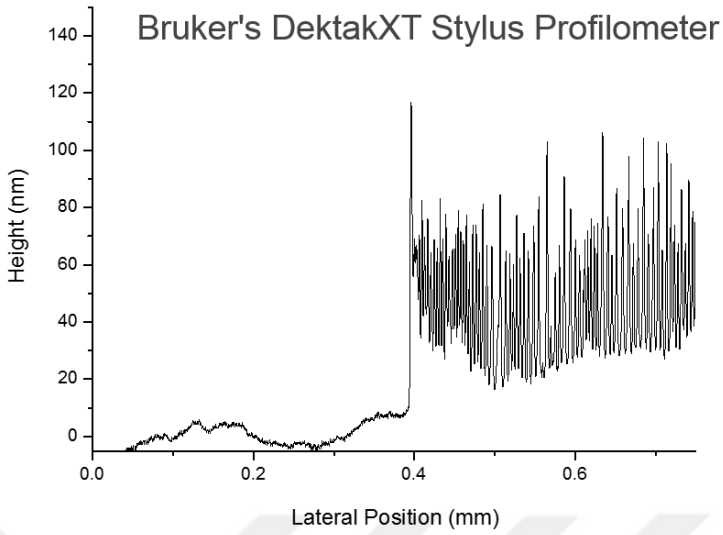

Figure 15 Thickness profile of the CYTOP layer. (*Reprinted with permission from Aydogan Gokturk, P., Ulgut, B. and Suzer, S. "DC Electrowetting of Nonaqueous Liquid Revisited by XPS". Langmuir 2018, 34, 7301-7308. Copyright 2018, American Chemical Society.)*

Additionally, in order to check the hydrophobicity of CYTOP films, the water contact angle measurements were carried out with 5µl de-ionized water both before and after the dip coating. Figure 16 shows the side-view images of the drops on top of the SiO_2 (left) and CYTOP (right) substrates. Water contact angle increased from 66^o to 117^o which shows the enhanced dewetting after the fluoropolymer coating.

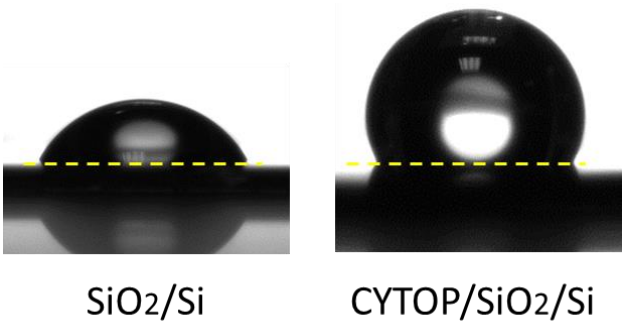

Figure 16 Side-view images of water droplet before and after the CYTOP coating

3.2. Conventional XPS analysis on EWOD Devices

The structure of Polyethylene glycol is H−(O−CH_2−CH_2)n−OH, hence the compound consists of only oxygen, carbon and hydrogen atoms. Since it is not possible to detect the hydrogen with the X-ray Photoelectron Spectroscopy only C1s and O1s peaks are detectable in the spectrum. A typical XPS survey spectrum and high resolution spectra of PEG , as given in Figure 17, confirms the stoichiometry of the liquid compound. The experimental ratios of total C : O : = 2 : 1 and it is in agreement with the theoretical value which is found to be 2.07 : 1 since the n in the structure is around 13 for the molecular weight of 600. In the C1s region, there is another peak in the lower binding energies which can be the indication of a minor surface impurities (adventitious carbon) since it has a much lower in intensity compare to the main peak.

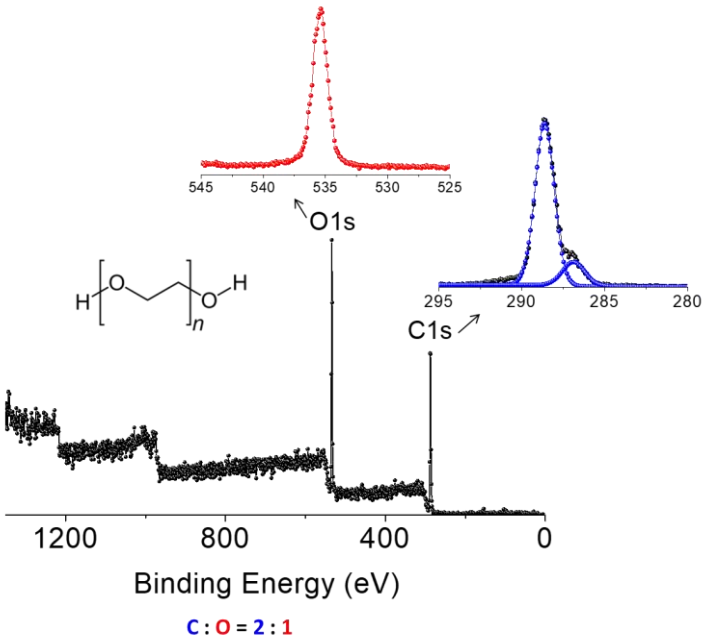

Figure 17 XP survey spectrum coming from the PEG surface with elemental regions in the high-resolution scanning mode.

On the other hand, ionic liquid we are using has a quaternary ammonium based cation and its formula is $C_{10}H_2OF_6N_2O_5S_2$. The survey XP spectrum of the IL from a selected position on the drop together with the detailed high-resolution spectra of all the elemental (S2p, C1s, N1s, O1s and F1s) regions and its molecular structure given in Figure 18. Survey spectrum shows only the peaks coming from the IL hence there is no indication of impurities. The S2p doublet peaks come only from the TFSI anion. O1s appears as a single peak, but the N1s XP spectra contains two distinct peak coming from the cationic as well as the anionic units specific to this IL. The N1s peak in higher binding energy at 402.0 eV, which is labeled as N+, comes from the quaternary ammonium. Other N1s peak at lower binding energy is assigned for the Nitrogen in TFSI anion. F1s region consists of a single peak originating from the CF_3 moieties of the anion with a high signal to noise ratio. Similarly, C1s region has a high signal to noise ratio, however, the measured spectra in this region is a convolution of four carbon atoms at different chemical environment which is fitted by considering the stoichiometric ratio of them. It is also worth saying that, in order to compensate the charging due to X-Ray illumination, the whole spectrum is shifted to set the aliphatic carbon labeled as C_1 to the 285.0 eV which is a well-known procedure adopted by researchers in the field.[38,66,68,71,72,78] The fifth Carbon peak at the highest binding energy position arises from the anionic part contrary to others. Peak area ratios are C1:C2:C3:CF_3= 2:2:4:2. Throughout this thesis, F1s region is chosen for this IL to follow the effect of other external excitations because it has high intensity and

contains only one peak that reduces the challenges for the conclusions drawn under bias contrary to in the case of C1s region.

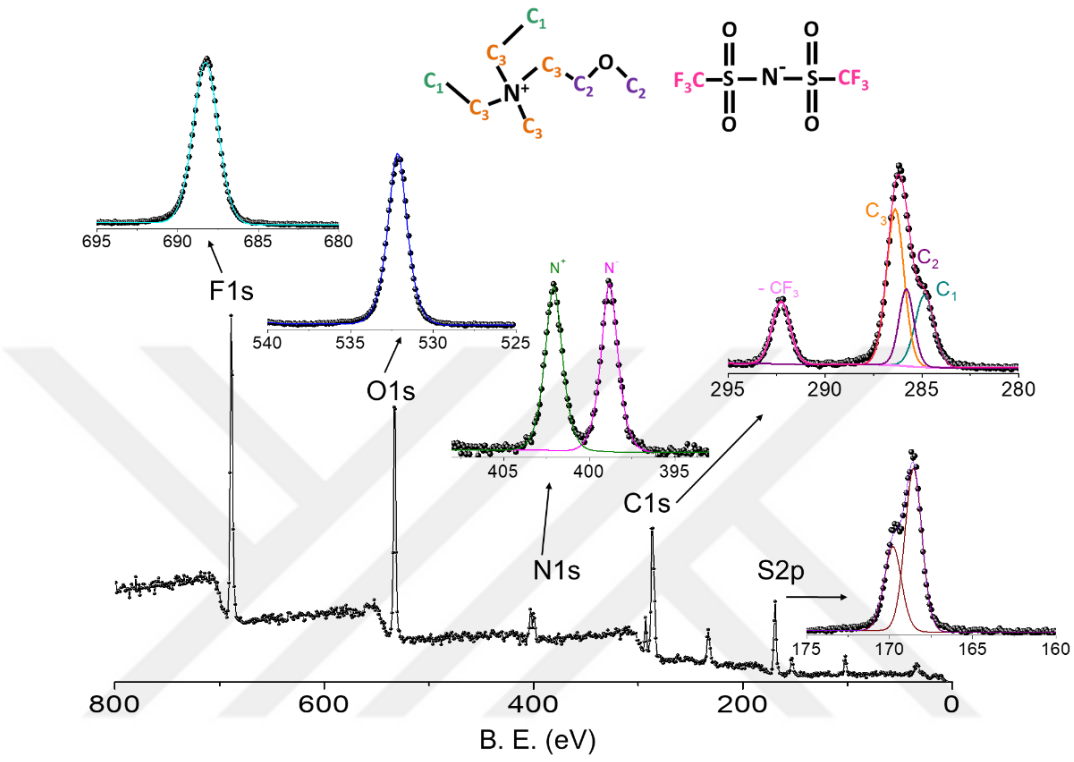

Figure 18 XP survey spectrum coming from the IL surface. The insets show various elemental regions in the high-resolution scanning mode

For the hydrophobic CYTOP layer, XP survey and corresponding elemental high-resolution spectra of elements are depicted in Figure 19. Single F1s peak comes from the -CF_2 and -CF substituents since the chemical shift between them are not resolvable. O1s also appears as a single peak. C1s region, however, includes two carbon atoms at different chemical environments. The stoichiometric ratio of the elements are measured as C : F : O = 6 : 11 : 1 which is close enough the expected one.

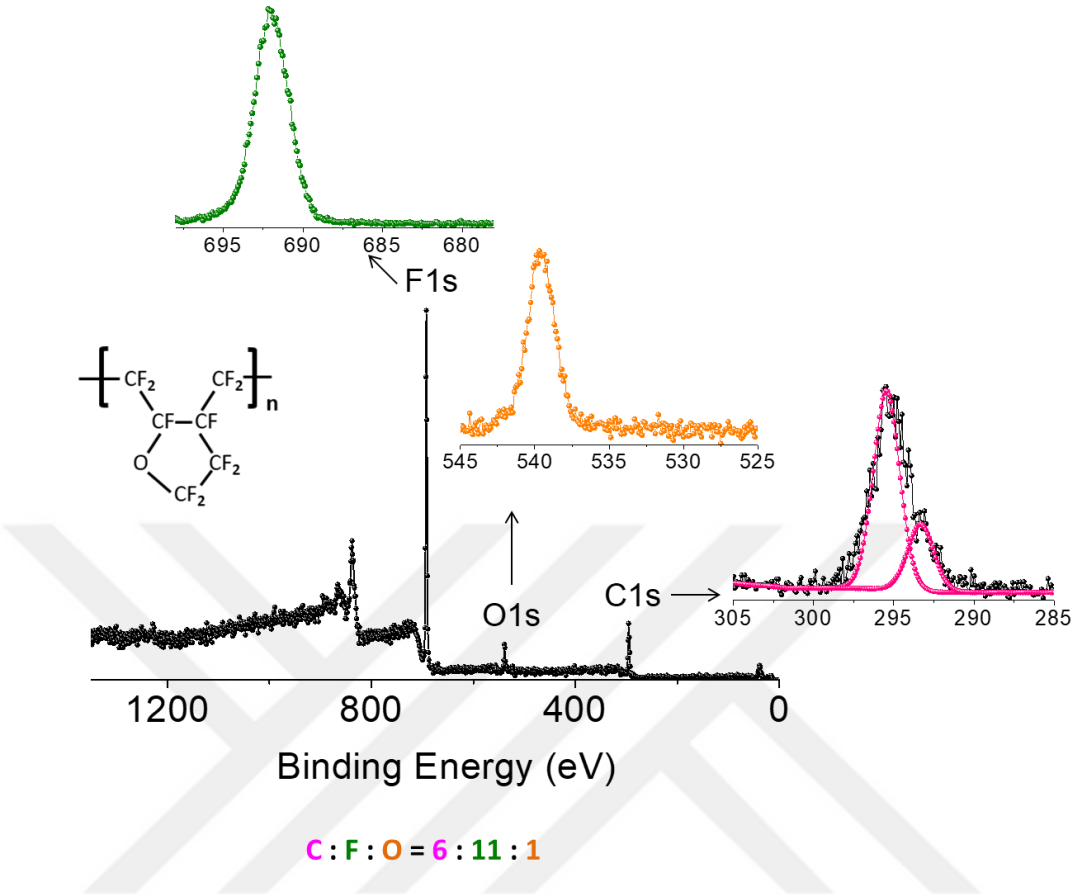

Figure 19 XP survey spectrum coming from the CYTOP surface. The insets show various elemental regions in the high-resolution scanning mode. *(Adapted with permission from Aydogan Gokturk, P., Ulgut, B. and Suzer, S. "DC Electrowetting of Nonaqueous Liquid Revisited by XPS". Langmuir 2018, 34, 7301-7308. Copyright 2018, American Chemical Society.)*

One of the other characteristic of the CYTOP aside from being a hydrophobic is its dielectric nature with dielectric constant of ~ 2. In addition, due to the positive charging of this hydrophobic and insulating surface under X-ray illumination, the measured position of the peaks differ about 1-10 eV than the expected value.

3.3. Electrowetting of PEG

(This part is also described in Aydogan Gokturk, P., Ulgut, B. & Suzer, S. "DC Electrowetting of Nonaqueous Liquid Revisited by XPS". Langmuir 2018, 34, 7301-7308. https://pubs.acs.org/doi/10.1021/acs.langmuir.8b01314
Reprinted with permission from Ref [137] Copyright 2018, American Chemical Society.)

3.3.1. Geometrical Changes in Air Ambient

First of all, in order to quantify the electrowetting behavior of PEG with DC voltages, we used the EWOD device described on the experimental section in air ambient. The applied DC voltage was increased gradually from 0V to 50V then back to 0 V and decreased from 0 to -50V gradually and contact angle values were calculated geometrically from the drop diameter and the height of the apex using the software of the contact angle meter. A "negative" applied potential corresponds to (-) voltage at the electrode underneath the substrate, and 0 V at the inserted wire. Figure 20 shows the contact angle changes in various amplitudes of the applied potential. DC voltage dependence of contact angle graph shows contact angle saturation after 20V. Thus, the change in applied potential causes very little changes in contact angle as the applied voltage becomes larger and starts to deviate from the Young-Lippmann equation.

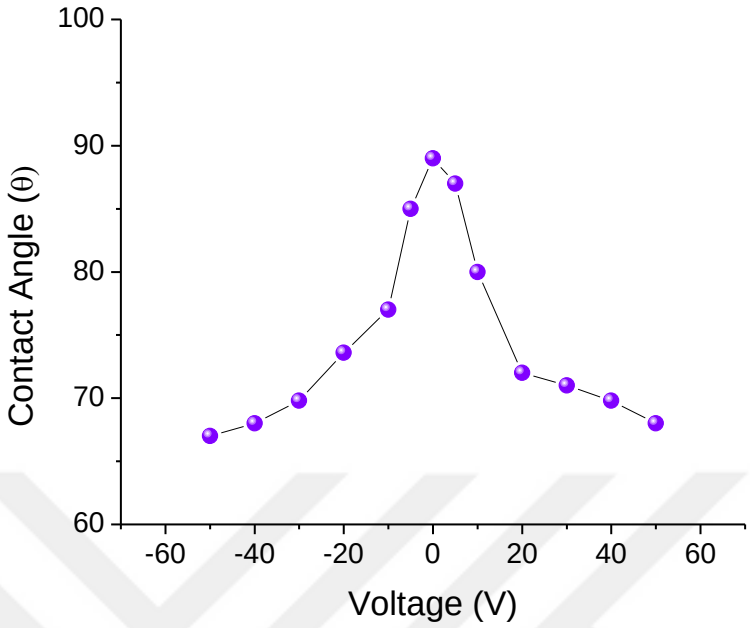

Figure 20 DC Voltage dependence of contact angle. The voltage was increased from 0 to 50 V, and then brought back to 0 V and decreased from 0 to -50V gradually.

Images of a PEG droplet under +50V, +10V, 0V, -10V and -50V in air ambient, are shown in Figure 21. The contact angle of the droplet on hydrophobic fluoropolymer is around 89^0 at 0V. When the applied potential becomes more negative or positive, the droplet electrowets the surface and decreases its contact angle.

Our contact angle values for negative and positive bias are slightly different. As we discussed in the introduction part, this asymmetry in electrowetting response has also been encountered in other studies and have been related to the charge trapping on the Cytop layer due to aging of substrates with polyethylene glycol.

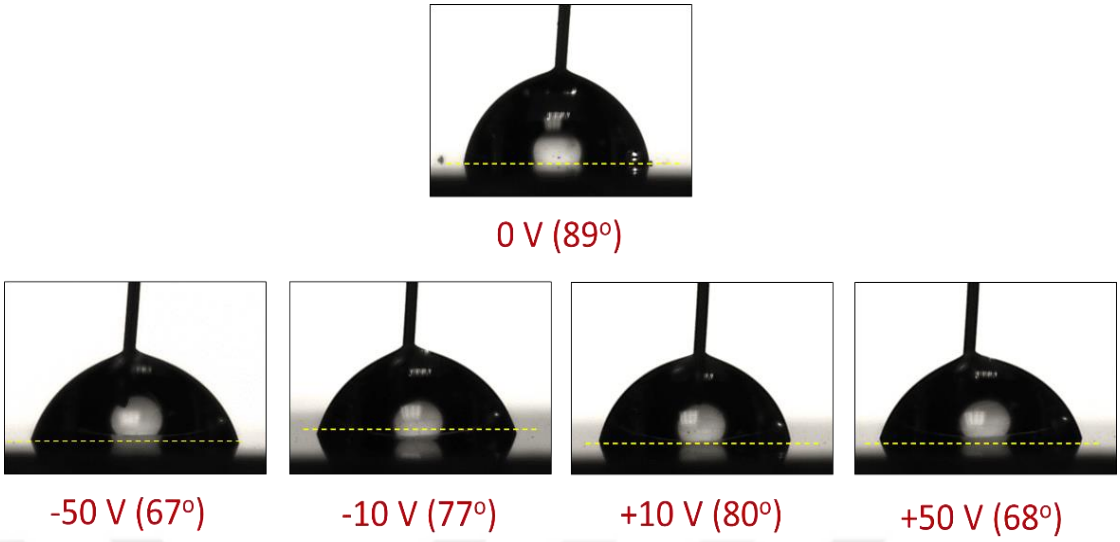

Figure 21 DC Voltage dependence of contact angle and shape of PEG droplet. The voltage increased from 0 to 50 V, and then back to 0 V and decreased from 0 to -50V gradually. *(Reprinted with permission from Aydogan Gokturk, P., Ulgut, B. and Suzer, S. "DC Electrowetting of Nonaqueous Liquid Revisited by XPS". Langmuir 2018, 34, 7301-7308. Copyright 2018, American Chemical Society.)*

3.3.2. Geometrical Changes in vacuo

To reflect the changes that the drop undergoes during DC electrowetting in UHV chamber, we collected C1s spectra from the area representing a droplet with the faster data gathering snapshot mode. Figure 22 displays an aerial map of C1s peak intensity with 50 µm X-ray spot- and 50 µm step-sizes, with and without the potential. Potential is applied from the bottom silicon electrode while the drop is grounded from the copper wire.

To form this graphs, at first, XPS data is collected from the selected area in the C1s region between 278-298 eV. For the grounded sample, two types of C1s peaks are observed in the interface region. One of these peaks is broad and is

around 294 eV. This peak belongs to the substrate, while the other one is narrower, more intense and is around 286.4 eV originates from the PEG. Contrary to the grounded case, under 50 V bias, there is only one C1s peak, which is again around 286.4 eV, because application of the bias causes the carbon peaks coming from substrate to move out of the scanned range towards 50 eV higher binding energy values. In order to get information about the shape of the droplet, we selected the sharp PEG peak. Then, the entire collected spectra were fitted by imposing constrain to keep this peak's binding energy position constant at 286.4 eV, using the Avantage software. The resultant peak areas after fitting were extracted as a 2 dimensional areal matrix consisting of x and y coordinates with 50 μm steps and corresponding data for the each of x and y values. Finally this matrix was converted in to a color filled contour plot.

The left side contour plot of C1s represents almost a circular shape of the drop in the beginning with some distortion because of the inserted wire electrode to the droplet, convoluted with the angled X-rays illumination geometry. Basal area of the drop is estimated for each case as shown in Figure 22 by counting the number of small and known areal which fit in the circular shape. For the grounded case, the base area is ~5.8 mm^2. Under the +50V bias, the drop expands, distorts further and also moves without breaking its electrical connection. Base area of the drop after the +50V is estimated as ~6.7 mm^2. This corresponds to a 17% increase in the initial area.

We used this %17 increase to find the change in the contact angle. We first found the change radius of the droplet:

$\left(\frac{A_i}{A_f}\right) = \left(\frac{r_i^2}{r_f^2}\right) = 0.86$, $\frac{r_i}{r_f} = 0.93$, $r_i \cong 1.5\ mm$ from the contour plot,

then $r_f \cong 1.61\ mm$

After that, we assumed that volume of droplet is constant during the electrowetting process, the height of the drop can be calculated as follows:

$V_i = V_f$,

$\frac{2}{3}\ \pi h_i\, r_i^2 = \frac{2}{3}\ \pi h_f\, r_f^2$

$\frac{h_i}{h_f} = 1.16$

Geometrically, the contact angle can be calculated from the drop diameter and the height of the apex;

$$\frac{\theta}{2} = \tan^{-1}\left(\frac{h}{r}\right)$$

$$\frac{\theta_i}{\theta_f} = \frac{\tan^{-1}\left(\frac{h_i}{r_i}\right)}{\tan^{-1}\left(\frac{h_f}{r_f}\right)} = \frac{\tan^{-1} 1.25}{\tan^{-1} 1} = 1.14$$

If the contact angle is 89^0 in the beginning as it is outside the x-ray photoelectron spectrometer chamber, then the final contact angle will be 77^0. Hence, this 17% geometrical change corresponds to $\sim 12^0$ change from the initial contact angle value. This change is smaller than the measurements outside the chamber, which might be related to the contact angle saturation phenomenon, since the drop had been exposed to several voltage cycles before this particular data was acquired.[42]

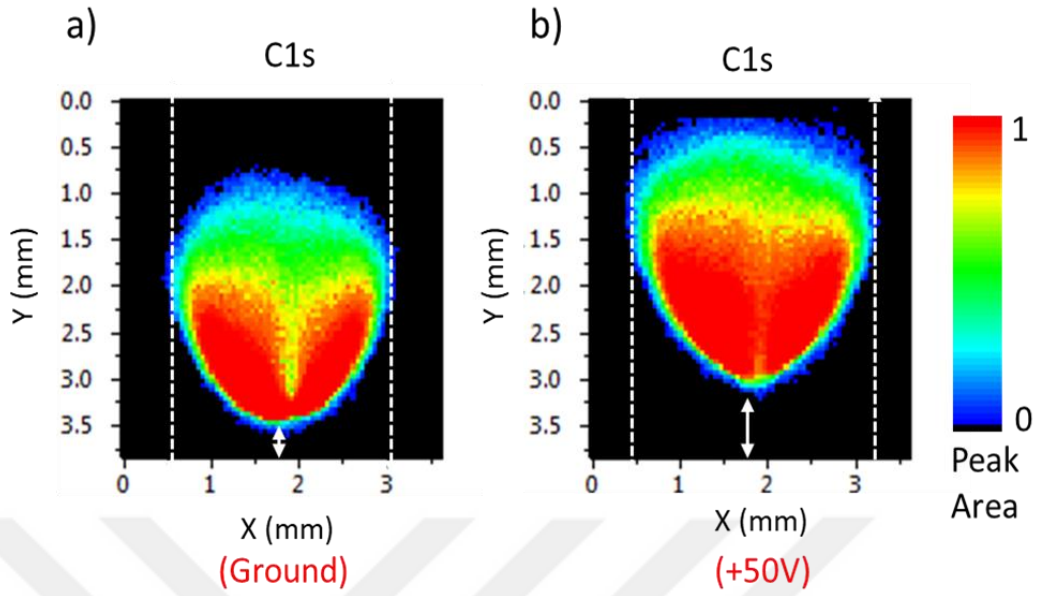

Figure 22 DC Voltage dependence of contact angle and shape of PEG droplet. The voltage increased from 0 to 50 V, and then back to 0 V and decreased from 0 to -50V gradually. *(Reprinted with permission from Aydogan Gokturk, P., Ulgut, B. and Suzer, S. "DC Electrowetting of Nonaqueous Liquid Revisited by XPS". Langmuir 2018, 34, 7301-7308. Copyright 2018, American Chemical Society.)*

After the steady state observations, in order to see the dynamic expansion and contraction of the drop, we carried out time resolved XPS analysis by the sequential gathering of O1s (representing the drop) and F1s (representing the rigid substrate) regions in the snapshot mode on a point at the PEG / substrate interface where both peaks are visible while we appied the successive -50V and 0V excitations with a constant frequency. Figure 23 shows the time dependent changes in intensities of the O1s and the F1s peaks. The cycle begins with application of a -50V at which the F1s peak appears around 650 eV (-50eV lower than its ground position), the drop expands and the intensity of the O1s peak (at ~532 eV) increases. When the voltage is brought back to 0V, the F1s goes back to

its original binding energy position and disappears from the observation window completely, and the intensity of O1s peak decreases but does not disappear completely.

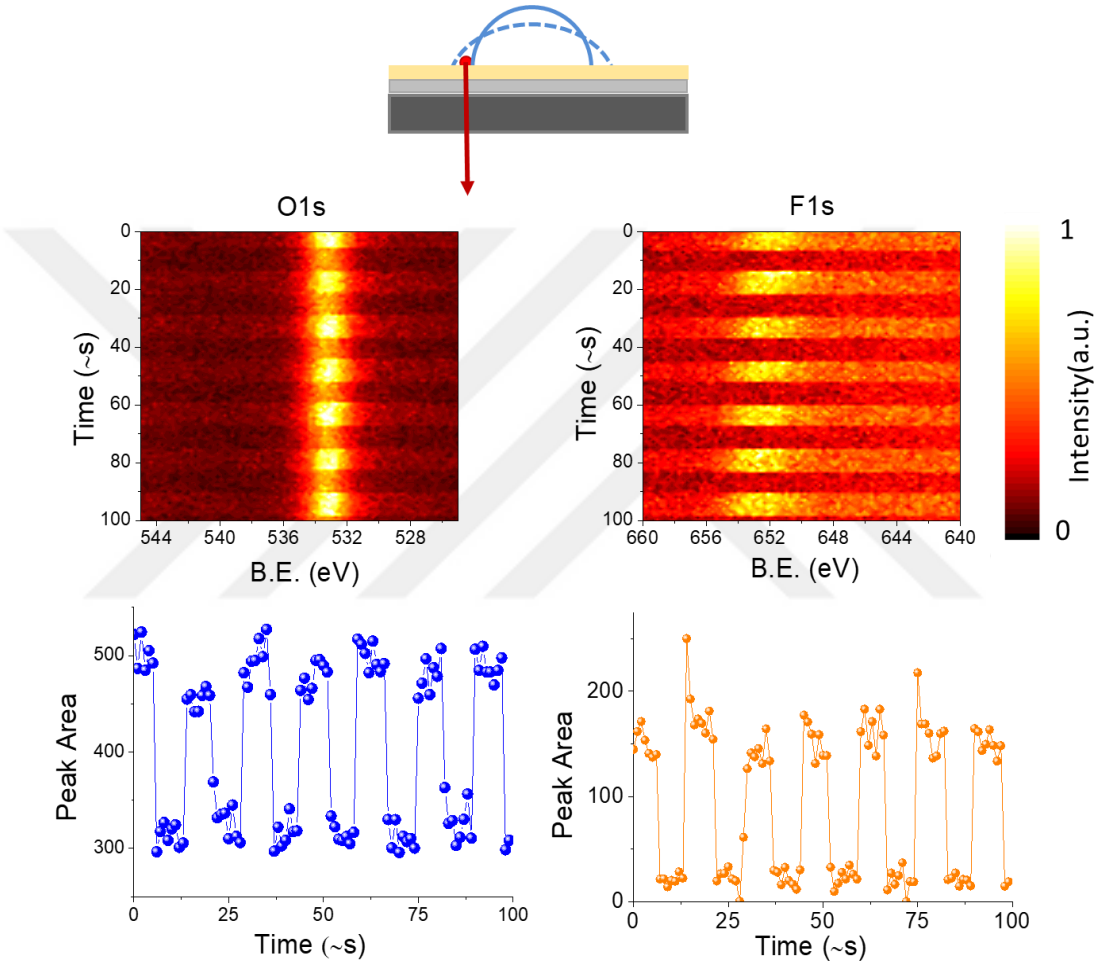

Figure 23 DC Voltage dependence of contact angle and shape of PEG droplet. The voltage increased from 0 to 50 V, and then back to 0 V and decreased from 0 to -50V gradually. *(Reprinted with permission from Aydogan Gokturk, P., Ulgut, B. and Suzer, S. "DC Electrowetting of Nonaqueous Liquid Revisited by XPS". Langmuir 2018, 34, 7301-7308. Copyright 2018, American Chemical Society.)*

3.4. Potential Developments Under DC Excitation

(This part is also described in Aydogan Gokturk, P., Ulgut, B. & Suzer, S. "DC Electrowetting of Nonaqueous Liquid Revisited by XPS". Langmuir 2018, 34, 7301-7308. https://pubs.acs.org/doi/10.1021/acs.langmuir.8b01314
Reprinted with permission from Ref 54 Copyright 2018, American Chemical Society.)

Understanding of the electrical field effect on the electrowetting behavior is of interest because literature is based only on the computational and theoretical work and lacks of experimental findings. Voltage-Contrast X-ray Photoelectron Spectroscopy with external bias is an efficient way to detect the potential developments on the EWOD device under its operating conditions due to its ability to detect, locate and quantify the potential developments on the surface.

Measurements for detecting the geometrical changes reported earlier also provide electrical information about the EWOD device under operation. However, they were obtained using the low resolution snapshot mode with 1 second intervals in order to catch the real time observation of the relatively fast processes occurring in a time window of a few milliseconds to a few minutes. To obtain higher precision, we have acquired data in the scanning mode, which is a slow process, and is the reason why it is generally used for a small number of data set, but with improved spectral quality. Accordingly, we collected C1s spectra on a selected line from the substrate surface to the middle of the drop under the DC excitation to the sample from the bottom Si electrode. C1s or O1s peak can be selected for analysis of the behavior of the liquid, since both peaks have large intensity, see Figure 17, and reveal the same conclusions. Hence, throughout this thesis C1s or O1s peaks will be

used interchangeably to represent the characteristics of PEG. Figure 24 shows the recorded line scan results of C1s at different applied bias (+50V, ground and -50V), along the line shown in the inset. As indicated from the figure, both the PEG and substrate peaks are visible in the spectra recorded at several positions at the interface region.

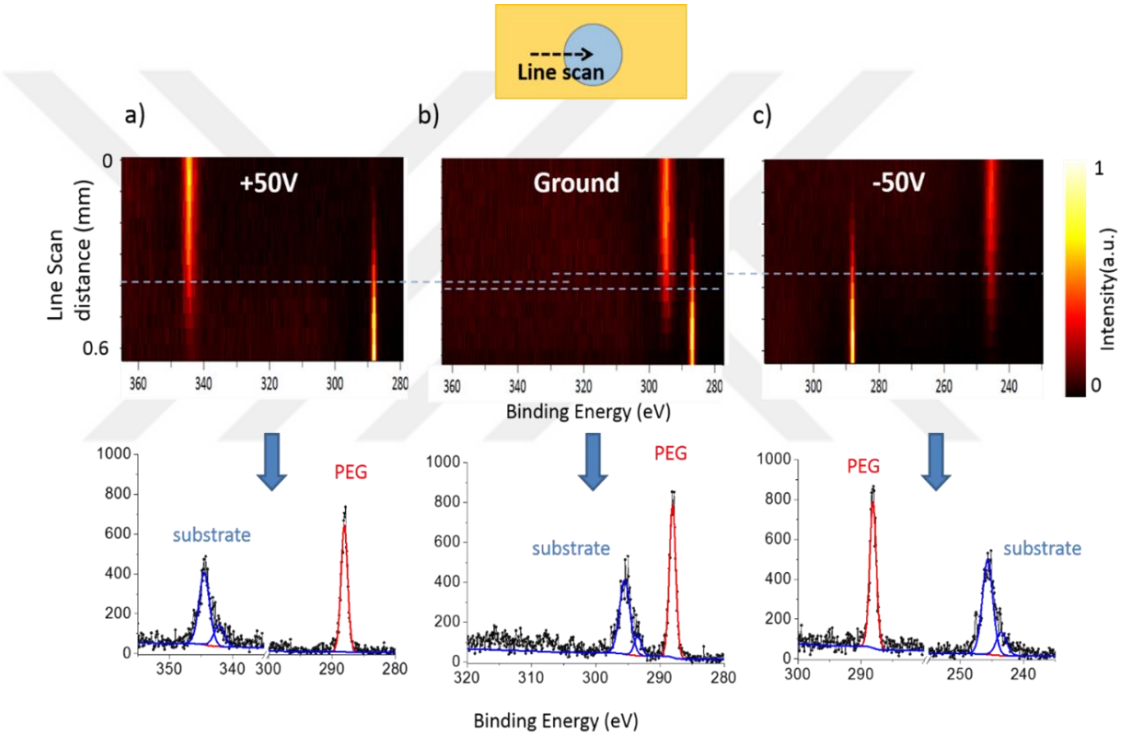

Figure 24 C1s spectra recorded at different applied bias, along the line shown in the inset. The lateral position of the liquid/substrate interface, determined by the region where both C1s features overlap, also moves with the bias. *(Reprinted with permission from Aydogan Gokturk, P., Ulgut, B. and Suzer, S. "DC Electrowetting of Nonaqueous Liquid Revisited by XPS". Langmuir 2018, 34, 7301-7308. Copyright 2018, American Chemical Society.)*

When both the bottom and the top electrodes are grounded, which is shown in the middle, the C1s region exhibit one broad peak, which includes multiple

components of the CYTOP such as C-F, C-F_2 and C-O, in the early positions of the line scan and a narrow peak representing the PEG liquid at 286.4 eV with a FWHM equal to 1.2 ± 0.2 eV. When +50 V or -50V bias is applied, the binding energy position of the narrow peak displays no shift with neither of the polarity of the bias, whereas the second peak coming from the substrate shifts in eV with the same amplitude of the bias. Expansion of the liquid on the substrate while it undergoes electrowetting with the bias is also observable by tracing the changes in the lateral position of the PEG/CYTOP interface. When the potential is applied, the drop wets the surface and expands on the substrate. This results in the movement of the interface to the earlier position of the line scan.

Interesting finding about the present geometry is that, surprisingly the entire potential drop occurs only at the substrate/liquid interface, which is contrary to our previous studies.[27,82,83] As we also mentioned in the introduction part, when we used ionic liquids as the medium between two electrodes, the F1s signal of the ionic liquid exhibited a constant and non-varying shift across the electrodes. However, the measured amplitude of the shift was dependent on the nature and the geometry of electrodes. For instance, with a symmetrical co-planar geometry where the device had two similar gold electrodes, the binding energy shift was only half of the imposed potential, since the applied potential drop was shared equally by the two equivalent electrode/electrolyte interfaces, which was attributed to the effective screening by the two similar electrical double layers (EDL) at the two interfaces.[27] For the asymmetric geometry as in another study, where one of the

electrodes was a thin metal wire while the other one was a plate, the shifts were higher or lower reflecting the nature of interfaces, and capacities of the EDLs.[83]

Similar to the EWOD of PEG, we also monitored the potential development on and around the specific IL (DEME-TFSI). IL device is prepared in the same geometry and procedure with PEG device. This device also displays a similar behavior such that the entire potential drop occurs only at the substrate/liquid interface, see Figure 25, which proves that the intrinsic characteristics of the drop used in EWOD geometry and also the conductivity have no effect on the electrical behavior of DC electrowetting. Additionally, geometrical changes upon electrowetting and spreading of IL on the substrate can also be probed from the same figure through the detection of the changes in the lateral position of the IL / CYTOP interface. With the external bias, interface moves to the early positions of the line scans similar to the observation in the PEG liquid.

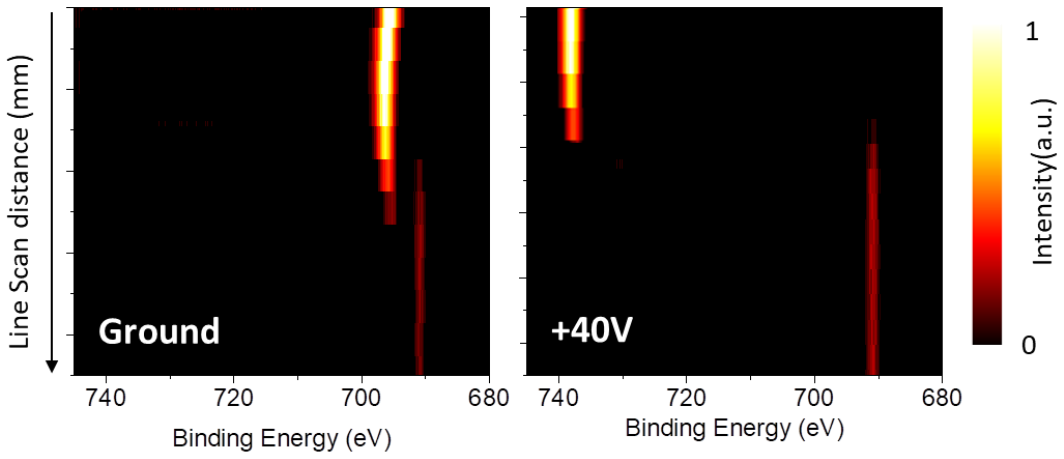

Figure 25 F1s spectra recorded at ground and +40V applied bias, along the line beginning from the substrate towards to the middle of the drop.

Potential drop upon reversing the electrical connection of the PEG device, where the bias is applied to the drop from the copper wire, while the planar electrode is grounded, is also checked. Similar behaviors are observed with this geometry too, where the C1s peak shifts promptly with the bias, and the F1s experiences no significant shifts, as given in the Figure 26. Again, the entire potential drop materializes on the liquid/ substrate interface while no potential drop is observed in the liquid/wire electrode interface.

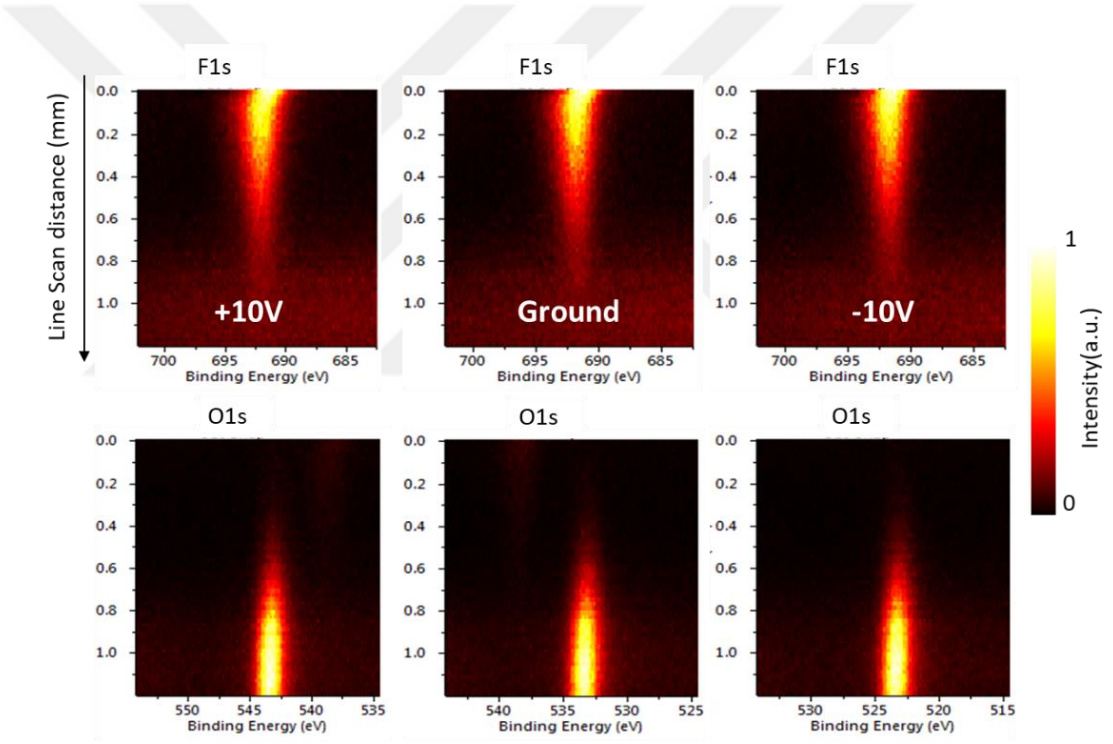

Figure 26 O1s and F1s spectra recorded at different applied bias, along the line beginning from the substrate towards to the middle of the drop.

We also checked the interface region in detail by tracing the binding energy of F1s from CYTOP and C1s from PEG with the application +100V bias from the wire, see Figure 27. As can be understood from the figure, while the F1s peak does not shift with the bias, the measured binding energy of C1s is shifted by 100.0 eV to 386.4 ± 0.1 eV along the entire line with no sign of additional broadening. FWHM values of C1s coming from the fitting results are also shown in Figure 27, with no indication of any significant change.

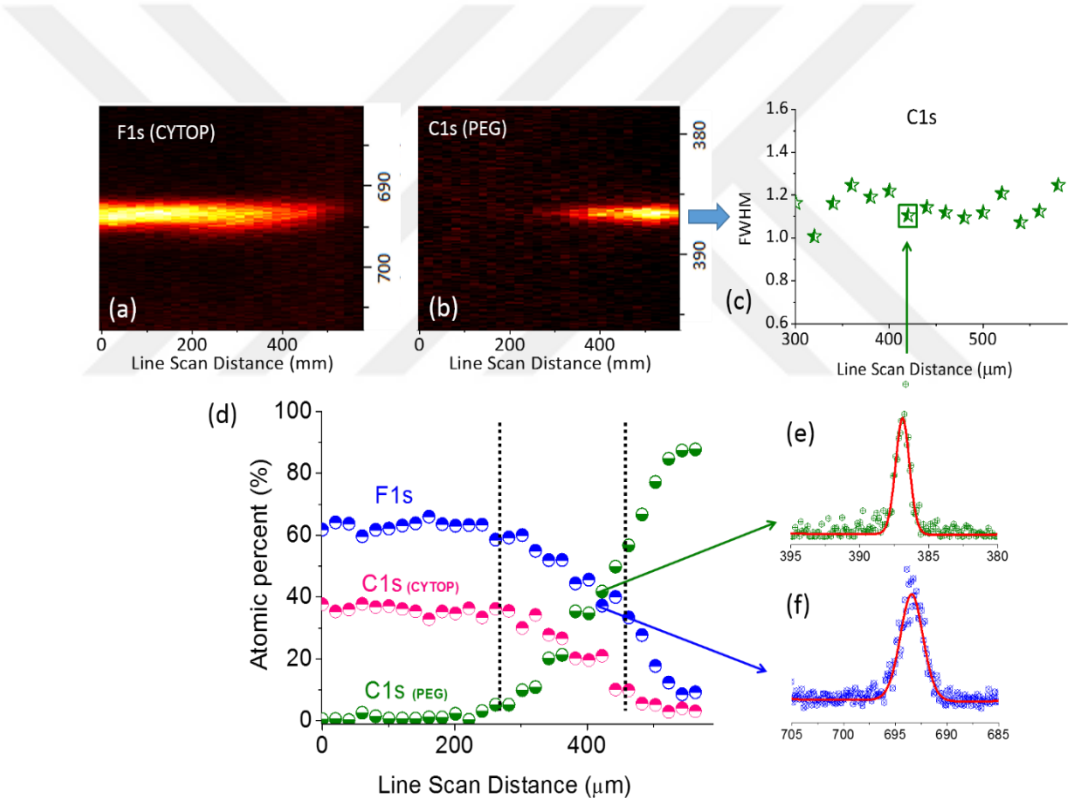

Figure 27 Line-scan spectra of; **(a)** F1s and **(b)** C1s regions, recorded under +100 V bias and with 30 µm spot and 20 µm step sizes, along a line into the drop. **(c)** Variations in the width of the C1s peak. **(d)** Atomic percentages computed. Representative spectra at the designated point; **(e) C1s** and **(d)** F1s. **(***Reprinted with permission from Aydogan Gokturk, P., Ulgut, B. and Suzer, S. "DC Electrowetting of Nonaqueous Liquid Revisited by XPS". Langmuir 2018, 34, 7301-7308. Copyright 2018, American Chemical Society.)*

In Figure 27, we also fitted the broad C1s (from CYTOP), narrow C1s (from PEG) and F1s peaks through the line in order to get the atomic percentages using the Avantage software. Surprising finding coming from this graph is related with the unexpectedly large interface region where the F1s and the C1s are both observable for ~200 microns which includes more than 6 steps with 30 μm spot size of the X-rays we used. This large interface region may be related to the previously reported wedge-like extension of the liquid on the substrate.[138-140] Moreover, this wedge-like extension seems to be still in full electrical contact with the drop since the C1s peaks from the interface have the same binding energy value with the main body of it.

Figure 28 shows similar measurements as in Figure 23 but with a faster snapshot acquisition, now used to probe the dynamics of the electrowetting and potential developments. These periodic alterations are fast, in orders of tens of milliseconds. This is surprising since polyethylene glycol 600 is a viscous liquid with a viscosity around 190 mPa.s which is known to decrease the response and the spreading time of the liquid under DC electrowetting.[141]

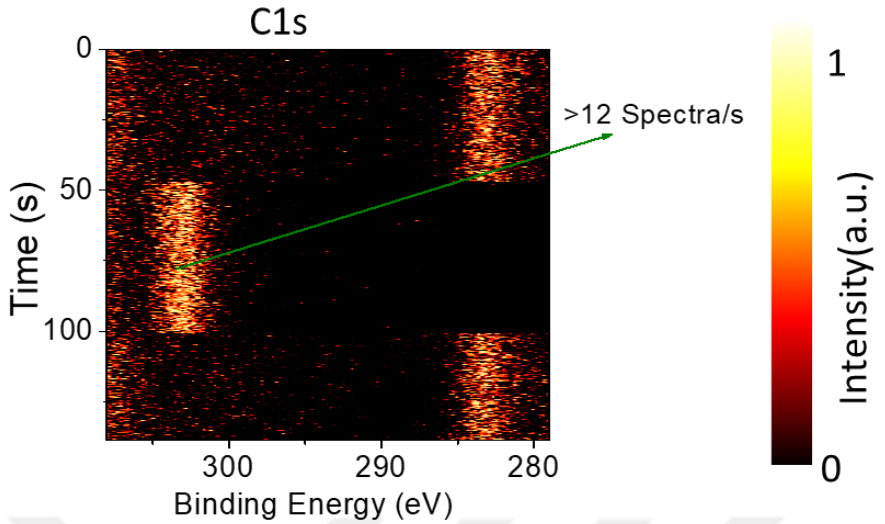

Figure 28 Time-resolved C1s spectra in a fast snap-shot mode (> 12 spectra/s) recorded under 10 SQW excitation

3.4.1. Dielectric Breakdown

With the top-gated device geometry where we applied the potential from the copper wire immersed on top of the drop, measurements leading to extract the potential developments on and around the liquid drop can be carried out up to hundred volts as long as the integrity of the vacuum system is preserved. We observed that with the increasing potential up to 120-130V, C1s peak from PEG shifts promptly with the same amplitude of the bias. Figure 29 shows the binding energy position of C1s peak under various biases with a perfectly linear behavior having a slope of 0.994.

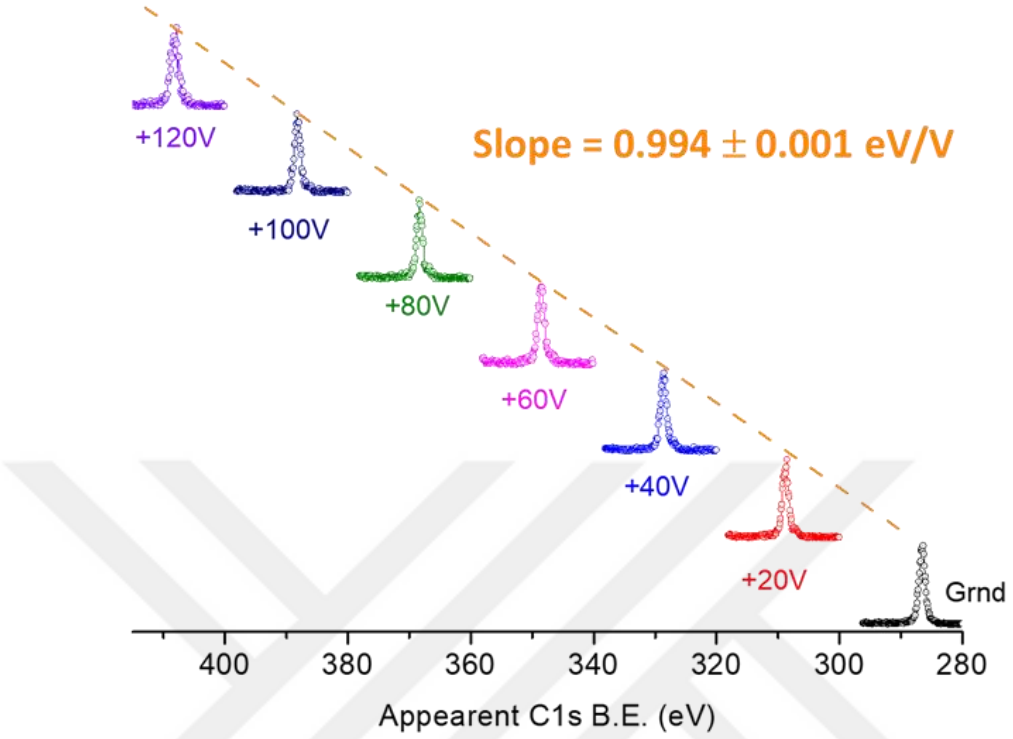

Figure 29 C1s region on the drop, recorded at different bias applied to the liquid until potential where the dielectric breakdown occurs. **(***Reprinted with permission from Aydogan Gokturk, P., Ulgut, B. and Suzer, S. "DC Electrowetting of Nonaqueous Liquid Revisited by XPS". Langmuir 2018, 34, 7301-7308. Copyright 2018, American Chemical Society.)*

After a certain potential (120V in this case) the binding energy deviates from the linearity due to the dielectric breakdown. Hence, drop peaks experience a potential development close to the magnitude of applied potential but with only small deviations, which then recover itself within seconds, see Figure 30. This 120V can be assigned as a dielectric breakdown voltage for the device under investigation and even after the breakdown, which leads to passage of current, vacuum conditions are not altered.

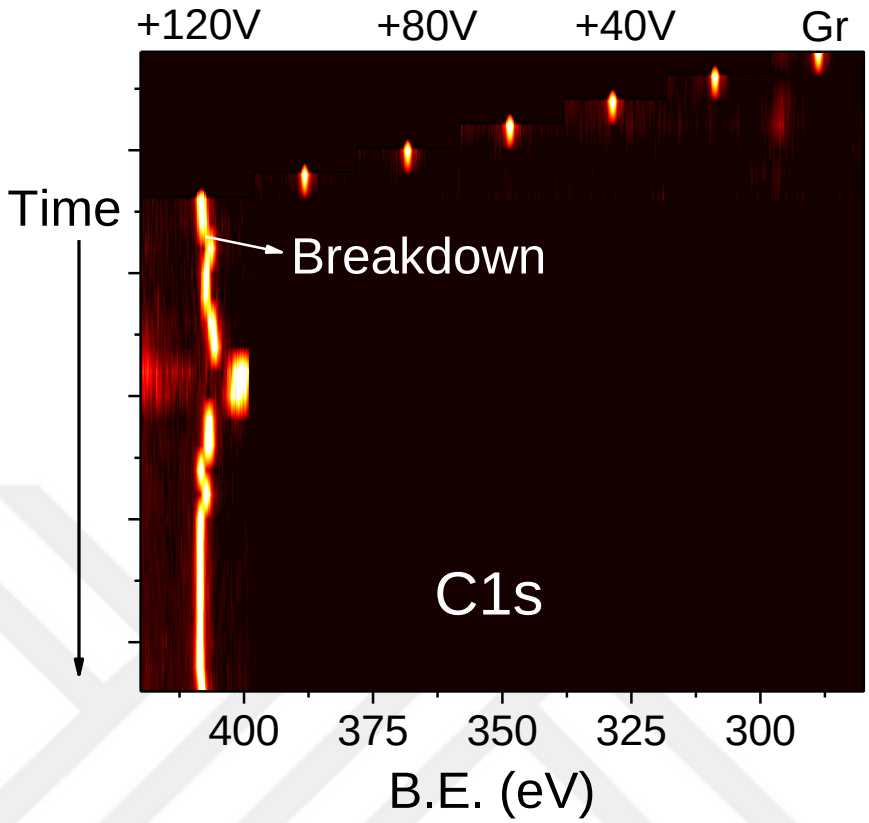

Figure 30 C1s spectra recorded at +20V increments until the onset of the breakdown at +120V, and afterwards at ~1 minute intervals, but still under +120V. Note that the drop recovers and returns to the full applied bias within minutes. *(Reprinted with permission from Aydogan Gokturk, P., Ulgut, B. and Suzer, S. "DC Electrowetting of Nonaqueous Liquid Revisited by XPS". Langmuir 2018, 34, 7301-7308. Copyright 2018, American Chemical Society.)*

The dielectric breakdown is an important phenomenon limiting the applicability of the EW process. Therefore, chemically specific information derivable using our approach can provide a completely fresh investigation perspective. Recorded current measurements are given in Figure 31 and show the rapid increase of leakage current to microampere range after 120V when the dielectric breakdown occurs.

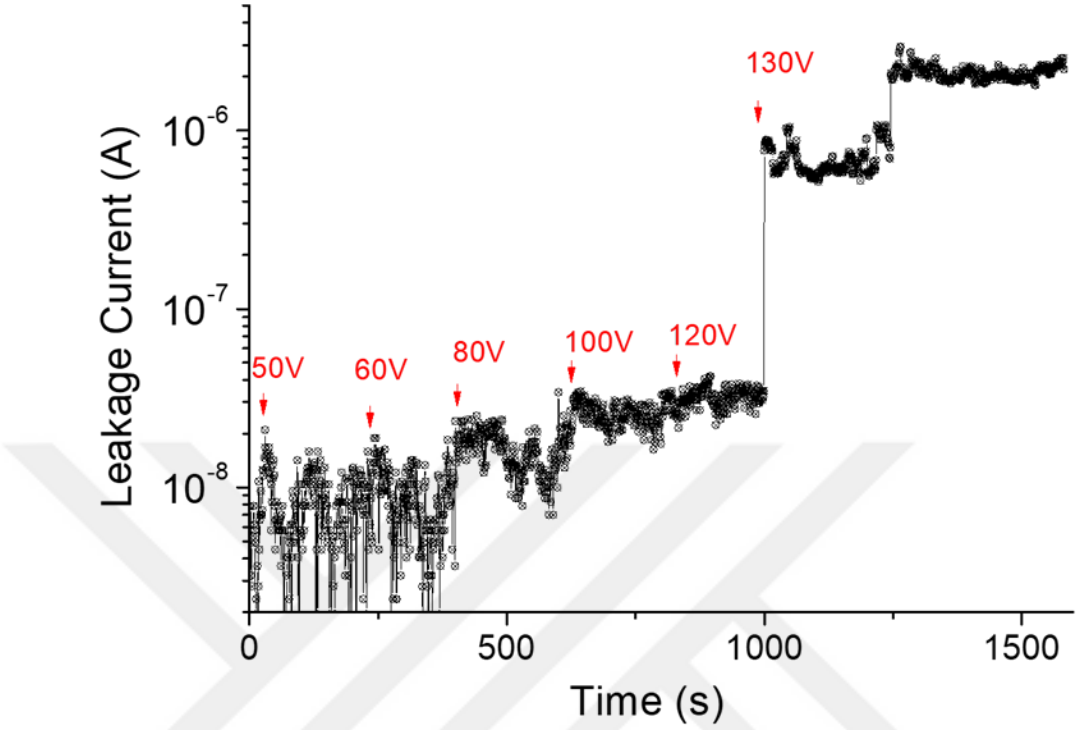

Figure 31 Current measurements through a liquid (PEG) drop during an XPS investigation, under various biases approaching the breakdown and beyond. *(Reprinted with permission from Aydogan Gokturk, P., Ulgut, B. and Suzer, S. "DC Electrowetting of Nonaqueous Liquid Revisited by XPS". Langmuir 2018, 34, 7301-7308. Copyright 2018, American Chemical Society.)*

The combined dielectric breakdown voltage for the ~50 nm hydrophobic CYTOP layer and the 300 nm silicon oxide layer can be estimated as **126 V**, using the following formula and constants adopted from Reference [142].

$$\boldsymbol{V_{d.b.}} = \boldsymbol{E_{d.s}} \times \mathbf{t}$$

where $\boldsymbol{E_{d.s}}$ is the dielectric strength and $\mathbf{t}$ is the thickness.

$$V_{d.b.}(CYTOP) = 0.11\frac{V}{nm} \times 50nm = 5.5V$$,

$$V_{d.b.}(SiO_2) = 0.4\frac{V}{nm} \times 300nm = 120V$$

$$V_{d,b}(device) = 126V$$

Dielectric breakdown was also observed in air ambient by following a similar procedure of XPS analysis. For that, the same device configuration was used and the bias was applied between the wire electrode and the bottom of the silicon while silicon end is connected to the ground of the source meter. Applied bias was increased with +10V increments from 0V to +210V and a video was recorded. In the video and up to +50V, the contact angle changes and spreading of the drop is clearly observable. After that, the contact angle does not change much due to contact angle saturation phenomenon and a hard dielectric breakdown occurs around +120V. With the further increase in the amplitude of the bias, bubble-like features and drastic disruptions in the drop become visible. See Figure 32, which represents some of the snapshot images of the video recording in various magnitudes of potentials before and after the dielectric breakdown.

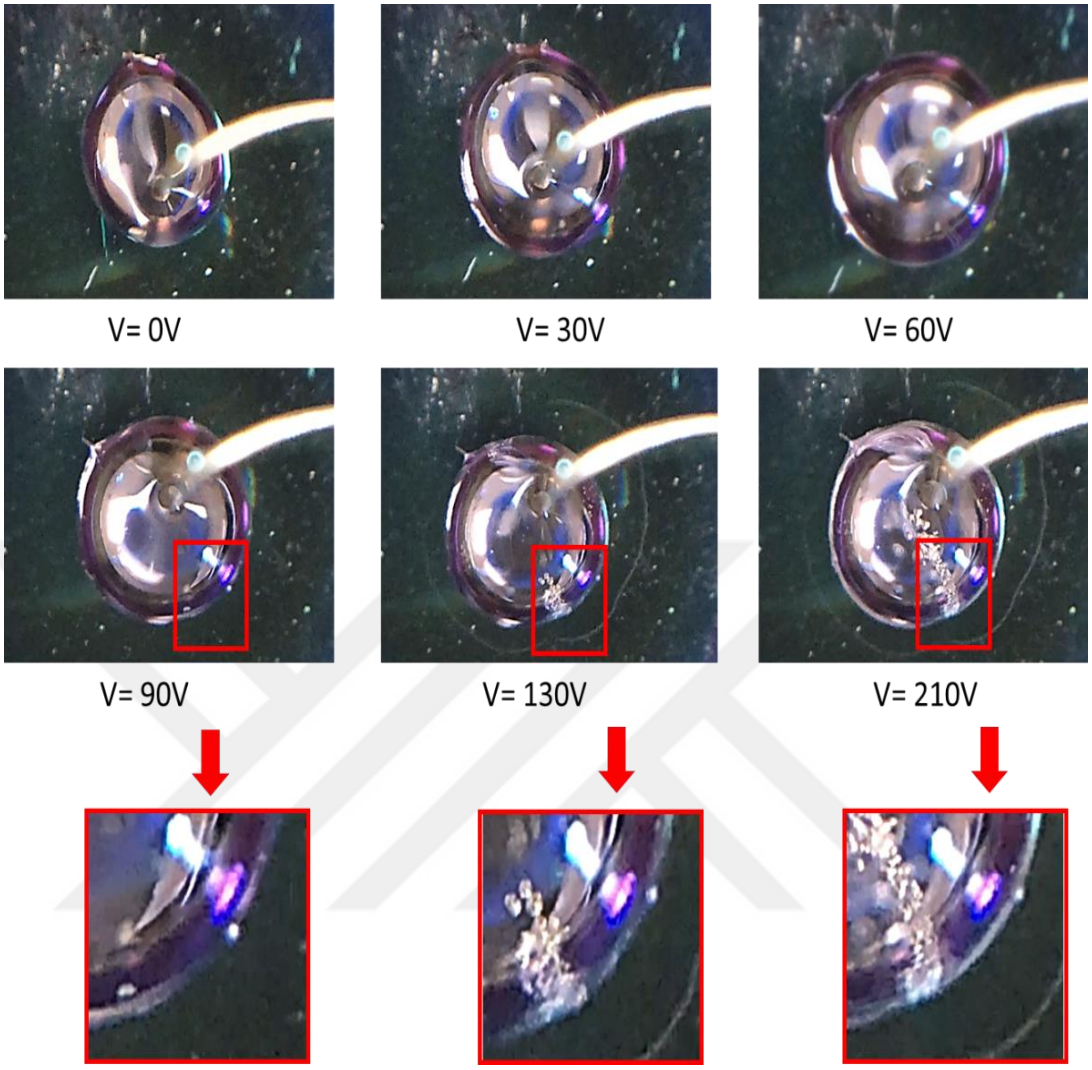

Figure 32 Snapshot images from the video recording of top-gated PEG EWOD device in air ambient with the application of different amplitude of potentials before and after the dielectric breakdown. *(Reprinted with permission from Aydogan Gokturk, P., Ulgut, B. and Suzer, S. "DC Electrowetting of Nonaqueous Liquid Revisited by XPS". Langmuir 2018, 34, 7301-7308. Copyright 2018, American Chemical Society.)*

3.5. Potential Developments Under AC Excitation

This part is "reproduced with permission from Langmuir submitted for publication. Unpublished work copyright 2018 American Chemical Society."

As was mentioned in the previous section, with the DC electrowetting, though no potential drop is observable at the top wire electrode/liquid interface, the entire potential drop develops across the liquid/substrate interface with dynamics faster than our probe time which is the order of 100 ms, up to large biases around 120V leading to the dielectric breakdown. It was also demonstrated that the intrinsic properties of the liquid as well as the conductivity do not play any role in the potential development with DC bias, since we did not observe any change in the electrical behavior for IL nor PEG devices.

In order to see the frequency dependent behavior of the potential developments, we performed similar line scan analysis as in Figure 24 to the EWOD device of IL and PEG while we were applying an alternating electrical signal in the form of square wave with the same amplitude but variable constant frequencies. Figure 33, shows the recorded line scan results of F1 at different $\pm$6V AC squarewave frequencies, along the line beginning from the substrate towards to the middle of the IL drop. Similar to the previous observations, there are two F1s peaks observable in this region. One of them is a broad peak in the higher binding energies coming from the commercial CYTOP fluoropolymer due to its charging nature. Other one is narrow F1s peak coming from the DEME-TFSI. According to the figure, observations for the AC IL electrowetting on dielectric are very similar to

what we had observed on the DC case. Accordingly, when we applied the potential from the bottom of the silicon substrate, an independent of the frequency, the second peak coming from the substrate shifts to reflect the positive and the negative components of the applied square wave. The peak coming from the IL maintains its ground state position even in the interface region. Hence, again the entire potential drops in the substrate/ IL interface. Additionally, due to the charging nature of CYTOP film, the broad F1s peaks shows shift towards the higher binding energy during the data acquisition. Nevertheless, it is important to point out that the difference between the positive and negative component is always equal to 12 eV, which is the amplitude of peak to peak potential for the applied SQW. Figure 33, also shows the movement of the drop and possible expansion and contraction because the location of interface changes slightly with various frequencies.

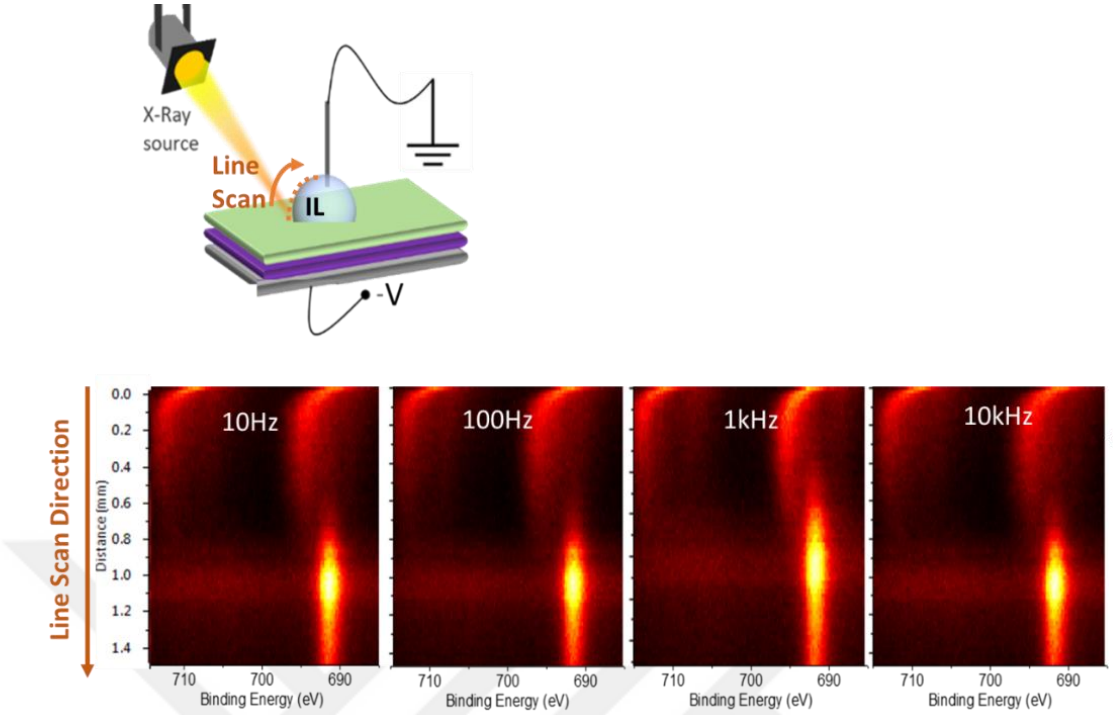

Figure 33 F1s spectra recorded at different AC SQW frequencies, along the line beginning from the substrate towards to the middle of the drop.

On the other hand, Figure 34 shows the recorded line scan results of O1s for PEG EWOD device at different AC frequencies. Contrary to the IL, PEG exhibits a strong frequency dependent potential development under the operating conditions. At very low frequencies PEG shows the similar characteristics with DC excitation. However, with increasing frequency, amplitude of the potential on the PEG drop increases and begins to reflect the positive and the negative components of the SQW potential bias. The peak difference between the positive and the negative components of O1s peak increases in higher frequencies and reaches to the amplitude of 12 eV.

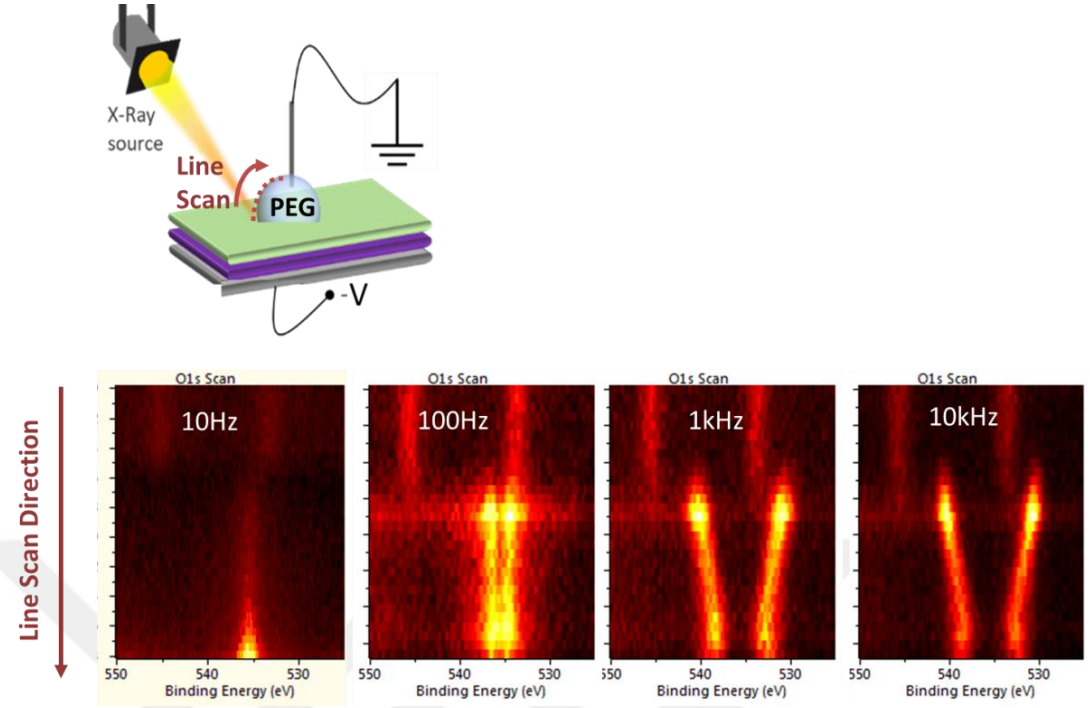

Figure 34 O1s spectra recorded at different AC SQW frequencies, along the line beginning from the substrate towards to the middle of the drop

In order to better follow this frequency dependent behavior of potential on the droplet in AC electrowetting process, we have used a device in the experimental set-up, which is depicted in Figure 35. In this set-up, contrary to previous measurement, we did no set the frequency at constant value but we applied a time-varying SQW electrical signal with a logarithmic frequency sweep, starting from 100 mHz and reaching 100 kHz with an amplitude of 6 V, either from the bottom of the planar electrode, (Figure 35a,c) or the top of the liquid drop (Figure 35b,d). We then followed the surface potential by recording the O1s signal and F1s signal from a single point on the drops for PEG and IL respectively repetitively. For this kind of time-resolved XPS analysis y-axis represents the number of scans or iterations while

the x-axis is the binding energy. Each iteration row is formed from a single spectrum on the same position. However, appearance of the spectrum changes due to the changes (like frequency) in the external excitation. Transformation of iteration axis to the relevant frequency one is also shown in Figure 36.

When actuated from the bottom electrode, the PEG, a dielectric liquid, adopts the ground potential of the inserted wire electrode at very low frequencies up to ∼70 Hz, and only one O1s peak is measurable. After 70 Hz two O1s peaks are measured, reflecting the positive and the negative components of the SQW potential bias. The difference in the binding energy positions of these two peaks increases continuously and reaches a steady state value at ∼800 Hz, which is maintained at higher frequencies. However, this steady-state potential is not equal to the entire of applied potential but a fraction of it. The continuous nature of the transition from capacitative to resistive behavior as a function of frequency is illustrated in Figure 35a, when the bias is applied from the bottom electrode. Accordingly, we can define the frequencies up to 70 Hz and above 800 Hz regions as the low and high frequency regimes, respectively.

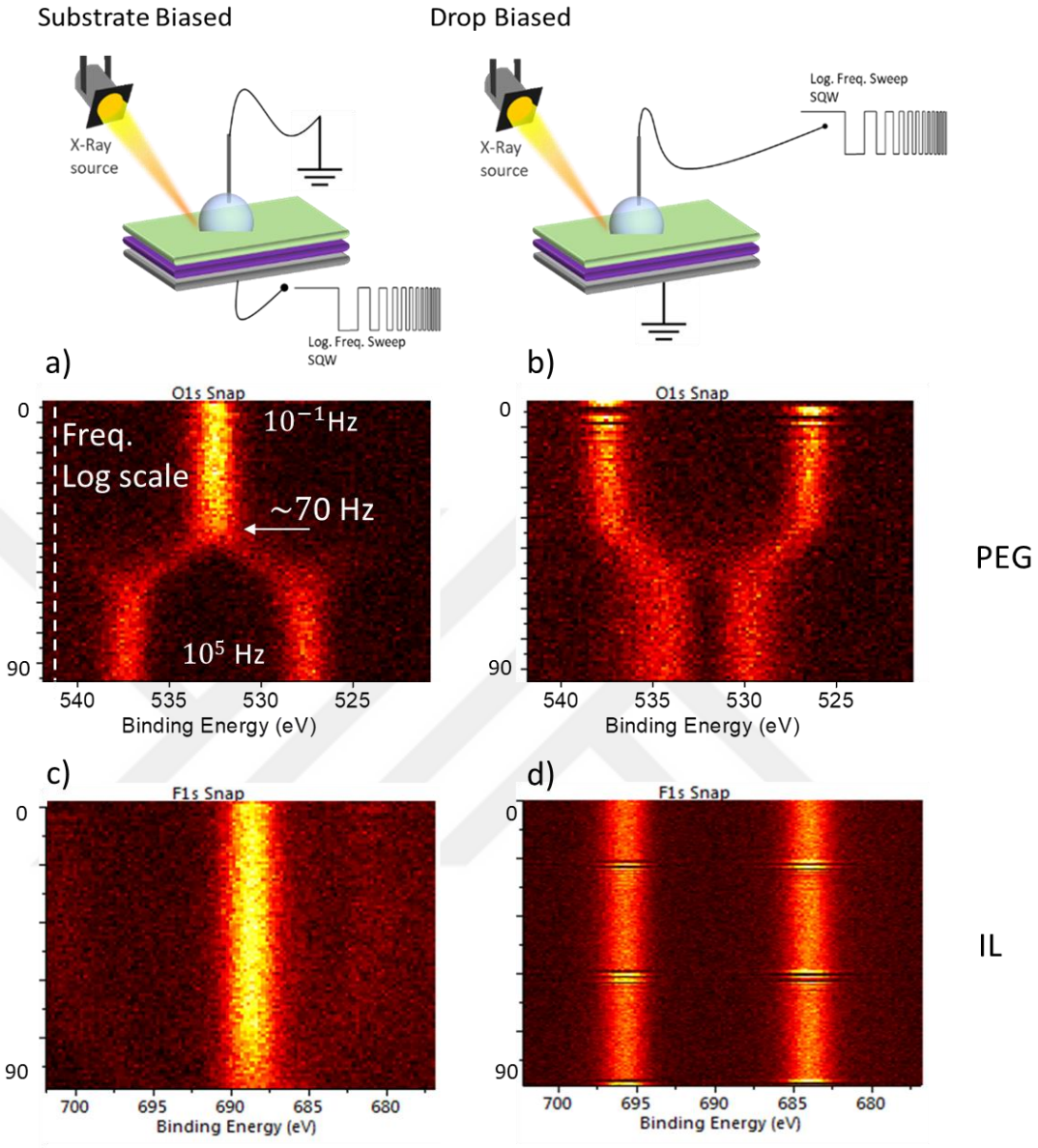

Figure 35 Schematic representation of the AC actuation by imposing the bias from; (a)(c) the bottom or (b)(d) the top electrodes, together with the recorded O1s and F1s spectra for PEG and IL devices respectively while sweeping the frequency**.**

In the reverse geometry, where the bias is applied through the droplet, while the bottom electrode is grounded, the frequency dependence exhibits a mirrored behavior, as seen in Figure 35b. The measured non-varying onset of 70 Hz

on the entire surface of the droplet can be associated with the critical frequency for the pristine PEG having ~600 Da molecular weight. The corresponding value for the de-ionized water has been reported and also predicted by numerous calculations to be in the order of a few kHz, and increases further by incorporation of ionic components.[114]

On the other hand, for a conductive ionic liquid droplet, ions can follow up the applied bias from the wire for all test frequencies up to 100 kHz, see Figure 35c-d. These findings are predicted and consistent with previous studies because the critical frequency for this conductive media was reported previously to be around 500 kHz which exceeds our 100 kHz limit.[133] Hence, the all data for IL that we gathered corresponds to the low-frequency regime behavior for IL device.

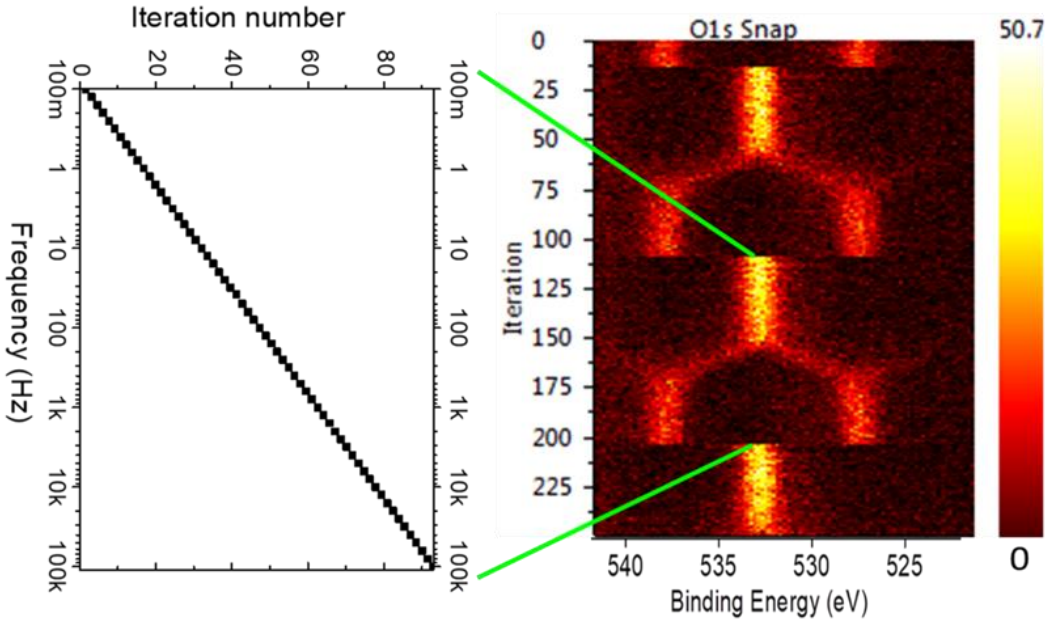

Figure 36 Time dependent iterative spectra of O1s region as a 2D intensity and frequency plot with respect to the iteration number.

In the literature, critical frequency is measured under the AC excitation in the sinusial waveform. Even though the XPS line shape under sine and square wave excitations are considerably different with respect to their line-shapes as we mentioned in the introduction part, the measured critical frequency for our EWOD device in investigation does not differ. Figure 37 shows the time dependent O1s peaks under the sinewave and squarewave excitations, while sweeping the frequency from 100 mHz to 100 kHz. As is also understood from the figure, the critical frequency between these two behaviors is same in both waveforms of AC excitation.

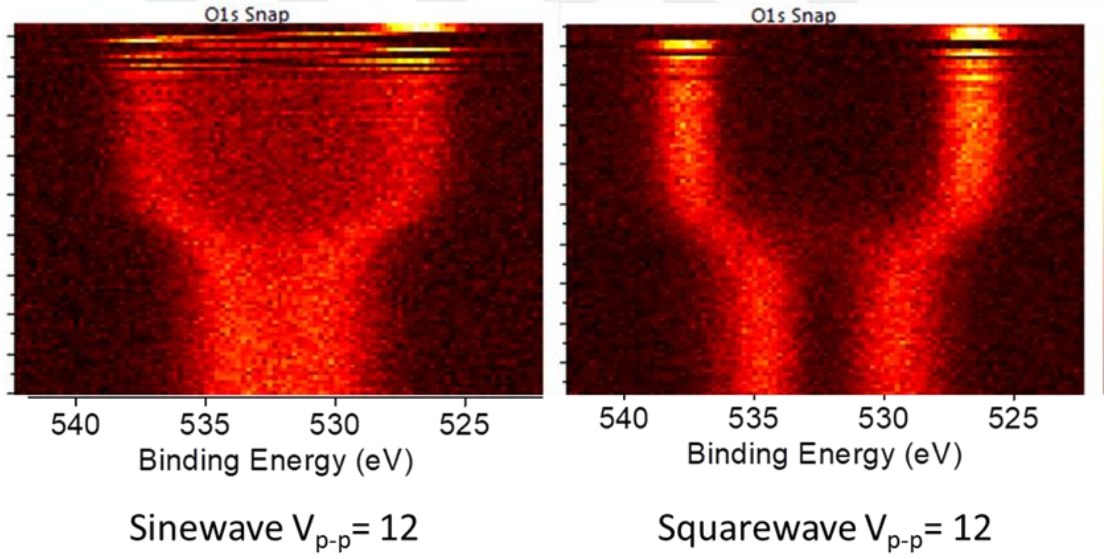

Figure 37 Time dependent iterative spectra of O1s region as a 2D intensity and frequency plot with respect to the iteration number.

The measured steady-state potential at high frequencies, on the other hand, is a fraction of the bias and its magnitude differs significantly depending on the position of the point on the droplet surface, as depicted in Figure 38. We, therefore advocate that the critical frequency, as probed by XPS under the SQW modulation, is an intrinsic property of the liquid, and is the same for all points analyzed on the entire drop; i.e. does not change with the position. However, steady-state potential at higher frequencies depends strongly on position, and adapts to a fraction of the applied potential, as a function of the distance of the analyzed point from the wire-electrode, as depicted in Figure 38 a and b, which show iterative O1s signals recorded at three different positions on the drop, upon the AC excitation from the bottom of the planar electrode or the top of the counter wire electrode, respectively.

As can be seen from the Figure 38, while the critical frequency stays constant, the amplitude of potential measured varies with the distance from electrodes in higher frequencies. Thus, on the point close to the liquid/dielectric interface, negative and positive components of the O1s peak show the potential on the dielectric which merge to each other (near zero IR drop) if the substrate is grounded or shows no measurable IR drop (full 12V) if the bias is applied from the substrate and vice versa for the liquid/ wire electrode interface.

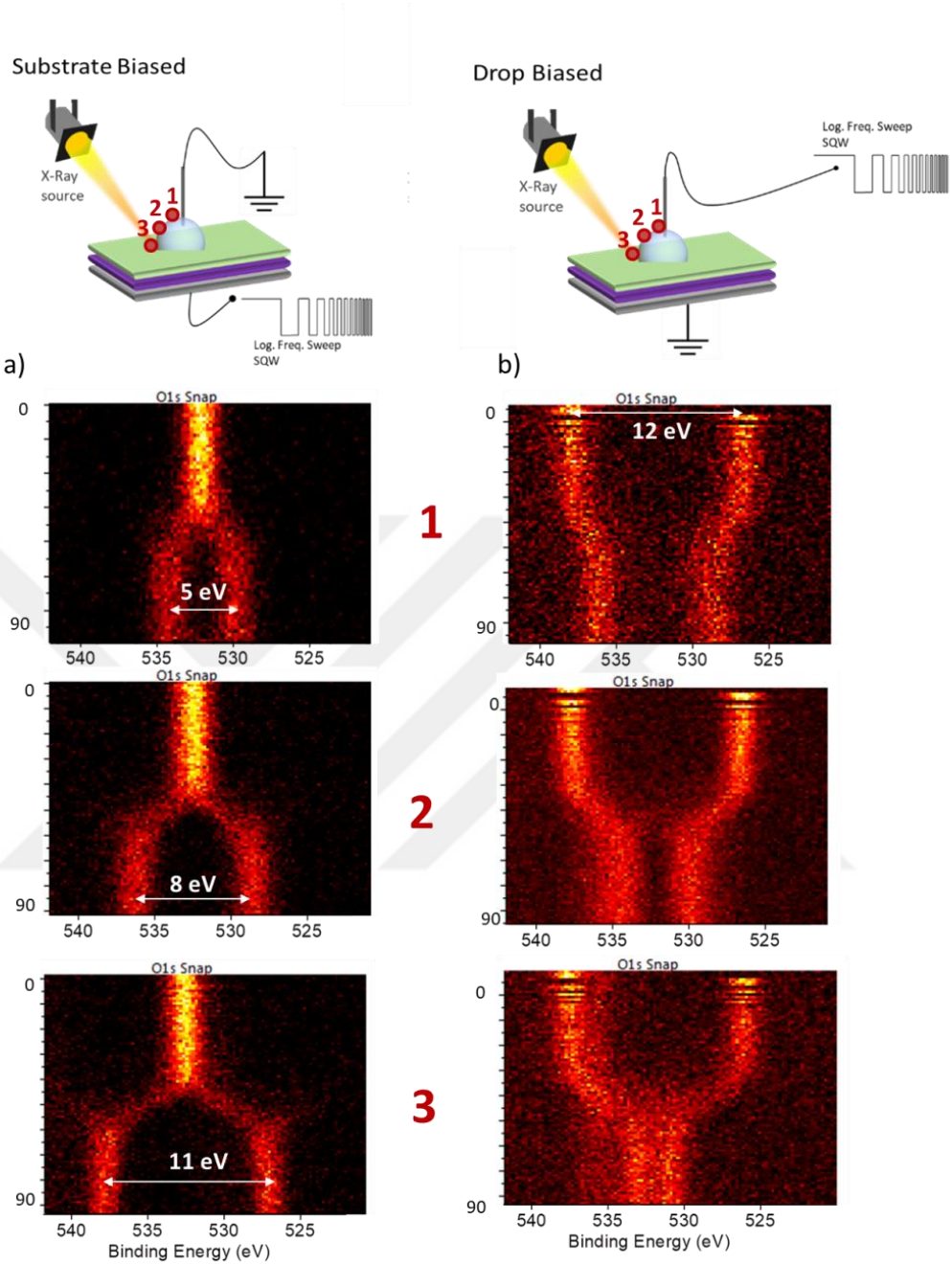

Figure 38 O1s spectra recorded under continuous AC actuation at three different positions on the drop, while imposing the bias from; (a) the top or (b) the bottom electrodes.

To extend these measurements to the entire liquid surface, we have recorded the O1s signal in the areal mapping mode and at only two frequencies representative of the lower and the higher frequency regimes, since collecting

continuous frequency data is not feasible. At first, with the simple EWOD configuration external bias in the form of SQW with a fixed frequency was applied from the bottom planar electrode while the wire was grounded. Then, we collected O1s (coming from PEG) peaks from the region between 520-545 eV in the fast snap-shot mode of the instrument with 50 µm x-ray spot size and 50 µm steps from the selected area which contains the entire liquid surface.

In order to quantify the potential distribution on the droplet surface, the entire set of the collected spectra are fitted to two different O1s peaks as a negative and a positive components, using the Avantage software. In order to do that, we only considered the peaks coming from the droplet shape and ignored the other O1s contributions coming from the substrate by simply eliminating them through their low peak intensity. The difference in the binding energy positions between the two components of PEG peaks are assigned to the developed AC potential at that position. These values are converted to a 3 dimensional areal matrix consisting of x and y coordinates with 50 µm steps and corresponding data for the each of x and y values. Finally this matrix is converted into a color filled contour plot as shown in Figure 39 which are areal maps for the lower (50 Hz) and higher (1 kHz) frequencies separately. The color bar represents the amplitude of the splitting measured.

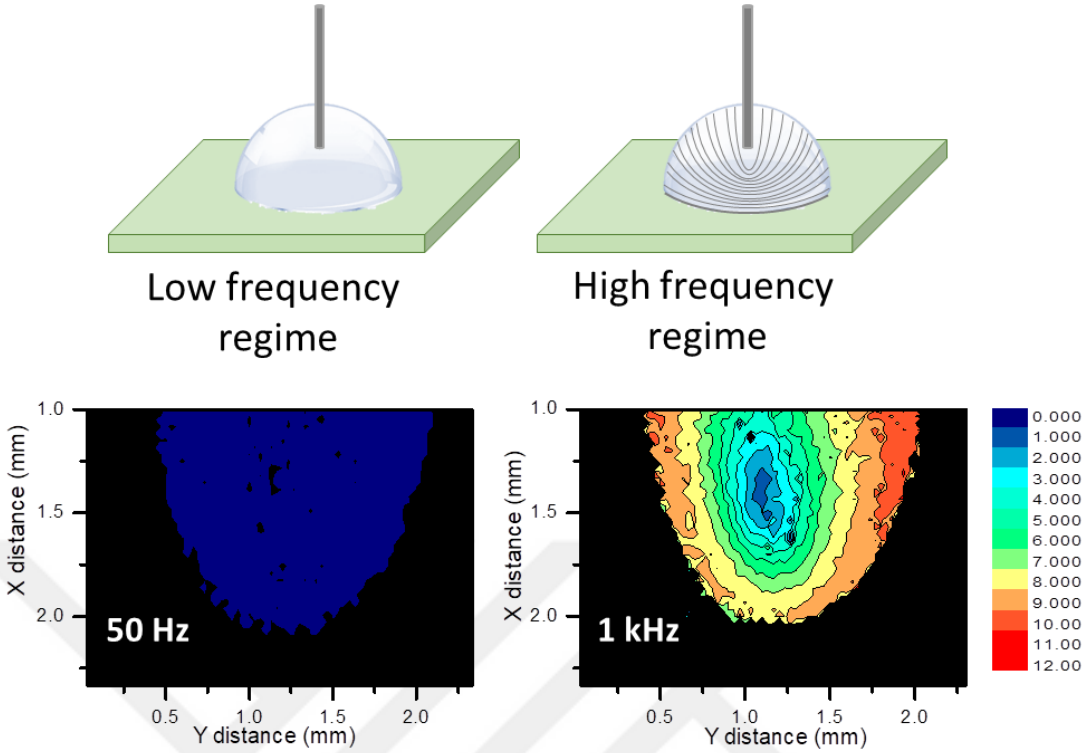

Figure 39 Areal maps of the binding energy difference of positive and negative components of O1s under the applied 6V square wave bias from the bottom electrode with; (a) 50 Hz, and; (b) 1 kHz frequencies together with their schematic representations.

For the low frequency SQW application (50 Hz), only one O1s peak appeared around 533 eV. However, for the high frequency SQW, either the merged single peak or a twinned two peaks appear depending on the position of the analyzed point. For the points, which are close to grounded wire, still only one O1s peak is observed as depicted in Figure 40. However, for points that are away from the ground electrode, the O1s peak is split into one negative and one positive components. The energy difference between the twinned peaks varies, between 0 and 12 eV, as a function of the position between the two electrodes. An intermediate splitting is shown in the Figure 40.

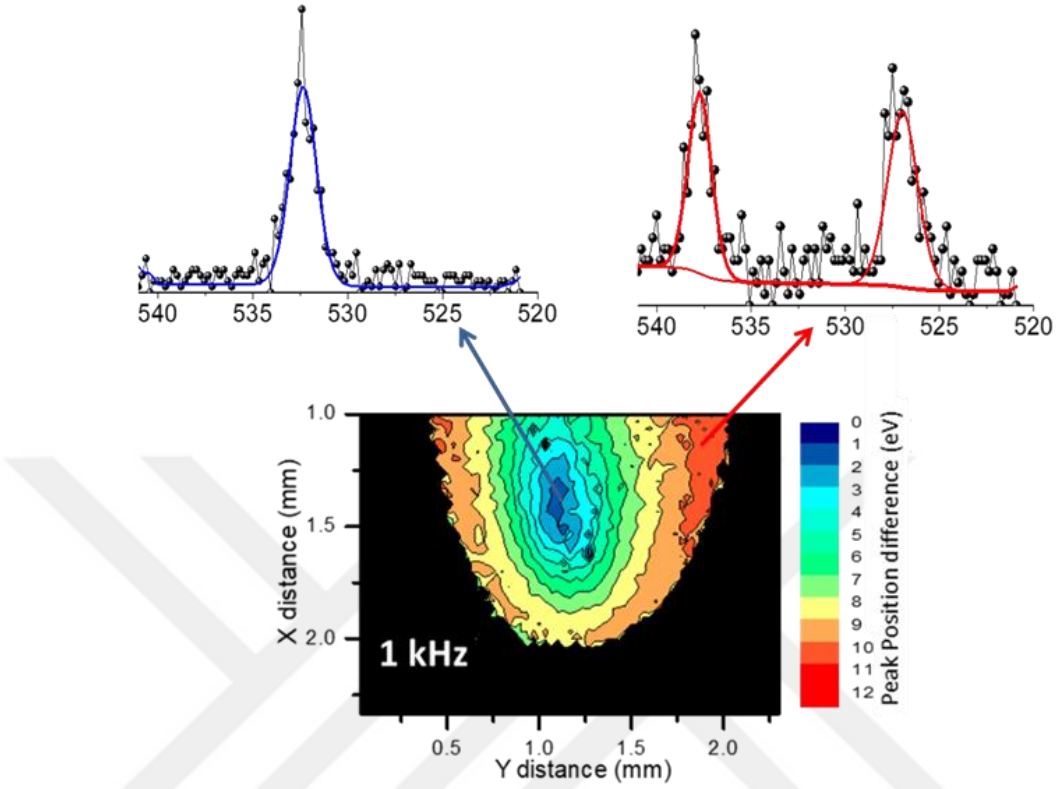

Figure 40 Areal maps of the binding energy difference of positive and negative components of O1s under the applied 6V square wave bias from the bottom electrode with 1 kHz frequencies together with illustrative O1s spectra coming from two different positions.

As is evident at 50 Hz (in the low frequency region and before the critical frequency), the liquid completely screens the applied electrical field and the entire potential drop takes place at the liquid/dielectric interface as in the case of DC electrowetting. As a result only one O1s peak is observed throughout the droplet surface. However, at 1 kHz, the liquid can no longer screen the field, and the drop behaves like a resistive medium, resulting in splitting of the O1s peaks. The magnitude of the splitting is near zero at the tip of the wire electrode and increases

to up to 12 eV at the liquid/dielectric interface. This behavior is evidenced by the equipotential surface contours in Figure 39.

The relevant critical frequency in electrowetting depends on the intrinsic properties of the liquid and changes with the conductivity of the liquid used in electrowetting and increases with increasing ionicity. In the previous measurements, we analyzed the two extreme cases where we have liquids that one of them is fully ionic and the other is non-ionic. In addition, we have carried out the same type of measurement with Figure 35 while we are imposing AC electrical potential in the form of SQW with the sweeping frequency again from the 100 mHz to 100 kHz to a liquid where $MgCl_2$ was added to PEG as illustrated in Figure 41. As expressed in the equation 2, the relevant critical frequency in electrowetting stems out as an intrinsic property of the liquid and is expected to change with the conductivity of the liquid, as was observed for the aqueous ionic solutions.[114] In order to confirm this prediction, we now show that the addition of salt ions into the PEG media shifts the critical frequency.

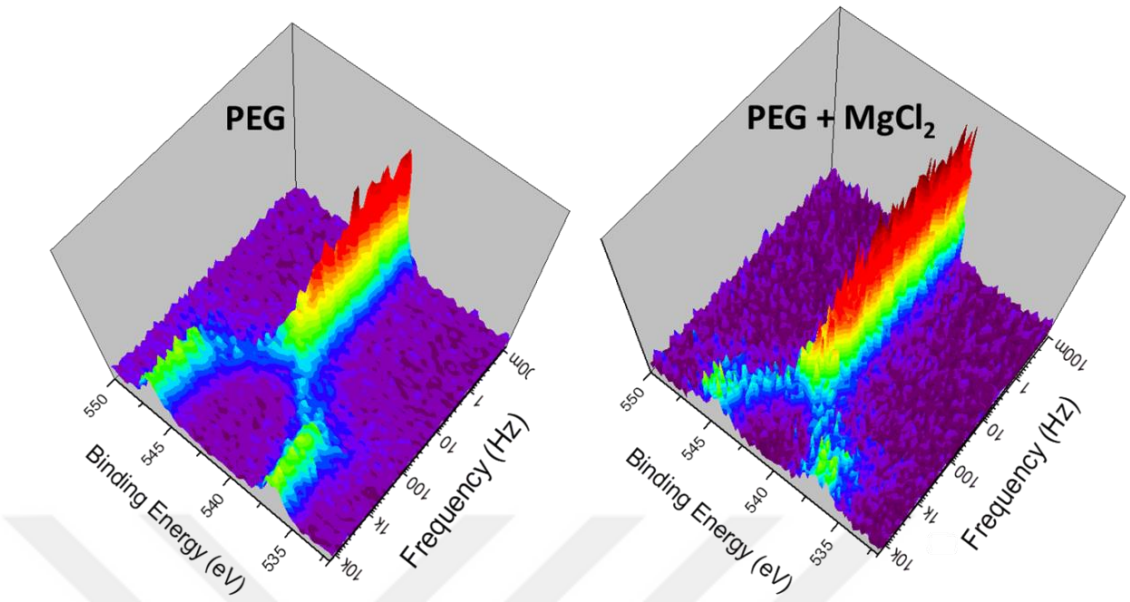

Figure 41 O1s spectra recorded under continuous AC actuation (10^{-1} to 10^{4} Hz) for three different liquid drops.

Addition of ionic moieties into the PEG media shifts the critical frequency from 70 Hz to 700 Hz. This finding can be rationalized by noting that the viscous liquid, with its low molecular weight polymeric nature has limited and very sluggish and connected dipoles, which can only screen the applied electrical field at low frequencies. Once, the pulses become faster the current starts flowing through the liquid. Addition of ions, with higher but again with limited mobility in the viscous liquid, introduces ionic screening in addition to the dipolar one, which extends the frequency range of screening by no more than a factor of five.

3.6. Model Electrical Circuits Mimicking The EWOD Devices

This part is "reproduced with permission from Langmuir submitted for publication. Unpublished work copyright 2018 American Chemical Society."

In light of the above findings and also the additional measurements we had carried out using a mimicking device to be described below and in order to describe the EWOD system under investigation electrically, a circuit model was constructed as shown in Scheme 1. In this circuit, the PEG droplet is represented as a capacitor (C_{liquid}) in a parallel connection with resistor (R_{liquid}). The two-layer dielectric stack of CYTOP and SiO_2 is also represented by a very large leakage resistor ($R_{leakage}$) and a parallel capacitor ($C_{dielectric}$). The droplet impedance depends on the dipolar strength and changes with the addition of salt. Note that, although an infinite number of series resistors should have been used to represent the liquid drop, only four are used for practical purposes. In addition, we, like many studies using the equivalent electrical circuits for EWOD, did not consider the electrical double layers on interfaces, since the double layer thicknesses are much smaller than that of the dielectric. As a result, the dielectric capacitance dominates, which has been proven by many other groups and the error stemming from ignoring the double layers, for a planar dielectric/liquid interface, is in the order of 0.01%.[95,108,114,115]

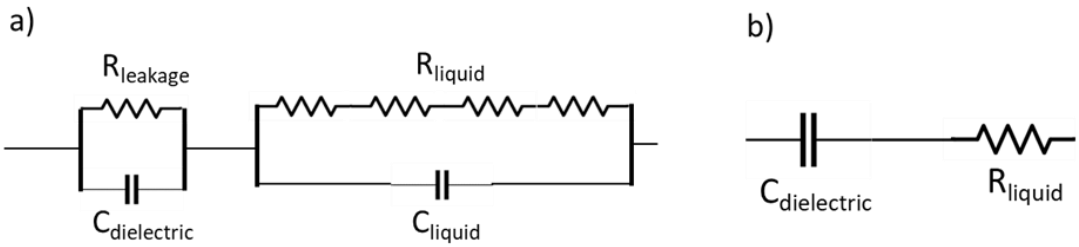

Scheme 1 a) Equivalent circuit model for the EWOD system under investigation and b) Simplified equivalent circuit model

Total capacitance of dielectric stack can be estimated by considering them as two series parallel plate capacitors where:

$$C = \frac{A.\epsilon_0.\varepsilon_d}{d} \text{ and } \frac{1}{C_{total}} = \frac{1}{C_{CYTOP}} + \frac{1}{C_{SiO2}}$$

The layer thickness (d) for CYTOP is measured by a profilometer and found to be around 50 nm and for SiO_2 thickness is 300 nm.

$$C_{CYTOP} = \frac{A.\epsilon_0.\varepsilon_d}{d} = \frac{8.854 \times 10^{-12}\, F/m \times\ 2 \times \pi \times (1\ mm)^2}{50 * 10^{-9} m} = 1112 \text{ pF}$$

$$C_{SiO2} = \frac{A.\epsilon_0.\varepsilon_d}{d} = \frac{8.854 \times 10^{-12}\, F/m \times\ 4 \times \pi \times (1\ mm)^2}{300 * 10^{-9} m} = 370 \text{ pF}$$

$$\frac{1}{C_{total}} = \frac{1}{C_{CYTOP}} + \frac{1}{C_{SiO2}} = \frac{1}{pF} + \frac{1}{pF}$$

$$C_{total} \cong 270 \text{ pF}$$

Thus, we estimated the capacitance of the dielectric layer, hence that of the system, as ~270 pF, using the geometry of the drop and the dielectric parameters of the media.

Using this value and the measured critical frequency through XPS as 70 Hz and the simplified equivalent circuit consisting of a series R_{liquid} and $C_{dielectric}$, shown in Scheme 1b, the total effective AC resistance (impedance) of the drop can now be estimated around 8 MOhm using the formula below:

$$f = \frac{1}{2\pi R_{liquid} C_{dielectric}}$$

In order to further check the reliability of the derived circuit that represents the electrical behavior of our EWOD devices, and to find out the other missing parameters ($R_{leakage}$ and C_{liquid}) we also employed Electrical Impedance Spectroscopy for the same PEG EWOD device but in air ambient. Details of the experimental procedure were given in the experimental section. Representative experimental impedance spectrum is shown in Figure 42 for the electrowetting of PEG with 0.5V alternating voltage. Impedance modulus versus frequency curve shows two characteristic behaviors in the low frequencies and high frequencies. Figure 42 also shows the fitting results of estimated electrical circuit given in Scheme 2.

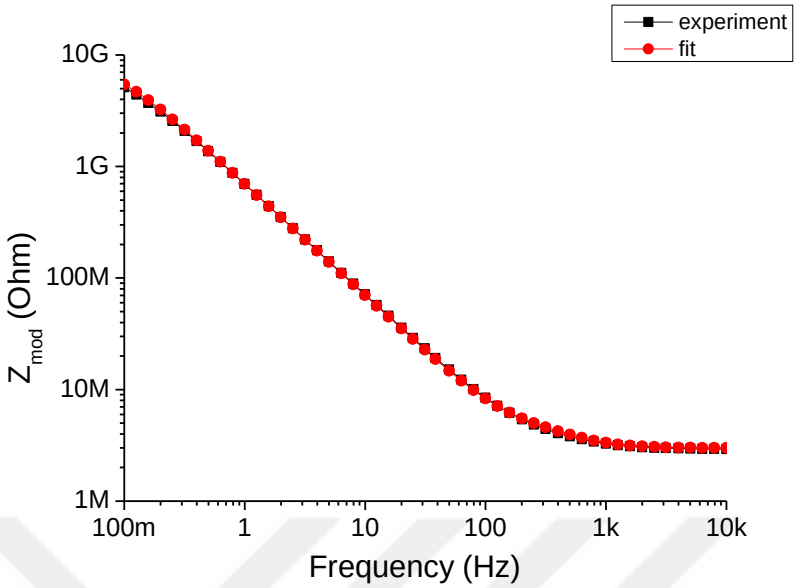

Figure 42 Impedance modulus versus frequency for the PEG electrowetting at 0.5 V AC voltage

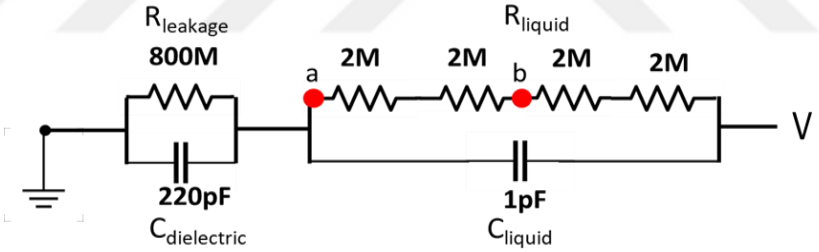

Scheme 2 Schematic representation of solid-state mimicking device developed from the EIS and computational results

In the next step, we used LT-Spice simulation software and generated the output waveforms from two different points (a and b), shown in the Scheme 2, of the equivalent circuit using various frequencies between 10 Hz-10 kHz AC square waves as the input. After that, we used these waveforms to generate the XPS data from the ground state spectrum of the respective element by using an in-house

developed Phyton program to compare with the experimental results. Figure 43 illustrates the generated waveforms from the position b at three different frequencies namely 10 Hz, 100 Hz and 1k Hz as an example together with the representative XP spectra.

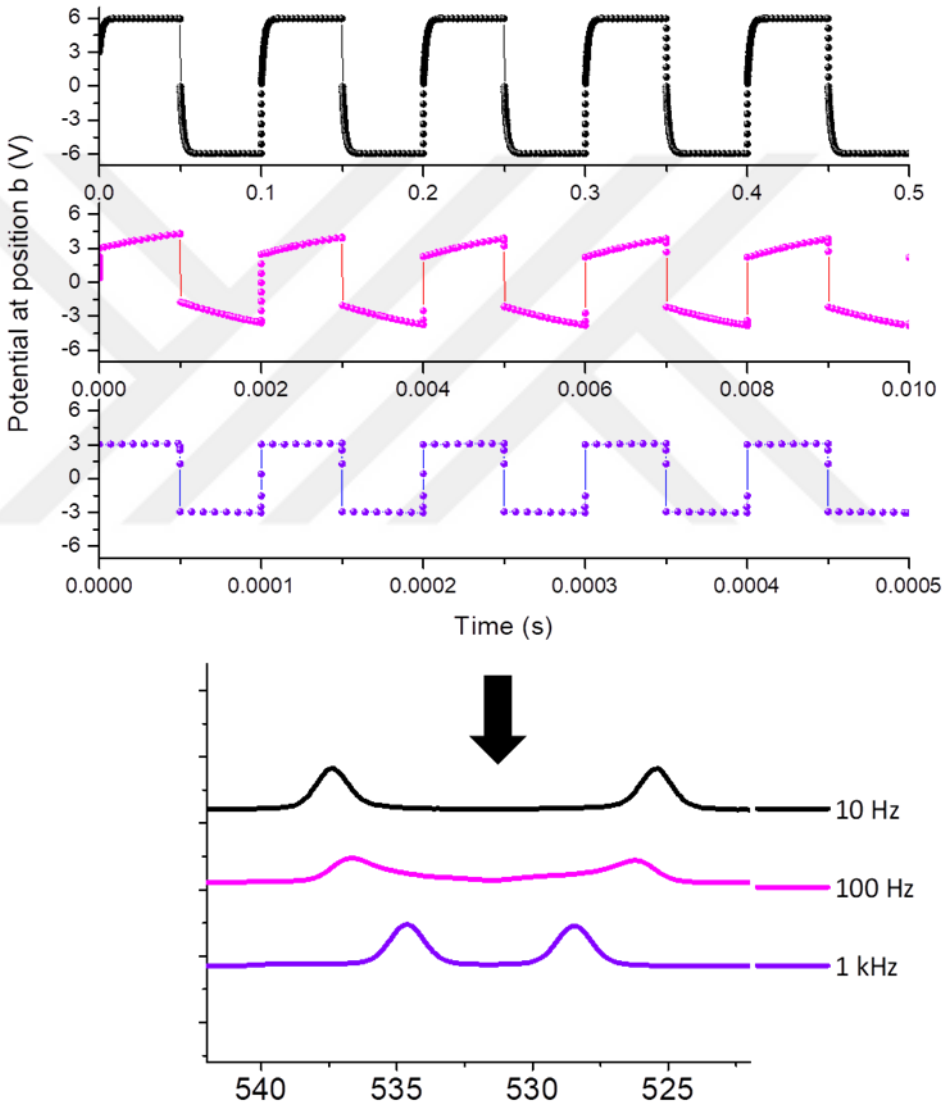

Figure 43 Output waveforms generated from the b position on the proposed circuit at three different frequencies and corresponding simulated O1s spectra from each of them

Figure 44 shows the simulated XPS spectra at two different points (a and b) along the drop and at several relevant frequencies. In the same figure, the corresponding measured spectra are also reproduced c and d, which were already given in Figure 38. Resemblance of the simulated data to those of the measured ones is simply remarkable.

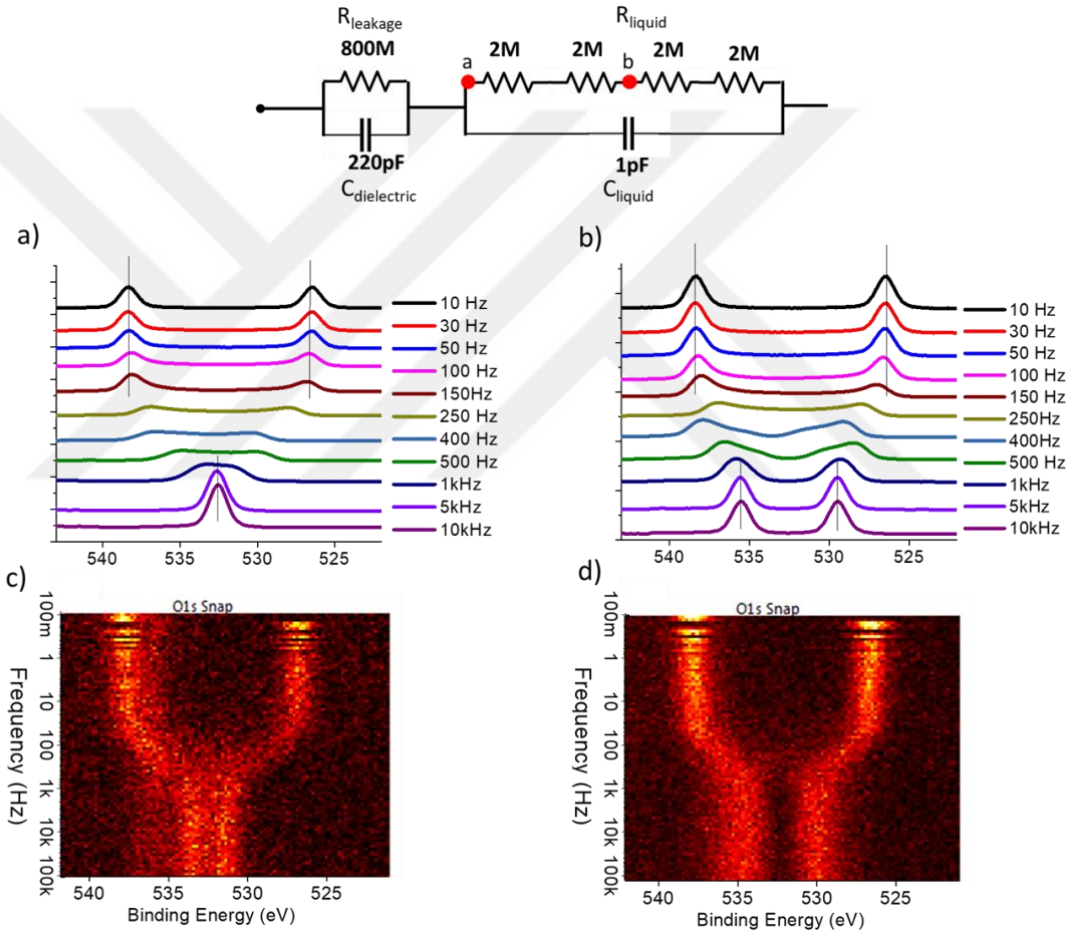

Figure 44 (a) and (b). Simulated O1s spectra at two different positions on the equivalent circuit used, while (c) and (d) are the recorded ones, on the liquid surface at two different points.

In order to further verify the simulation results, we have carried out AC XPS measurements on a mimicking device made out of only solid state resistors and capacitors connected together by soldering. Sn3d peak at the soldering connections are used to record the data at four different points, representative of the different points along the liquid drop as was given in Figure 38. The data are displayed in Figure 45. Examining the spectra displayed in these two figures lead us to boldly postulate that the device faithfully mimics the electrical and frequency dependent behavior of the liquid PEG EWOD device.

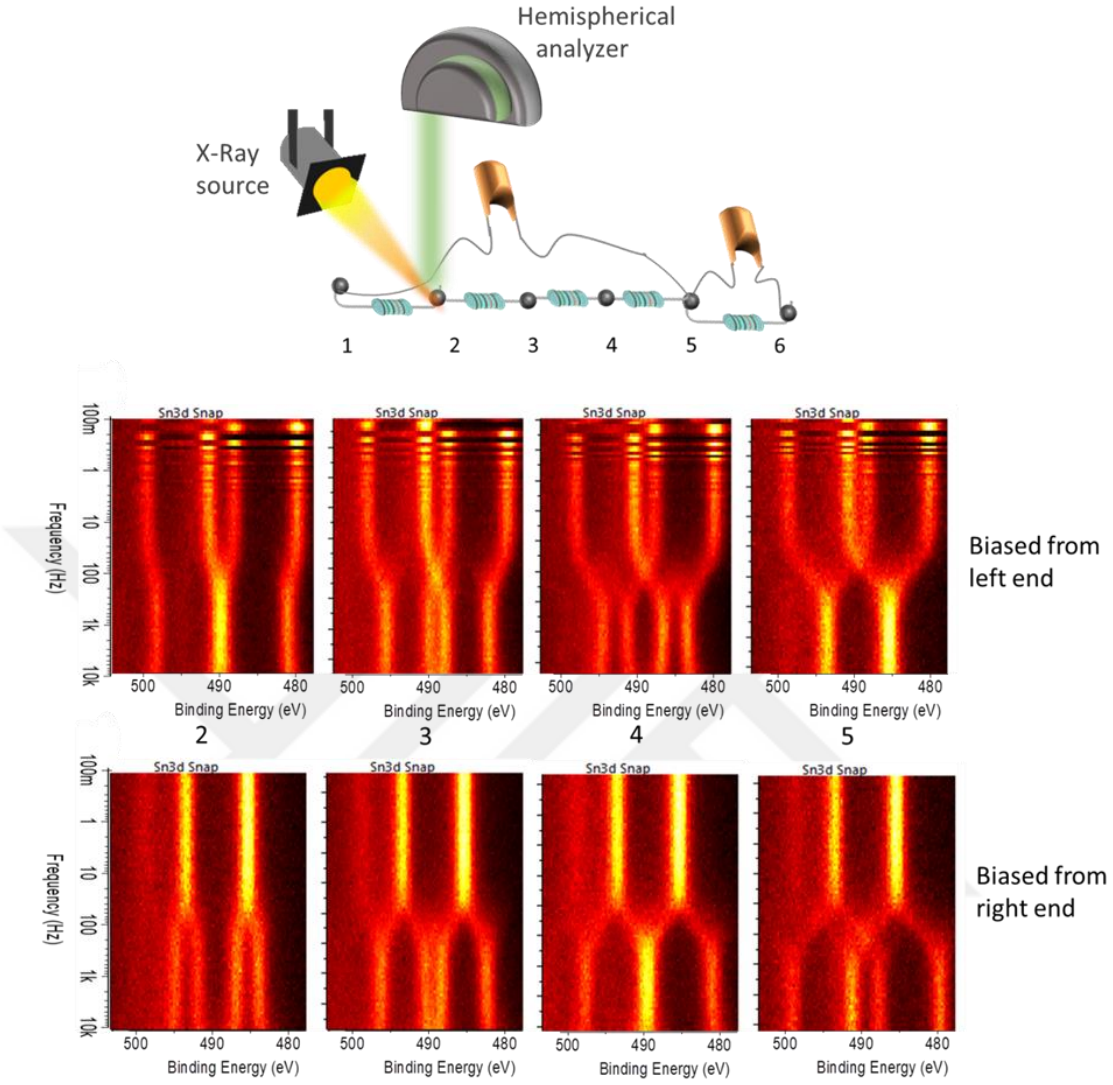

Figure 45 Sn3d spectra recorded at four different positions on the mimicking device. Top row correspond to actuation from the wire electrode, while bottom row from the planar Si electrode.

Our findings both from the experiment and the simulation suggest that our EWOD device under investigation shows two distinct behaviors separated by a critical frequency estimated as 70 Hz which is the lowest critical frequency ever reported for the liquid polyethylene glycol with a 600 Da molecular weight. This

critical frequency is dependent on the AC resistance (impedance) (and the chemical composition) and the ionic content of the liquid, hence increases when ionic moieties are introduced. The electrical characteristics of the dielectric layer is another contributing factor. Below the critical frequency, the liquid complies faithfully to the applied bias, as determined by the constant shift in the binding energy position of the XPS peaks representative of the liquid throughout its entire surface. The liquid completely screens the applied electrical field and the entire potential drop takes place at the liquid/dielectric interface. However, for frequencies above the critical one, the resistive component of the system dominates and the drop behaves like a resistive strip, resulting in the formation of equipotential surface contours which are derived from the differences in the positions of the twinned O1s peaks under AC application and shown experimentally for the first time in this study.

Chapter 4

4. Conclusions

In this doctoral thesis, we used the well-known Voltage Contrast X-Ray Photoelectron Spectroscopy to follow both electrical and chemical properties of nonaqueous and non-volatile liquids in devices used particularly for electrowetting applications. The technique was previously applied by us to investigate electrical characterization of graphene based solid-state devices under operating conditions. Establishing this novel technique by using both DC and AC excitation has opened up a new perspective to assess the performance of other device geometries, including liquid/solid and liquid/vacuum interfaces. In the present work, we have focused on a particular and commonly used electrowetting on dielectric (EWOD) geometry and used two types of nonaqueous liquids, namely ionic liquid DEME-TFSI and Polyethylene glycol as representative of two extreme cases in terms of ionic content.

In the first part, we have focused on the fundamental understanding of the DC electrowetting phenomenon, and we have shown that with XPS we can follow the geometrical changes that droplet undergoes during an external electrical excitation. As in the air ambient, liquid droplet expanded and spread on the substrate with application of the electrical bias independent from the polarity and retracted upon its removal. We also were able to trace the electrical potential developments on and around the droplet under DC excitation, using the shifts in the binding energy positions of XPS peaks of the liquid and the substrate separately. As a result, we have established that, whereas no potential drop is observable at the wire counter electrode/liquid interface, the entire potential drop develops across the liquid/substrate interface faster than our probe time, up to large biases even leading to the dielectric breakdown. Finally, we did not observe any effect of increasing ionic content to the potential developments of the liquid through the analysis of IL and PEG separately.

Secondly, we have tried to understand the frequency dependent potential developments of EWOD devices during the AC electrowetting. Our time dependent XPS measurements under AC excitation with sweeping frequency have shown that EWOD devices exhibit two different behaviors before and after a critical frequency. Whereas below the critical frequency device behave very similar to the DC case, after the critical frequency resistive component dominates and results in the formation of electrical potential distribution on the liquid surface similar to a resistive strip model that we had previously observed in the graphene-based solid state devices.

In the last part of the thesis, we proposed an equivalent electrical circuit based on the electrical impedance spectroscopy and the calculations in order to electrically describe the EWOD devices. Then we furthered the use of this circuit to simulate the observed XPS spectral data and also to fabricate a solid-state mimicking device to reproduce the same XPS spectral observations.

Bibliography

[1] A. Fahlman; K. Hamrin; J. Hedman; R. Nordberg; C. Nordling and K. Siegbahn, "Electron Spectroscopy and Chemical Binding." *Nature,* vol. 210, pp. 4, 1966.

[2] C. N. K. Siegbahn, A. Fahlman, K. Hamrin, J. Hedman, R. Nordberg, C. Johansson, T. Bergmark, S.-E. Karlsson, I. Lindgren, B. Lindberg. "Atomic, Molecular and Solid-State Structure Studied by Means of Electron Spectroscopy". 20.1-282 Almqvist and Wiksells, 1967.

[3] K. M. Siegbahn , "Nobel Lecture", NobelPrize.org, Nobel Media AB, 2018. https://www.nobelprize.org/prizes/physics/1981/siegbahn/lecture/

[4] J. W. John and F. Watts, *An Introduction to Surface Analysis by XPS and AES,* ch.1 "Electron Spectroscopy: Some Basic Concepts", Wiley-VCH, pp. 1-15, 2003.

[5] J. W. John and F. Watts, *An Introduction to Surface Analysis by XPS and AES,* ch.2 " Electron Spectrometer Design", Wiley-VCH, pp. 17-58, 2003.

[6] J. W. John and F. Watts, *An Introduction to Surface Analysis by XPS and AES*, ch.4 "Compositional Depth Profiling", Wiley-VCH, pp. 79-111 , 2003.

[7] C. S. Fadley, *Electron Emission Spectroscopy.* (eds W. Dekeyser, L. Fiermans, G. Vanderkelen and J. Vennik), ch.2 "Theoretical Aspects of X-Ray Photoelectron Spectroscopy", pp. 151-224 ,Springer Netherlands.

[8] D. Briggs and J. T. Grant, "Surface Analysis by Auger and X-ray Photoelectron Spectroscopy", IMPublications, Chichester, 2003

[9] C. S. Fadley, "X-Ray Photoelectron Spectroscopy: Progress and Perspectives." *Journal of Electron Spectroscopy and Related Phenomena,* vol. 178-179, pp. 2-32, 2010.

[10] J. E. Castle and A. M. Salvi, "Interpretation of the Shirley Background in X-Ray Photoelectron Spectroscopy Analysis." *Journal of Vacuum Science & Technology A,* vol. 19, pp. 1170-1175, 2001.

[11] J. Hedman; P. F. Hedén; C. Nordling and K. Siegbahn, "Energy Splitting of Core Electron Levels in Paramagnetic Molecules." *Physics Letters A,* vol. 29, pp. 178-179, 1969.

[12] C. S. Fadley; S. B. M. Hagström; J. M. Hollander; M. P. Klein and D. A. Shirley, "Chemical Bonding Information from Photoelectron Spectroscopy." vol. 157, pp. 1571-1573, 1967.

[13] J. W. John and F. Watts, *An Introduction to Surface Analysis by XPS and AES,* ch.4 "Compositional Depth Profiling", Wiley-VCH, pp. 79-111 , 2003.

[14] C. Kocabas and S. Suzer, "Probing Voltage Drop Variations in Graphene with Photoelectron Spectroscopy." *Analytical Chemistry,* vol. 85, pp. 4172-4177, 2013.

[15] P. Aydogan Gokturk; N. Kakenov; C. Kocabas and S. Suzer, "Raman and X-Ray Photoelectron Spectroscopic Studies of Graphene Devices for Identification of Doping." *Applied Surface Science,* vol. 425, pp. 1130-1137, 2017.

[16] M. A. Brown; A. Beloqui Redondo; M. Sterrer; B. Winter; G. Pacchioni; Z. Abbas and J. A. van Bokhoven, "Measure of Surface Potential at the Aqueous–Oxide Nanoparticle Interface by Xps from a Liquid Microjet." *Nano Letters,* vol. 13, pp. 5403-5407, 2013.

[17] H. Sezen and S. Suzer, "Xps for Chemical- and Charge-Sensitive Analyses." *Thin Solid Films,* vol. 534, pp. 1-11, 2013.

[18] H. Sezen and S. Suzer, "Dynamical Xps Measurements for Probing Photoinduced Voltage Changes." *Surface Science,* vol. 604, pp. L59-L62, 2010.

[19] H. Sezen; G. Ertas and S. Suzer, "Methods for Probing Charging Properties of Polymeric Materials Using Xps." *Journal of Electron Spectroscopy and Related Phenomena,* vol. 178-179, pp. 373-379, 2010.

[20] E. Yilmaz; H. Sezen and S. Suzer, "Probing the Charge Build-up and Dissipation on Thin Pmma Film Surfaces at the Molecular Level by Xps." vol. 51, pp. 5488-5492, 2012.

[21] S. Suzer; E. Abelev and S. L. Bernasek, "Impedance-Type Measurements Using Xps." *Applied Surface Science,* vol. 256, pp. 1296-1298, 2009.

[22] S. Suzer; H. Sezen; G. Ertas and A. Dâna, "Xps Measurements for Probing Dynamics of Charging." *Journal of Electron Spectroscopy and Related Phenomena,* vol. 176, pp. 52-57, 2010.

[23] H. Sezen; G. Ertas; A. Dâna and S. Suzer, "Charging/Discharging of Thin Ps/Pmma Films as Probed by Dynamic X-Ray Photoelectron Spectroscopy." *Macromolecules,* vol. 40, pp. 4109-4112, 2007.

[24] P. Aydogan; E. O. Polat; C. Kocabas and S. Suzer, "X-Ray Photoelectron Spectroscopy for Identification of Morphological Defects and Disorders in Graphene Devices." vol. 34, pp. 041516, 2016.

[25] M. Copuroglu; P. Aydogan; E. O. Polat; C. Kocabas and S. Süzer, "Gate-Tunable Photoemission from Graphene Transistors." *Nano Letters,* vol. 14, pp. 2837-2842, 2014.

[26] P. Aydogan; O. Balci; C. Kocabas and S. Suzer, "Monitoring the Operation of a Graphene Transistor in an Integrated Circuit by Xps." *Organic Electronics,* vol. 37, pp. 178-182, 2016.

[27] M. T. Camci; P. Aydogan; B. Ulgut; C. Kocabas and S. Suzer, "Xps Enables Visualization of Electrode Potential Screening in an Ionic Liquid Medium with Temporal- and Lateral-Resolution." *Physical Chemistry Chemical Physics,* vol. 18, pp. 28434-28440, 2016.

[28] S. Axnanda; E. J. Crumlin; B. Mao; S. Rani; R. Chang; P. G. Karlsson; M. O. M. Edwards; M. Lundqvist; R. Moberg; P. Ross; Z. Hussain and Z. Liu, "Using “Tender” X-Ray Ambient Pressure X-Ray Photoelectron Spectroscopy as a Direct Probe of Solid-Liquid Interface." *Scientific Reports,* vol. 5, pp. 9788, 2015.

[29] M. A. Brown; Z. Abbas; A. Kleibert; R. G. Green; A. Goel; S. May and T. M. Squires, "Determination of Surface Potential and Electrical Double-Layer Structure at the Aqueous Electrolyte-Nanoparticle Interface." *Physical Review X,* vol. 6, pp. 011007, 2016.

[30] M. Favaro; B. Jeong; P. N. Ross; J. Yano; Z. Hussain; Z. Liu and E. J. Crumlin, "Unravelling the Electrochemical Double Layer by Direct Probing of the Solid/Liquid Interface." *Nature Communications,* vol. 7, pp. 12695, 2016.

[31] M. F. Lichterman; S. Hu; M. H. Richter; E. J. Crumlin; S. Axnanda; M. Favaro; W. Drisdell; Z. Hussain; T. Mayer; B. S. Brunschwig; N. S. Lewis; Z. Liu and H.-

J. Lewerenz, "Direct Observation of the Energetics at a Semiconductor/Liquid Junction by Operando X-Ray Photoelectron Spectroscopy." *Energy & Environmental Science,* vol. 8, pp. 2409-2416, 2015.

[32] H. Siegbahn and K. Siegbahn, "Esca Applied to Liquids." *Journal of Electron Spectroscopy and Related Phenomena,* vol. 2, pp. 319-325, 1973.

[33] H. Siegbahn, "Electron Spectroscopy for Chemical Analysis of Liquids and Solutions." *The Journal of Physical Chemistry,* vol. 89, pp. 897-909, 1985.

[34] T. Lena; R. H. Ashley; K. Osman; K. Line and B. Hendrik, "Ambient Pressure Photoelectron Spectroscopy: Practical Considerations and Experimental Frontiers." *Journal of Physics: Condensed Matter,* vol. 29, pp. 053002, 2017.

[35] R. Seidel; S. Thürmer and B. Winter, "Photoelectron Spectroscopy Meets Aqueous Solution: Studies from a Vacuum Liquid Microjet." *The Journal of Physical Chemistry Letters,* vol. 2, pp. 633-641, 2011.

[36] B. Winter, "Liquid Microjet for Photoelectron Spectroscopy." *Nuclear Instruments and Methods in Physics Research Section A: Accelerators, Spectrometers, Detectors and Associated Equipment,* vol. 601, pp. 139-150, 2009.

[37] M. Faubel; K. R. Siefermann; Y. Liu and B. Abel, "Ultrafast Soft X-Ray Photoelectron Spectroscopy at Liquid Water Microjets." *Accounts of Chemical Research,* vol. 45, pp. 120-130, 2012.

[38] E. F. Smith; I. J. Villar Garcia; D. Briggs and P. Licence, "Ionic Liquids in Vacuo; Solution-Phase X-Ray Photoelectron Spectroscopy." *Chemical Communications,* vol., pp. 5633-5635, 2005.

[39] F. Qiu; A. W. Taylor; S. Men; I. J. Villar-Garcia and P. Licence, "An Ultra High Vacuum-Spectroelectrochemical Study of the Dissolution of Copper in the Ionic Liquid (N-Methylacetate)-4-Picolinium

Bis(Trifluoromethylsulfonyl)Imide." *Physical Chemistry Chemical Physics,* vol. 12, pp. 1982-1990, 2010.

[40] A. W. Taylor; F. Qiu; I. J. Villar-Garcia and P. Licence, "Spectroelectrochemistry at Ultrahigh Vacuum: In Situ Monitoring of Electrochemically Generated Species by X-Ray Photoelectron Spectroscopy." *Chemical Communications,* vol., pp. 5817-5819, 2009.

[41] Z. Lei; B. Chen; Y.-M. Koo and D. R. MacFarlane, "Introduction: Ionic Liquids." *Chemical Reviews,* vol. 117, pp. 6633-6635, 2017.

[42] M. Watanabe; M. L. Thomas; S. Zhang; K. Ueno; T. Yasuda and K. Dokko, "Application of Ionic Liquids to Energy Storage and Conversion Materials and Devices." *Chemical Reviews,* vol. 117, pp. 7190-7239, 2017.

[43] S. P. M. Ventura; F. A. e Silva; M. V. Quental; D. Mondal; M. G. Freire and J. A. P. Coutinho, "Ionic-Liquid-Mediated Extraction and Separation Processes for Bioactive Compounds: Past, Present, and Future Trends." *Chemical Reviews,* vol. 117, pp. 6984-7052, 2017.

[44] S. Z. E. Abedin; M. Pölleth; S. A. Meiss; J. Janek and F. Endres, "Ionic Liquids as Green Electrolytes for the Electrodeposition of Nanomaterials." *Green Chemistry,* vol. 9, pp. 549-553, 2007.

[45] M. Hayyan; F. S. Mjalli; M. A. Hashim; I. M. AlNashef and T. X. Mei, "Investigating the Electrochemical Windows of Ionic Liquids." *Journal of Industrial and Engineering Chemistry,* vol. 19, pp. 106-112, 2013.

[46] S. Kazemiabnavi; Z. Zhang; K. Thornton and S. Banerjee, "Electrochemical Stability Window of Imidazolium-Based Ionic Liquids as Electrolytes for Lithium Batteries." *The Journal of Physical Chemistry B,* vol. 120, pp. 5691-5702, 2016.

[47] S. P. Ong; O. Andreussi; Y. Wu; N. Marzari and G. Ceder, "Electrochemical Windows of Room-Temperature Ionic Liquids from Molecular Dynamics and

Density Functional Theory Calculations." *Chemistry of Materials,* vol. 23, pp. 2979-2986, 2011.

[48] N. Jayaprakash; S. K. Das and L. A. Archer, "The Rechargeable Aluminum-Ion Battery." *Chemical Communications,* vol. 47, pp. 12610-12612, 2011.

[49] M. Angell; C.-J. Pan; Y. Rong; C. Yuan; M.-C. Lin; B.-J. Hwang and H. Dai, "High Coulombic Efficiency Aluminum-Ion Battery Using an Alcl₃-Urea Ionic Liquid Analog Electrolyte." vol. 114, pp. 834-839, 2017.

[50] M.-C. Lin; M. Gong; B. Lu; Y. Wu; D.-Y. Wang; M. Guan; M. Angell; C. Chen; J. Yang; B.-J. Hwang and H. Dai, "An Ultrafast Rechargeable Aluminium-Ion Battery." *Nature,* vol. 520, pp. 324, 2015.

[51] A. Lewandowski and A. Świderska-Mocek, "Ionic Liquids as Electrolytes for Li-Ion Batteries—an Overview of Electrochemical Studies." *Journal of Power Sources,* vol. 194, pp. 601-609, 2009.

[52] I. Osada; H. de Vries; B. Scrosati and S. J. A. C. I. e. Passerini, "Ionic-Liquid-Based Polymer Electrolytes for Battery Applications." vol. 55, pp. 500-513, 2016.

[53] A. B. McEwen; S. F. McDevitt and V. R. Koch, "Nonaqueous Electrolytes for Electrochemical Capacitors: Imidazolium Cations and Inorganic Fluorides with Organic Carbonates." vol. 144, pp. L84-L86, 1997.

[54] A. B. McEwen; H. L. Ngo; K. LeCompte and J. L. Goldman, "Electrochemical Properties of Imidazolium Salt Electrolytes for Electrochemical Capacitor Applications." vol. 146, pp. 1687-1695, 1999.

[55] C. Du; S. Liu; W. Zhang; X. Zhang and Y. Deng, "Nitrogen-Doped Carbon Nanotubes Based on Ionic Liquid Precursors as Effective Cathode Catalysts for Li/Socl2 Batteries." vol. 165, pp. A1955-A1960, 2018.

[56] C. Lv; X. Duan; J. Deng and T. Wang, "Lifepo4 Mesocrystals Coated with N-Doped Carbon from an Ionic Liquid for Li-Ion Batteries." *CrystEngComm,* vol. 19, pp. 1253-1257, 2017.

[57] Y. Yao; Y. Jiang; H. Yang; X. Sun and Y. Yu, "Na3v2(Po4)3 Coated by N-Doped Carbon from Ionic Liquid as Cathode Materials for High Rate and Long-Life Na-Ion Batteries." *Nanoscale,* vol. 9, pp. 10880-10885, 2017.

[58] J. Zhu; Y. Shen; A. Xie; L. Qiu; Q. Zhang and S. Zhang, "Photoinduced Synthesis of Anisotropic Gold Nanoparticles in Room-Temperature Ionic Liquid." *The Journal of Physical Chemistry C,* vol. 111, pp. 7629-7633, 2007.

[59] C. W. Scheeren; G. Machado; S. R. Teixeira; J. Morais; J. B. Domingos and J. Dupont, "Synthesis and Characterization of Pt(0) Nanoparticles in Imidazolium Ionic Liquids." *The Journal of Physical Chemistry B,* vol. 110, pp. 13011-13020, 2006.

[60] P. B. Murphy; F. Liu; S. C. Cook; N. Jahan; D. G. Marangoni; T. B. Grindley and P. Zhang, "Structural Control of Au and Au–Pd Nanoparticles by Selecting Capping Ligands with Varied Electronic and Steric Effects." *Canadian Journal of Chemistry,* vol. 87, pp. 1641-1649, 2009.

[61] P. Migowski; G. Machado; S. R. Texeira; M. C. M. Alves; J. Morais; A. Traverse and J. Dupont, "Synthesis and Characterization of Nickel Nanoparticles Dispersed in Imidazolium Ionic Liquids." *Physical Chemistry Chemical Physics,* vol. 9, pp. 4814-4821, 2007.

[62] M. T. Camci; B. Ulgut; C. Kocabas and S. Suzer, "In-Situ Xps Monitoring and Characterization of Electrochemically Prepared Au Nanoparticles in an Ionic Liquid." *ACS Omega,* vol. 2, pp. 478-486, 2017.

[63] J. Krämer; E. Redel; R. Thomann and C. Janiak, "Use of Ionic Liquids for the Synthesis of Iron, Ruthenium, and Osmium Nanoparticles from Their Metal Carbonyl Precursors." *Organometallics,* vol. 27, pp. 1976-1978, 2008.

[64] M.-A. Neouze, "About the Interactions between Nanoparticles and Imidazolium Moieties: Emergence of Original Hybrid Materials." *Journal of Materials Chemistry,* vol. 20, pp. 9593-9607, 2010.

[65] R. D. Rogers and K. R. Seddon, "Ionic Liquids--Solvents of the Future?." vol. 302, pp. 792-793, 2003.

[66] E. F. Smith; F. J. M. Rutten; I. J. Villar-Garcia; D. Briggs and P. Licence, "Ionic Liquids in Vacuo: Analysis of Liquid Surfaces Using Ultra-High-Vacuum Techniques." *Langmuir,* vol. 22, pp. 9386-9392, 2006.

[67] S. Caporali; U. Bardi and A. Lavacchi, "X-Ray Photoelectron Spectroscopy and Low Energy Ion Scattering Studies on 1-Buthyl-3-Methyl-Imidazolium Bis(Trifluoromethane) Sulfonimide." *Journal of Electron Spectroscopy and Related Phenomena,* vol. 151, pp. 4-8, 2006.

[68] S. Men; K. R. J. Lovelock and P. Licence, "X-Ray Photoelectron Spectroscopy of Pyrrolidinium-Based Ionic Liquids: Cation–Anion Interactions and a Comparison to Imidazolium-Based Analogues." *Physical Chemistry Chemical Physics,* vol. 13, pp. 15244-15255, 2011.

[69] S. Men; B. B. Hurisso; K. R. J. Lovelock and P. Licence, "Does the Influence of Substituents Impact Upon the Surface Composition of Pyrrolidinium-Based Ionic Liquids? An Angle Resolved Xps Study." *Physical Chemistry Chemical Physics,* vol. 14, pp. 5229-5238, 2012.

[70] S. Men; D. S. Mitchell; K. R. J. Lovelock and P. Licence, "X-Ray Photoelectron Spectroscopy of Pyridinium-Based Ionic Liquids: Comparison to Imidazolium- and Pyrrolidinium-Based Analogues." vol. 16, pp. 2211-2218, 2015.

[71] R. K. Blundell and P. Licence, "Quaternary Ammonium and Phosphonium Based Ionic Liquids: A Comparison of Common Anions." *Physical Chemistry Chemical Physics,* vol. 16, pp. 15278-15288, 2014.

[72] I. J. Villar-Garcia; E. F. Smith; A. W. Taylor; F. Qiu; K. R. J. Lovelock; R. G. Jones and P. Licence, "Charging of Ionic Liquid Surfaces under X-Ray Irradiation: The Measurement of Absolute Binding Energies by Xps." *Physical Chemistry Chemical Physics,* vol. 13, pp. 2797-2808, 2011.

[73] S. Men and P. Licence, "Tuning the Electronic Environment of the Anion by Using Binary Ionic Liquid Mixtures." *Chemical Physics Letters,* vol. 681, pp. 40-43, 2017.

[74] S. Men and P. Licence, "Probing the Electronic Environment of Binary and Ternary Ionic Liquid Mixtures by X-Ray Photoelectron Spectroscopy." *Chemical Physics Letters,* vol. 686, pp. 74-77, 2017.

[75] V. Lockett; R. Sedev; S. Harmer; J. Ralston; M. Horne and T. Rodopoulos, "Orientation and Mutual Location of Ions at the Surface of Ionic Liquids." *Physical Chemistry Chemical Physics,* vol. 12, pp. 13816-13827, 2010.

[76] V. Lockett; R. Sedev; C. Bassell and J. Ralston, "Angle-Resolved X-Ray Photoelectron Spectroscopy of the Surface of Imidazolium Ionic Liquids." *Physical Chemistry Chemical Physics,* vol. 10, pp. 1330-1335, 2008.

[77] F. Maier; J. M. Gottfried; J. Rossa; D. Gerhard; P. S. Schulz; W. Schwieger; P. Wasserscheid and H.-P. Steinrück, "Surface Enrichment and Depletion Effects of Ions Dissolved in an Ionic Liquid: An X-Ray Photoelectron Spectroscopy Study." vol. 45, pp. 7778-7780, 2006.

[78] K. R. J. Lovelock; I. J. Villar-Garcia; F. Maier; H.-P. Steinrück and P. Licence, "Photoelectron Spectroscopy of Ionic Liquid-Based Interfaces." *Chemical Reviews,* vol. 110, pp. 5158-5190, 2010.

[79] D. Weingarth; A. Foelske-Schmitz; A. Wokaun and R. Kötz, "In Situ Electrochemical Xps Study of the Pt/[Emim][Bf4] System." *Electrochemistry Communications,* vol. 13, pp. 619-622, 2011.

[80] K. R. J. Lovelock; E. F. Smith; A. Deyko; I. J. Villar-Garcia; P. Licence and R. G. Jones, "Water Adsorption on a Liquid Surface." *Chemical Communications,* vol., pp. 4866-4868, 2007.

[81] R. Wibowo; L. Aldous; R. M. J. Jacobs; N. S. A. Manan and R. G. Compton, "In Situ Electrochemical-X-Ray Photoelectron Spectroscopy: Rubidium Metal Deposition from an Ionic Liquid in Competition with Solvent Breakdown." *Chemical Physics Letters,* vol. 517, pp. 103-107, 2011.

[82] P. Aydogan Gokturk; S. E. Donmez; B. Ulgut; Y. E. Türkmen and S. Suzer, "Optical and Xps Evidence for the Electrochemical Generation of an N-Heterocyclic Carbene and Its Cs2 Adduct from the Ionic Liquid [Bmim][Pf6]." *New Journal of Chemistry,* vol. 41, pp. 10299-10304, 2017.

[83] P. Aydogan Gokturk; U. Salzner; L. Nyulászi; B. Ulgut; C. Kocabas and S. Suzer, "Xps-Evidence for in-Situ Electrochemically-Generated Carbene Formation." *Electrochimica Acta,* vol. 234, pp. 37-42, 2017.

[84] H.-M. Shin; T. E. McKone and D. H. Bennett, "Contribution of Low Vapor Pressure-Volatile Organic Compounds (Lvp-Vocs) from Consumer Products to Ozone Formation in Urban Atmospheres." *Atmospheric Environment,* vol. 108, pp. 98-106, 2015.

[85] C. Fruijtier-Pölloth, "Safety Assessment on Polyethylene Glycols (Pegs) and Their Derivatives as Used in Cosmetic Products." *Toxicology,* vol. 214, pp. 1-38, 2005.

[86] H.-J. Jang; C. Y. Shin and K.-B. Kim, "Safety Evaluation of Polyethylene Glycol (Peg) Compounds for Cosmetic Use." *Toxicological research,* vol. 31, pp. 105-136, 2015.

[87] J. Chen; S. K. Spear; J. G. Huddleston and R. D. Rogers, "Polyethylene Glycol and Solutions of Polyethylene Glycol as Green Reaction Media." *Green Chemistry,* vol. 7, pp. 64-82, 2005.

[88] P. G. de Gennes, "Wetting: Statics and Dynamics." *Reviews of Modern Physics,* vol. 57, pp. 827-863, 1985.

[89] Y. Yuan and T. R. Lee. in *Surface Science Techniques* (eds Gianangelo Bracco & Bodil Holst) pp. 3-34,Springer Berlin Heidelberg, 2013.

[90] S. Lee; J.-S. Park and T. R. Lee, "The Wettability of Fluoropolymer Surfaces: Influence of Surface Dipoles." *Langmuir,* vol. 24, pp. 4817-4826, 2008.

[91] R. Seemann; M. Brinkmann; E. J. Kramer; F. F. Lange and R. Lipowsky, "Wetting Morphologies at Microstructured Surfaces." vol. 102, pp. 1848-1852, 2005.

[92] X. Yong and L. T. Zhang, "Nanoscale Wetting on Groove-Patterned Surfaces." *Langmuir,* vol. 25, pp. 5045-5053, 2009.

[93] M. Frieder and B. Jean-Christophe, "Electrowetting: From Basics to Applications." *Journal of Physics: Condensed Matter,* vol. 17, pp. R705, 2005.

[94] T. B. Jones, "On the Relationship of Dielectrophoresis and Electrowetting." *Langmuir,* vol. 18, pp. 4437-4443, 2002.

[95] H. Moon; S. K. Cho; R. L. Garrell and C.-J. C. Kim, "Low Voltage Electrowetting-on-Dielectric." vol. 92, pp. 4080-4087, 2002.

[96] W. C. Nelson and C.-J. C. Kim, "Droplet Actuation by Electrowetting-on-Dielectric (Ewod): A Review." *Journal of Adhesion Science and Technology,* vol. 26, pp. 1747-1771, 2012.

[97] V. Narasimhan and S.-Y. Park, "An Ion Gel as a Low-Cost, Spin-Coatable, High-Capacitance Dielectric for Electrowetting-on-Dielectric (Ewod)." *Langmuir,* vol. 31, pp. 8512-8518, 2015.

[98] S. Berry; J. Kedzierski and B. Abedian, "Low Voltage Electrowetting Using Thin Fluoroploymer Films." *Journal of Colloid and Interface Science,* vol. 303, pp. 517-524, 2006.

[99] A. Quinn; R. Sedev and J. Ralston, "Contact Angle Saturation in Electrowetting." *The Journal of Physical Chemistry B,* vol. 109, pp. 6268-6275, 2005.

[100] S. Chevalliot; S. Kuiper and J. Heikenfeld, "Experimental Validation of the Invariance of Electrowetting Contact Angle Saturation." *Journal of Adhesion Science and Technology,* vol. 26, pp. 1909-1930, 2012.

[101] D. Klarman; D. Andelman and M. Urbakh, "A Model of Electrowetting, Reversed Electrowetting, and Contact Angle Saturation." *Langmuir,* vol. 27, pp. 6031-6041, 2011.

[102] H. J. J. Verheijen and M. W. J. Prins, "Reversible Electrowetting and Trapping of Charge: Model and Experiments." *Langmuir,* vol. 15, pp. 6616-6620, 1999.

[103] A. G. Banpurkar; Y. Sawane; S. M. Wadhai; C. U. Murade; I. Siretanu; D. van den Ende and F. Mugele, "Spontaneous Electrification of Fluoropolymer–Water Interfaces Probed by Electrowetting." *Faraday Discussions,* vol. 199, pp. 29-47, 2017.

[104] M. Vallet; M. Vallade and B. Berge, "Limiting Phenomena for the Spreading of Water on Polymer Films by Electrowetting." *Eur. Phys. J. B,* vol. 11, pp. 583-591, 1999.

[105] Y. B. Sawane; S. B. Ogale and A. G. Banpurkar, "Low Voltage Electrowetting on Ferroelectric Pvdf-Hfp Insulator with Highly Tunable Contact Angle Range." *ACS Applied Materials & Interfaces,* vol. 8, pp. 24049-24056, 2016.

[106] H.-H. Shen; L.-Y. Chung and D.-J. Yao, "Improving the Dielectric Properties of an Electrowetting-on-Dielectric Microfluidic Device with a Low-Pressure

Chemical Vapor Deposited Si3n4 Dielectric Layer." *Biomicrofluidics,* vol. 9, pp. 022403, 2015.

[107] W. J. J. Welters and L. G. J. Fokkink, "Fast Electrically Switchable Capillary Effects." *Langmuir,* vol. 14, pp. 1535-1538, 1998.

[108] B. Bhushan and Y. Pan, "Role of Electric Field on Surface Wetting of Polystyrene Surface." *Langmuir,* vol. 27, pp. 9425-9429, 2011.

[109] Y.-Y. Lin; R. D. Evans; E. Welch; B.-N. Hsu; A. C. Madison and R. B. Fair, "Low Voltage Electrowetting-on-Dielectric Platform Using Multi-Layer Insulators." *Sensors and actuators. B, Chemical,* vol. 150, pp. 465-470, 2010.

[110] Y.-J. Li and B. P. Cahill, "Frequency Dependence of Low-Voltage Electrowetting Investigated by Impedance Spectroscopy." *Langmuir,* vol. 33, pp. 13139-13147, 2017.

[111] H. Shirinkami; J. Kim; C. Lee; H. C. Kim and H. Chun, "Improvement of Droplet Speed and Stability in Electrowetting on Dielectric Devices by Surface Polishing." *BioChip Journal,* vol. 11, pp. 316-321, 2017.

[112] C. Hao; Y. Liu; X. Chen; Y. He; Q. Li; K. Y. Li and Z. Wang, "Electrowetting on Liquid-Infused Film (Ewolf): Complete Reversibility and Controlled Droplet Oscillation Suppression for Fast Optical Imaging." *Scientific Reports,* vol. 4, pp. 6846, 2014.

[113] F. Mugele and S. Herminghaus, "Electrostatic Stabilization of Fluid Microstructures." *Applied Physics Letters,* vol. 81, pp. 2303-2305, 2002.

[114] J. S. Hong; S. H. Ko; K. H. Kang and I. S. Kang, "A Numerical Investigation on Ac Electrowetting of a Droplet." *Microfluidics and Nanofluidics,* vol. 5, pp. 263-271, 2008.

[115] T. B. Jones; J. D. Fowler; Y. S. Chang and C.-J. Kim, "Frequency-Based Relationship of Electrowetting and Dielectrophoretic Liquid Microactuation." *Langmuir,* vol. 19, pp. 7646-7651, 2003.

[116] T. B. Jones; K. L. Wang and D. J. Yao, "Frequency-Dependent Electromechanics of Aqueous Liquids: Electrowetting and Dielectrophoresis." *Langmuir,* vol. 20, pp. 2813-2818, 2004.

[117] X. Hu; M. Mibus; C. R. Knospe; G. Zangari and M. L. Reed, "Impedance Spectroscopy and Electrical Modeling of Electrowetting on Dielectric Devices." *Journal of Micromechanics and Microengineering,* vol. 25, pp. 045020, 2015.

[118] D. Chatterjee; H. Shepherd and R. L. Garrell, "Electromechanical Model for Actuating Liquids in a Two-Plate Droplet Microfluidic Device." *Lab on a Chip,* vol. 9, pp. 1219-1229, 2009.

[119] S. H. Ko; H. Lee and K. H. Kang, "Hydrodynamic Flows in Electrowetting." *Langmuir,* vol. 24, pp. 1094-1101, 2008.

[120] H. Lee; S. Yun; S. H. Ko and K. H. Kang, "An Electrohydrodynamic Flow in Ac Electrowetting." *Biomicrofluidics,* vol. 3, pp. 44113-44113, 2009.

[121] J. Heikenfeld; K. Zhou; E. Kreit; B. Raj; S. Yang; B. Sun; A. Milarcik; L. Clapp and R. Schwartz, "Electrofluidic Displays Using Young–Laplace Transposition of Brilliant Pigment Dispersions." *Nature Photonics,* vol. 3, pp. 292, 2009.

[122] Z. Yi; L. Shui; L. Wang; M. Jin; R. A. Hayes and G. Zhou, "A Novel Driver for Active Matrix Electrowetting Displays." *Displays,* vol. 37, pp. 86-93, 2015.

[123] W. Y. Cheng; K. L. Lo; Y. P. Chang; C. W. Wang; P. J. Su; H. H. Lee; D. W. Lee; K. C. Lee; C. C. Hsiao; J. W. Shiu; S. Y. Fuh; Y. C. Liao; J. C. Yang and C. H. Hsieh, "37.1: Novel Development of Large-Sized Electrowetting Display." vol. 39, pp. 526-529, 2008.

[124] P. Sureshkumar and S. S. Bhattacharyya, "Display Applications of Electrowetting." *Journal of Adhesion Science and Technology,* vol. 26, pp. 1947-1963, 2012.

[125] G. Beni and S. Hackwood, "Electro-Wetting Displays." *Applied Physics Letters,* vol. 38, pp. 207-209, 1981.

[126] R. A. Hayes and B. J. Feenstra, "Video-Speed Electronic Paper Based on Electrowetting." *Nature,* vol. 425, pp. 383, 2003.

[127] C. Sung Kwon; M. Hyejin and K. Chang-Jin, "Creating, Transporting, Cutting, and Merging Liquid Droplets by Electrowetting-Based Actuation for Digital Microfluidic Circuits." *Journal of Microelectromechanical Systems,* vol. 12, pp. 70-80, 2003.

[128] P. Paik; V. K. Pamula and R. B. Fair, "Rapid Droplet Mixers for Digital Microfluidic Systems." *Lab on a Chip,* vol. 3, pp. 253-259, 2003.

[129] B. Berge and J. Peseux, "Variable Focal Lens Controlled by an External Voltage: An Application of Electrowetting." *The European Physical Journal E,* vol. 3, pp. 159-163, 2000.

[130] C.-P. Chiu; T.-J. Chiang; J.-K. Chen; F.-C. Chang; F.-H. Ko; C.-W. Chu; S.-W. Kuo and S.-K. Fan, "Liquid Lenses and Driving Mechanisms: A Review." *Journal of Adhesion Science and Technology,* vol. 26, pp. 1773-1788, 2012.

[131] H. Li; M. Paneru; R. Sedev and J. Ralston, "Dynamic Electrowetting and Dewetting of Ionic Liquids at a Hydrophobic Solid–Liquid Interface." *Langmuir,* vol. 29, pp. 2631-2639, 2013.

[132] S. Millefiorini; A. H. Tkaczyk; R. Sedev; J. Efthimiadis and J. Ralston, "Electrowetting of Ionic Liquids." *Journal of the American Chemical Society,* vol. 128, pp. 3098-3101, 2006.

[133] J. Restolho; J. L. Mata and B. Saramago, "Electrowetting of Ionic Liquids: Contact Angle Saturation and Irreversibility." *The Journal of Physical Chemistry C,* vol. 113, pp. 9321-9327, 2009.

[134] M. Paneru; C. Priest; R. Sedev and J. Ralston, "Static and Dynamic Electrowetting of an Ionic Liquid in a Solid/Liquid/Liquid System." *Journal of the American Chemical Society,* vol. 132, pp. 8301-8308, 2010.

[135] Y. S. Nanayakkara; S. Perera; S. Bindiganavale; E. Wanigasekara; H. Moon and D. W. Armstrong, "The Effect of Ac Frequency on the Electrowetting Behavior of Ionic Liquids." *Analytical Chemistry,* vol. 82, pp. 3146-3154, 2010.

[136] P. Sen and C.-J. C. Kim, "Capillary Spreading Dynamics of Electrowetted Sessile Droplets in Air." *Langmuir,* vol. 25, pp. 4302-4305, 2009.

[137] Q. Vo; H. Su and T. Tran, "Universal Transient Dynamics of Electrowetting Droplets." *Scientific Reports,* vol. 8, pp. 836, 2018.

[138] L. Chen and E. Bonaccurso, "Electrowetting — from Statics to Dynamics." *Advances in Colloid and Interface Science,* vol. 210, pp. 2-12, 2014.

[139] P. Aydogan Gokturk; B. Ulgut and S. Suzer, "Dc Electrowetting of Nonaqueous Liquid Revisited by Xps." *Langmuir,* vol. 34, pp. 7301-7308, 2018.

[140] L. Y. Yeo and H.-C. Chang, "Static and Spontaneous Electrowetting." *Modern Physics Letters B,* vol. 19, pp. 549-569, 2005.

[141] J. Hwal Shin; G. Hwee Kim; I. Kim; H. Jeon; T. An and G. Lim, "Ionic Liquid Flow Along the Carbon Nanotube with Dc Electric Field." *Scientific Reports,* vol. 5, pp. 11799, 2015.

[142] U. Thiele; J. H. Snoeijer; S. Trinschek and K. John, "Equilibrium Contact Angle and Adsorption Layer Properties with Surfactants." *Langmuir,* vol. 34, pp. 7210-7221, 2018.

[143] J. Hong; Y. K. Kim; K. H. Kang; J. M. Oh and I. S. Kang, "Effects of Drop Size and Viscosity on Spreading Dynamics in Dc Electrowetting." *Langmuir,* vol. 29, pp. 9118-9125, 2013.

[144] H. Liu; S. Dharmatilleke; D. K. Maurya and A. A. O. Tay, "Dielectric Materials for Electrowetting-on-Dielectric Actuation." *Microsystem Technologies,* vol. 16, pp. 449, 2009.